

Unravelling annealing-related processes in ZnO:Al thin films used for tailoring electrical and optical properties

vorgelegt von
Master of Science

Steffi Hlawenka, geb. Schönau
geboren in Berlin

von der Fakultät II - Mathematik und Naturwissenschaften
der Technischen Universität Berlin
zur Erlangung des akademischen Grades

Doktor der Naturwissenschaften
- Dr. rer. nat. -

genehmigte Dissertation

Promotionsausschuss:

Vorsitzende: Prof. Dr. Birgit Kanngießer
Gutachter: Prof. Dr. Mario Dähne
Gutachter: Prof. Dr. Bernd Rech
Gutachter: Prof. Dr. Matthias Wuttig

Tag der wissenschaftlichen Aussprache: 16. November 2015

Berlin 2016

Contents

1	Introduction	1
2	Physical and experimental fundamentals	3
2.1	The material zinc oxide	3
2.1.1	Crystallographic structure and lattice dynamics	3
2.1.2	Doping	4
2.1.3	Electronic transport	5
2.1.4	Scattering mechanisms	7
2.1.5	Optical properties	14
2.2	Experimental methods	21
2.2.1	Sample preparation	21
2.2.1.1	Deposition of ZnO:Al	21
2.2.1.2	Deposition and removal of protective capping layers	23
2.2.1.3	Thermal post-deposition treatments	24
2.2.2	Characterisation methods	25
2.2.2.1	Optical characterisation	25
2.2.2.2	Electrical transport measurements	26
2.2.2.3	Raman spectroscopy	28
2.2.2.4	X-ray diffraction	30
3	Physical properties of ZnO:Al thin films after application of thermal post-deposition treatments with and without protective capping layer	33
3.1	Influence of the substrate temperature during deposition	34
3.1.1	Electrial, optical and structural properties in the as deposited state	34
3.1.2	Influence of thermal treatments on the structure	43
3.1.3	Change of electronic transport and sub-band gap absorption after thermal treatments	47
3.1.4	Discussion regarding microscopical changes during annealing	53
3.1.5	Summary	56
3.2	Systematic variation of oxygen addition during deposition	58
3.2.1	Electrial, optical and structural properties in the as deposited state	58
3.2.2	Influence of thermal treatments on the structure	64
3.2.3	Change of sub-band gap absorption and electronic transport after thermal treatments	65
3.2.4	Discussion regarding oxygen related changes during annealing	69
3.2.5	Summary	71

3.3	Systematic variation of nitrogen addition during deposition	73
3.3.1	Structural, electrical and optical properties in the as deposited state	74
3.3.2	Changes of properties after application of thermal treatment	78
3.3.3	Discussion of nitrogen incorporation during annealing without cap in nitrogen ambient	86
3.3.4	Summary	88
3.4	Influence of hydrogen on electrical properties and sub-band gap absorption	89
3.4.1	Addition of hydrogen to the deposition process	89
3.4.2	Employing hydrogen-rich and hydrogen-poor cap materials	92
3.4.3	Summary	94
3.5	Multi-step annealing	95
3.5.1	Repeated annealing under an amorphous silicon capping layer with and without intermediate cap renewal	95
3.5.2	Alternating application of degradation and cap annealing	98
3.5.3	Summary	100
3.6	Summary of experimental results regarding electronic transport and sub-band gap absorption	102
4	Discussion	103
4.1	Impurity related mechanisms during thermal annealing and the influence of the prevailing oxygen partial pressure	103
4.2	The origin of the exponential absorption tails in ZnO:Al	109
4.3	Technological relevance	117
5	Summary and outlook	121
	Appendix	125
	A Determination of the optical absorption coefficient	127
	B Limits for the determination of Urbach energy	133
	List of Publications	137
	List of Figures	V
	List of Tables	IX
	Bibliography	XI
	Acknowledgements	XXV

1 Introduction

Optoelectronic devices based on transparent conducting thin films (TCF) are an indispensable part of today's world. These functional layers are a key component especially in flat panel displays, light emitting diodes, touchscreens and photovoltaic devices. Here, TCFs act as a window for light to or from an active material beneath and at the same time as ohmic contact for carrier transport.

Amorphous and polycrystalline transparent conducting oxides (TCO) represent nowadays the material group with the largest economical share, while organic TCFs like polymers and carbon based nanostructures as graphene or nanotubes gain in importance, especially due to their mechanical flexibility. The most important TCOs are indium oxide (In_2O_3), tin oxide (SnO_2), impurity-doped zinc oxide (ZnO) and multicomponent oxides consisting of combinations of those materials.

Due to its outstanding high transparency and conductivity, chemical stability and ease to deposit it as thin film on large areas, tin-doped In_2O_3 (ITO) has evolved as industrial standard. However, the growing demand for transparent electrodes for optoelectronic device applications threatens the availability of ITO, since the main component, indium, is a scarce and, hence, very expensive material. Therefore, the development of cheaper materials with comparable properties is of great importance. ZnO is one promising alternative, consisting of abundant and non-toxic elements, and holds sufficiently low resistivity if doped with impurities such as aluminium.

ZnO possesses a broad field of application already for several decades. The material is industrially used as pigment e.g. in toothpaste, sunscreen, and wall colour, for catalysis and as gas sensor.

However, the current research on ZnO is not limited to its use as transparent conductor, but also includes the development of p-type layers for optically active devices such as LEDs, ZnO-based quantum structures and magnetic doping. Regarding the commercial application, the development of cost-effective production processes and the optimisation of optical and electrical properties remain a key aspect. Depending on the specific application, the requirements for the manufacturing process and material properties may differ significantly. Some applications, namely front contacts for chalcopyrite based solar cells or amorphous/crystalline silicon heterojunction solar cells, or pixel electrodes on the colour filter side of LCD displays require low deposition temperatures below 200 °C. On the other hand, much higher deposition temperatures can be used e.g. for front contacts of thin film silicon or CdTe solar cells.

In the context of the application of zinc oxide as a front electrode in polycrystalline silicon thin film solar cells it was discovered that post-deposition annealing of ZnO:Al significantly

1 Introduction

influences the materials optoelectronic properties.

While considerable enhancement of conductivity can be achieved by annealing under a protective silicon layer or under vacuum, annealing without cap in air or under nitrogen flow at comparable temperatures results in strong deterioration of its electrical properties. In continuing studies also a significant reduction of parasitic absorption in vicinity of the band edge energy was observed.

The origin of the fundamental difference between both annealing treatments is still not fully understood and its investigation will be the main content of this thesis. A strong influence of the annealing atmosphere indicates an interaction of the ZnO film with volatile compounds, especially oxygen, nitrogen and hydrogen. To distinguish the influence of the individual elements, O₂, N₂ and H₂ have been intentionally incorporated into ZnO:Al and the resulting modification of optical and electrical properties before and after annealing have been analysed.

The employed deposition and annealing conditions, as well as material basics of zinc oxide and the employed characterisation techniques are explained in chapter 2 while the experimental results are presented in chapter 3. The latter is subdivided into sections addressing the influence of the individual impurities ending with a short discussion regarding their importance in the annealing process.

A recapitulatory view on the mechanisms of the annealing process including all considered impurities is given in chapter 4. Furthermore, the origin of the observed absorption tails is discussed and the technological relevance of the findings of this thesis is presented.

Chapter 5 represents a summary of this work and an outlook.

The appendix contains additional considerations concerning the determination of the absorption coefficient of ZnO:Al and regarding the employed method for quantification of the occurring absorption tails.

2 Physical and experimental fundamentals

2.1 The material zinc oxide

2.1.1 Crystallographic structure and lattice dynamics

Zinc oxide (ZnO) is a II-IV semiconductor, meaning it is a compound of group-II^b element Zn and group-VI element O. The binding between both elements emerges from an sp^3 hybridisation leading to four tetrahedrally oriented, energetically equivalent orbitals. ZnO has a band gap of 3.4 eV [1] which makes it an interesting material for transparent electronics. The sp^3 hybridisation of the orbitals determines the crystal structure of ZnO.

Depending on the relative arrangement of the atoms ZnO exists either in cubic zinc-blende structure or hexagonal wurtzite structure, where the wurtzite structure is most common. Owing to the difference in electronegativity of Zn and O the as covalent considered bondings exhibit a considerable degree of polarity causing internal electric fields. Due to that

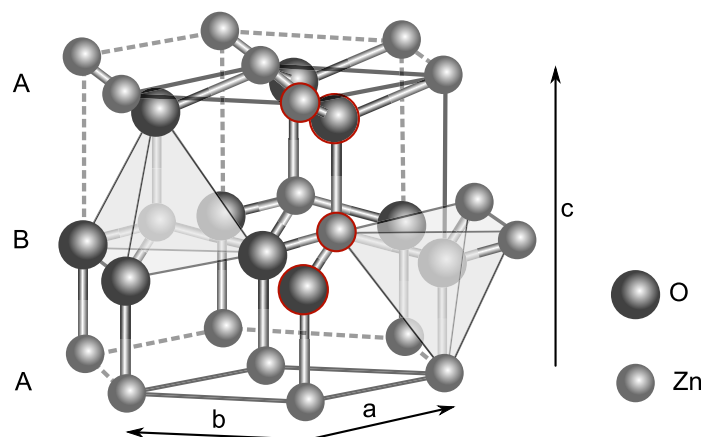


Figure 2.1: ZnO in wurtzite structure

2 Physical and experimental fundamentals

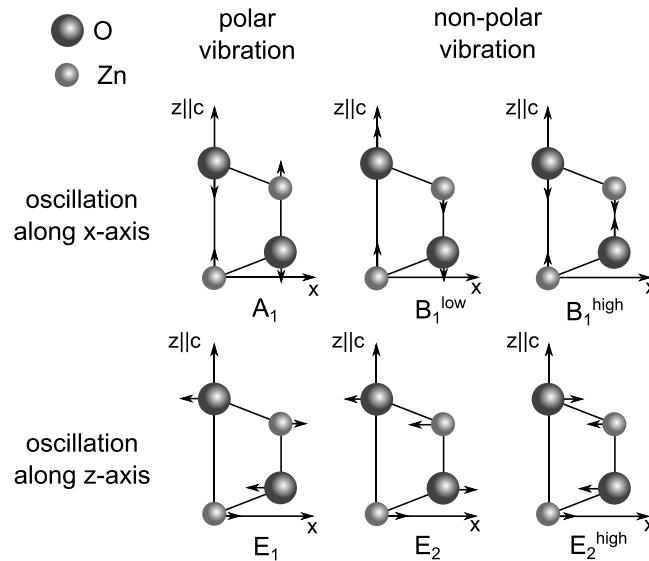


Figure 2.2: Optical phonon modes in ZnO and their atomic oscillations, according to [1]

polarity both structures are not inversion symmetric in [001] direction causing a pronounced piezoelectricity. As can be seen in figure 2.1, the hexagonal wurtzite structure is uniaxial with a pronounced axis, referred as c-axis. In plane perpendicular to the c-axis, the lattice constants a and b have equal lengths and enclose an angle of 120° . Under ambient conditions the lattice constants are $c = 0.52042$ nm and $a = b = 0.32496$ nm. The specific mass density is given with $\rho_m = 5.675$ g/cm³ [1].

For the wurtzite structure of ZnO 12 phonon branches arise, three acoustic and 9 optical [2–4]. According to space group theory, the optical phonon branches in a wurtzite lattice at the Γ -point can be described by the irreducible representation $\Gamma_{\text{opt}} = A_1 + 2B_1 + E_1 + 2E_2$ [2, 3], where the A- and B-modes are onefold and the E modes twofold degenerated. They are illustrated in figure 2.2 and their frequencies can be taken from table 2.1. A_1 and E_1 are non-polar modes, while E_2 and B_1 are polar modes causing a macroscopic electric field and an energetic splitting of longitudinal and transversal oscillations. This electric field interacts with electrons and causes a partial break of the Raman selection rules (see section 2.2.2.3), resulting, if excited close to the resonance, in an enhancement of Raman scattering intensity of those modes.

2.1.2 Doping

Even in the absence of intentional doping, ZnO shows n-type conductivity. Together with a not yet achieved reliable p-type conductivity, it indicates the relevance of electrically

Table 2.1: Optical phonon frequencies of ZnO at the Γ point of the Brillouin zone and their selection rules for Raman backscatter processes [2, 3, 5]. A short introduction into Raman spectroscopy will be given in section 2.2.2.3.

Notation	Frequency [cm^{-1}]	Raman selection rules
E_2^{low}	101	$y(xx)\bar{y}$, $z(xy)\bar{z}$, $z(xx)\bar{z}$
B_1^{low}	260	Raman silent
$A_1(\text{TO})$	380	$y(xx)\bar{y}$, $y(zz)\bar{y}$
$E_1(\text{TO})$	407	$y(zx)\bar{y}$
E_2^{high}	437	$y(xx)\bar{y}$, $z(xy)\bar{z}$, $z(xx)\bar{z}$
B_1^{high}	550	Raman silent
$A_1(\text{LO})$	574	$z(xx)\bar{z}$
$E_1(\text{LO})$	583	not in backscatter geometry

active intrinsic defects. Usually, nonstoichiometry is cited as the main cause of this native conductance but remains heavily debated [6–8]. In this context, the dominant donors are always identified as either zinc on interstitial lattice site (I_{Zn}) or oxygen vacancies (V_{O}). However, recent theoretical calculations showed both intrinsic defects are very unlikely the cause of unintentional n-type since V_{O} is assumed to be a deep rather than a shallow donor and I_{Zn} is predicted to have a higher formation energy than previously believed [9, 10]. Another proposed explanation is the unvoluntary incorporation of hydrogen acting as shallow donor [11].

Regarding industrial applications of ZnO as conducting layer, the native conductivity has to be exceeded with help of extrinsic doping. For n-type ZnO typical specimen are group-III elements like boron, aluminum, gallium and indium, substituting zinc and acting as shallow electron donors [12]. With these elements it is possible to fabricate a highly doped, degenerated zinc oxide. Due to its lower costs, especially Al as doping element is favourable and subject of numerous publications.

Considering that significant and stable p-type conductivity in ZnO could not be achieved by doping yet, indicates that the creation of p-type compensating defects (native donors) is favourable in ZnO [8, 13] and that the creation of stable acceptor atoms is very challenging [14].

2.1.3 Electronic transport

The electronic transport in semiconductors is typically described using the Drude theory [15]. This theory was actually developed for the electronic transport by an electric field in metals but can be generalised for free electrons in solids.

High (e.g. n-type) doping of zinc oxide causes the Fermi energy to shift from a position within the band gap into the conduction band. This effect is called semiconductor-metal transition. The zinc oxide becomes a degenerate semiconductor, which means that no

2 Physical and experimental fundamentals

further activation energy for donors is needed. In this state, electrons can essentially be treated as free i.e. the electrons have a parabolic dispersion relation at the bottom of the conduction band ($E(\vec{k}) \propto k^2$) and all lattice influences on the electrons are treated within the effective mass m^* approximation [16].

For relatively low carrier concentrations n , in the vicinity of the conduction band minimum (CBM), m^* is a constant and the Fermi energy is given by [17]

$$E_F(n) = \frac{\hbar^2}{2m^*} (3\pi^2 n)^{\frac{2}{3}}. \quad (2.1)$$

Generally, it is acknowledged that ZnO possesses a non-parabolic conduction band. Hence, moving away from the CBM, i.e. shifting the Fermi energy higher into the conduction band by high doping levels, deviations of the $E(\vec{k})$ shape from a parabolic form result in a \vec{k} -dependence of m^* . However, consensus about a correct description as a function of carrier concentration is still lacking. Experimentally, there are two different methods to characterise m^* . One is based on the comparison of the optically determined plasma frequency of the material with the carrier concentration [18], while the other one uses the analysis of electrical transport properties [19].

In this work, two different theoretical approaches have been considered that are based on Look *et al.* [20] and Pisarkiewicz *et al.* [21, 22]. They will be discussed in more detail later.

The carrier concentration n_{deg} required for the semiconductor-metal transition, hence, to obtain a degenerate semiconductor, is called *Mott's critical density* [23]

$$n_{\text{deg}}^{\frac{1}{3}} \cdot a_0 \approx 0.25,$$

where a_0 describes the effective Bohr radius with

$$a_0 = \frac{4\pi\epsilon_r\epsilon_0\hbar^2}{m^*e^2}.$$

Assuming $m^* = 0.28 \cdot m_e$ and $\epsilon_r = 8.75 \cdot \epsilon_0$ for an approximation of n_{deg} for ZnO [24, 25] the material becomes degenerate when the carrier concentration exceeds $n_{\text{deg}} \approx 3.5 \cdot 10^{18} \text{ cm}^{-3}$. m_e and ϵ_0 are the electron mass and the vacuum permittivity, respectively. Below this critical density the application of the electron scattering theories described below is limited.

In an external electric field $\vec{E} = E_0 \cdot \vec{e}_x$, the essentially free electrons experience an accelerating force $\vec{F}_{\text{el}} = e \cdot \vec{E}$. Within the Drude model these electrons interact with lattice atoms and get hindered in their movement by scattering events. The time between two scattering

events is called relaxation time τ and the motion of the free electrons can be described with

$$m^* \frac{d^2x}{dt^2} + \frac{m^*}{\tau} \frac{dx}{dt} = -e\vec{E}. \quad (2.2)$$

For a constant electric field, the equation can be solved in its stationary case¹ and

$$v_d = \frac{dx}{dt} = \frac{e\tau}{m^*} \cdot E = \mu E \quad (2.3)$$

applies, where v_d denotes the drift velocity of the charge carrier and μ its mobility, the proportionality factor between v_d and E .

An ensemble of electrons with a concentration of n and moving with a drift velocity v_d causes a charge current density, describable by

$$\vec{j} = en\vec{v}_d = en\mu\vec{E} = \sigma\vec{E}. \quad (2.4)$$

Equation 2.3 is also called Drude formula with σ as conductivity and represents Ohm's law. The inverse conductivity is called resistivity ρ , with

$$\rho = \frac{1}{\sigma} = \frac{1}{en\mu}. \quad (2.5)$$

2.1.4 Scattering mechanisms

The motion of electrons in a crystal, interacting with an external electric field, is impeded by scattering sites. Each different scattering process can be assigned to an individual relaxation time τ_i . The total relaxation time is then given by Matthiessen's rule

$$\tau_{\text{tot}}^{-1} = \sum \tau_i^{-1}. \quad (2.6)$$

According to equation 2.3, the total mobility is given by

$$\mu_{\text{tot}}^{-1} = \sum \mu_i^{-1}. \quad (2.7)$$

¹This case is valid if the applied forces are constant over the considered timeframe.

2 Physical and experimental fundamentals

Those scattering sites, interacting with moving electrons, can be categorised into defect and lattice scattering mechanisms. Defect scattering sites describe mainly dislocations and impurities, the latter can be either charged or neutral. Lattice scattering can be divided into scattering at optical or acoustic phonons while for acoustic phonons the interaction can take place either with the deformation potential of the lattice or with its piezoelectric potential.

In heavily doped transparent conducting oxides (TCO) it is widely agreed that ionised impurity and phonon scattering represent the most important scattering processes [19, 20, 26]. However, since sputtered zinc oxide has a polycrystalline structure, it can be expected that electron scattering at grain boundaries possesses a non-negligible share of the electron mobility limitation. A good review about electron mobility limiting processes in ZnO:Al is given by Ellmer *et al.* [27–29].

Ionised impurity scattering (IIS)

The first theoretical treatment of electron scattering by ionised impurities in semiconductors was published by Conwell and Weisskopf [30] using a reduced Coulomb potential of the scattering sites. Their approach, however, underestimates mobilities and was modified by Brooks and Herring [31] and later generalised for the application on degenerate semiconductors by Dingle [32].

In its generalised form and for a concentration of ionised impurities n_{II} with a charge Z the degenerate Brooks-Herring-Dingle (BHD) equation reads as²

$$\mu_{IIS}^{-1}(n, n_{II}) = \mu_{IIS_0}(n)^{-1} \frac{Z^2 n_{II}}{n} \quad (2.8)$$

where

$$\mu_{IIS_0}(n) = \frac{24\pi^3 \epsilon_0^2 \hbar^3}{e^3 m^{*2}} \frac{1}{F_{cc}^{BHD}} \quad (2.9)$$

with the charge carrier screening function

$$F_{cc}^{BHD} = \ln(1 + y(n)) - \frac{y(n)}{1 + y(n)} \quad (2.10)$$

$$\text{and } y(n) = \frac{3^{1/3} 4\pi^{8/3} \epsilon_0 \hbar^2 n^{1/3}}{e^2 m^*}. \quad (2.11)$$

Taking into account that ionised impurities can have either donor or acceptor character with individual charges Z_j , a distinction of both is useful. This approach was chosen by D. Look

²Here, n is again the electron concentration, while ϵ_0 denotes the vacuum permittivity, \hbar the reduced Planck constant and e the elementary charge.

to obtain a relation of ionised impurity scattering in dependence of the donor and acceptor concentration N_{Dj} and N_{Aj} , respectively [20]. The index j here means that different types of donors and acceptors can be taken into account in this model.

The electron concentration is then given by

$$n = \sum Z_{Dj} N_{Dj} - \sum Z_{Aj} N_{Aj}, \quad (2.12)$$

and equation 2.8 reads as

$$\mu_{IIS}^{-1} = \mu_{IIS_0}(n)^{-1} \frac{\sum Z_{Dj}^2 N_{Dj} + \sum Z_{Aj}^2 N_{Aj}}{n} \quad (2.13)$$

$$= \mu_{IIS_0}(n)^{-1} \frac{\sum Z_{Dj}^2 N_{Dj} + \sum Z_{Aj}^2 N_{Aj}}{\sum Z_{Dj} N_{Dj} - \sum Z_{Aj} N_{Aj}} \quad (2.14)$$

Considering aluminium in ZnO:Al as main donor with a charge $Z_D = 1$ and regarding zinc vacancies as main acceptor with $Z_A = 2$, eq. 2.14 reduces to

$$\mu_{IIS}(N_A, N_D) = \mu_{IIS_0}(n) \frac{N_D - 2N_A}{N_D + 4N_A}. \quad (2.15)$$

Effective mass according to Look and Rode

For degenerate ZnO, it has to be considered that the Fermi energy is located somewhere within the conduction band (CB), hence, due to the non-parabolicity of the CB, the effective mass m^* itself will be a function of the carrier concentration n . In his approach Look uses the approximation introduced by D. L. Rode [33]:

$$m^*(n) = \frac{m^*(n=0)}{1 - \frac{E_f(n)}{E_g} \cdot \left(1 - \frac{m^*(n=0)}{m_e}\right)^2} \quad (2.16)$$

where E_g is the 'effective mass' energy gap given by Rode as 3.42 eV for ZnO [33]. For the Fermi energy the following expression is used

$$E_F^L(n) = E_F(n) \cdot \left(1 - \frac{E_F(n)}{E_g} \left(1 - \frac{m^*(n=0)}{m_e}\right)^2\right), \quad (2.17)$$

2 Physical and experimental fundamentals

where $E_F(n)$ is the Fermi energy of a parabolic conduction band (eq. 2.1) and m_e the electron mass.

Effective mass according to Pisarkiewicz

A different addition of BHD theory regarding a non-parabolic shape of the conduction band was made by Pisarkiewicz [21, 22]. He employs a dispersion relation, in the form of

$$\frac{\hbar^2 k^2}{2m_0^*} = E + CE^2, \quad (2.18)$$

with C as non-parabolicity parameter and m_0^* as effective mass of a *parabolic* conduction band, yielding for the effective mass in a *non-parabolic* conduction band

$$m^* = \hbar^2 k \left(\frac{\partial E}{\partial k} \right) \quad (2.19)$$

$$= m_0^* (1 + 2CE). \quad (2.20)$$

These considerations lead to a correction of the charge carrier screening function according to

$$F_{cc}^P = \left[1 + \frac{4\zeta_P}{y(n)} \left(1 - \frac{\zeta_P}{8} \right) \right] \ln(1 + y(n)) - \frac{y(n)}{1 + y(n)} - 2\zeta_P \left(1 - \frac{5\zeta_P}{16} \right), \quad (2.21)$$

with

$$\zeta_P = 1 - \frac{m_0^*}{m^*}, \quad (2.22)$$

and $y(n)$ according to eq. 2.11. A parabolic conduction band would apply to $C = 0$ and $m^* = m_0^*$. For that eq. 2.21 would devolve into eq. 2.11.

For the Fermi energy in a non-parabolic conduction band he used the expression

$$E_F^P(n) = \frac{1}{2C} \left(\left\{ 1 + \frac{2C\hbar^2}{m_0^*} (3\pi^2 n)^{\frac{2}{3}} \right\}^{\frac{1}{2}} - 1 \right). \quad (2.23)$$

Phonon scattering (PS)

Considering ZnO at finite temperature, interactions between electrons and lattice vibrations (phonons) have to be taken into account considering the limitation of electron mobility. As

already mentioned, the scattering of electrons can take place either at optical or at acoustic phonons.

Polar optical phonons

Since ZnO forms a polar crystal with almost ionic bonding, electric field are induced by lattice vibrations (polar longitudinal-optical phonons) that interact with electrons. This process is also called Fröhlich-interaction.

According to the Howard-Sondheimer theory [34] the polar optical phonon mobility μ_{po} can be calculated by

$$\mu_{po}(T) = \frac{2^{9/2} \pi^{1/2} \hbar^2 (kT)^{1/2} (\exp(T_{po}/T) - 1) F_{ZnO}(n, T)}{3e (kT_{po}(m^*)^{3/2}) (\epsilon_1^{-1} - \epsilon_0^{-1})}, \quad (2.24)$$

where T_{po} is the polar optical temperature (837 K for ZnO), ϵ_1 the high frequency dielectric constant and $F_{ZnO}(n, T) = 0.93 \exp(T/T_{po})$ a 'fitting function' introduced by Look [35].

Acoustic phonons, deformation potential

Here, the scattering takes place at lattice deformations that entail a local shift of the band edges and lead to a mobility of [17, 20, 33]

$$\mu_{ac}(n, T) = \frac{\pi \hbar^4 c_1}{2^{1/2} (m^*)^{5/2} E_1^2 e k T} E_F(n)^{-1/2}, \quad (2.25)$$

where E_1 denotes the acoustic deformation potential, c_1 the longitudinal elastic constant and $E_F(n)$ the Fermi energy.

Acoustic phonons, piezoelectric potential

ZnO does not possess inversion symmetry and is consequently a piezoelectric material. It causes an electric field associated with acoustical phonons and can be calculated according to [17, 20, 33]

$$\mu_{pe}(n, T) = \frac{2^{3/2} \pi \hbar^2 \epsilon_0 \epsilon_r}{(m^*)^{3/2} P_{pe}^2 e k T} E_F(n)^{1/2}, \quad (2.26)$$

with P_{pe} as a unitless piezoelectric constant.

2 Physical and experimental fundamentals

All three individual phonon scattering processes are again combined using Matthissen's rule

$$\mu_{\text{PS}}(n, T)^{-1} = \mu_{\text{po}}(T)^{-1} + \mu_{\text{ac}}(n, T)^{-1} + \mu_{\text{pe}}(n, T)^{-1}. \quad (2.27)$$

Grain boundary scattering

ZnO thin films usually possess a polycrystalline structure and are, therefore, permeated by grain boundaries. These are crystallographically disturbed regions causing electronic states within the band gap. These states can be occupied by carriers from the grains. Depending on the kind of carrier and type of defect the charge balance causes either a depletion or accumulation zone around the grain boundary. In n-type ZnO, electrons drift into those traps leading to a barrier of height ϕ_{GB} and an area depleted of electrons around it.

A commonly used model to describe the electronic transport through grain boundaries was developed by Seto in 1975 [36] for polycrystalline silicon. He uses one dimensional grains with size L separated by very narrow area (grain boundaries, GB) with a trap state density N_{t} . The model assumes all donors, with a concentration N_{D} , to be ionised. The trapped charge carriers build up a potential barrier ϕ_{GB} , accompanied with a depletion region in grains of width $w = N_{\text{t}}/N_{\text{D}}$. Considering a low doping level ($N_{\text{D}} \cdot L < N_{\text{t}}$) the entire grains are depleted. Increasing the doping concentration increases the barrier height as well which reaches its maximum at $N_{\text{D}} = N_{\text{t}}/L$. Then, all trap states are occupied and the depletion width w and barrier height ϕ_{GB} decrease with further increase of the donor concentration:

$$\begin{aligned} \phi_{\text{GB}} &= \frac{e^2}{8\epsilon_0\epsilon_r} N_{\text{D}} L^2 & \text{for } N_{\text{D}} < N_{\text{t}}/L \\ &= \frac{e^2}{8\epsilon_0\epsilon_r} \frac{N_{\text{t}}^2}{N_{\text{D}}} & \text{for } N_{\text{D}} > N_{\text{t}}/L. \end{aligned} \quad (2.28)$$

The original model takes just thermionic emission as transport mechanism into account. However, for very high carrier concentrations ($n > 10^{20} \text{ cm}^{-3}$) those grain boundary barriers become very narrow and additional tunnelling through them takes place. The mobility of electrons resulting from only thermionic emission across the GB is given by

$$\mu_{\text{GB}}^{\text{Seto}} = \mu_0 \cdot \exp\left(-\frac{\phi_{\text{GB}}}{kT}\right) \text{ with } \mu_0 = \frac{eL}{\sqrt{2\pi m^* kT}}. \quad (2.29)$$

Considering only ionised impurity and phonon scattering and neglecting grain boundary scattering, the equations 2.14 and 2.24-2.26 provide the possibility to calculate the donor and acceptor concentration N_{D} and N_{A} , respectively, from carrier concentration n and mobility and vice versa. As will be shown, this model can lead to a conclusive explanation of

most annealing related effects on electrical transport in highly doped ZnO. This especially is consistent with the fact that grain boundaries are effectively screened at high carrier concentrations. Within this thesis, no conclusion on the importance of grain boundary scattering for lower doping levels will be made. For more detailed answers a more elaborate theory for grain boundary scattering as well as an investigation of the temperature dependence of electron mobility would be required.

Mobility model by D. Look

Look *et al.* developed a theoretical formalism with which the concentration of donors and acceptors can be calculated simply by fitting the experimentally obtained carrier concentration and mobility [20]. Since it was derived for highly doped, degenerated semiconductors, it takes only IIS and PS into account. The maximum obtainable mobility, therefore, determined in accordance to Martiensen's rule, is given by

$$\frac{1}{\mu_{\max}} = \frac{1}{\mu_{\text{IIS}}} + \frac{1}{\mu_{\text{PS}}}, \quad (2.30)$$

with μ_{IIS} and μ_{PS} according to eq. 2.15 and eq. 2.27, respectively. Any discription involving further contributions to the electrical transport would either yield a high degree of unknown parameters or requires additional information like transport properties at low temperatures.

The choice of appropriate assumptions for the effective mass m^* is important for the description of IIS. Since there is no standard description of m^* in ZnO, in this work the approaches

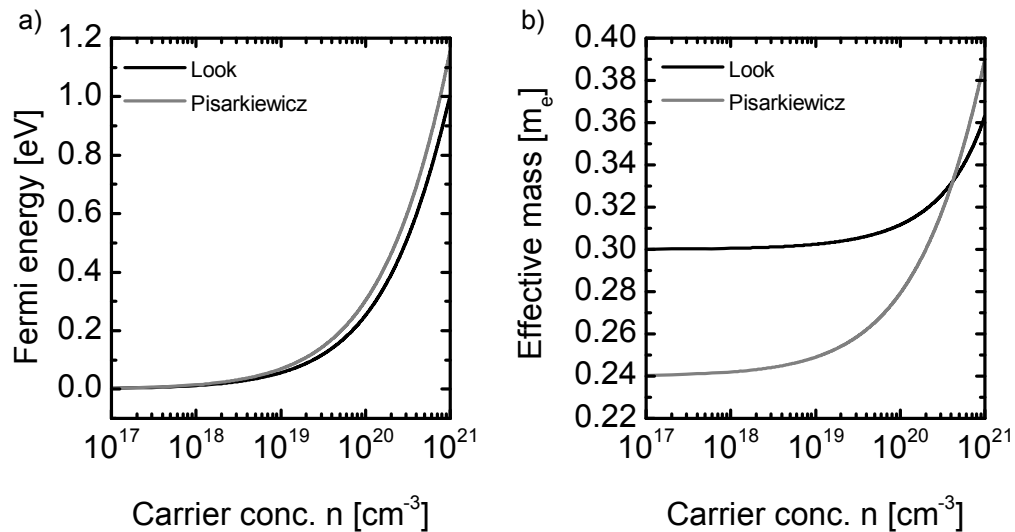


Figure 2.3: a) Fermi energy and b) effective mass as function of carrier concentration for ZnO according to the approaches of Look and Pisarkiewicz. The Fermi energy is given with respect to the conduction band minimum.

2 Physical and experimental fundamentals

Table 2.2: Overview of ZnO material parameters used for the mobility model of D. Look with the effective mass approaches according to Look and Pisarkiewicz.

Parameter	Look	Pisarkiewicz
'Effective mass' gap E_g	3.42 eV [33]	–
Effective mass at CBM m_0^*	$0.30 \cdot m_e$ [39]	$0.24 \cdot m_e$ [38]
Non-parabolicity factor C	–	0.27 eV^{-1} [38]
Static dielectric func. ϵ_r	$8.12 \cdot \epsilon_0$ [39]	
High frequency dielectric func. ϵ_1	$3.72 \cdot \epsilon_0$ [20]	
Polar-optical temperature T_{po}	837 K [20]	
Acoustic deformation potential E_1	3.3 eV [20]	
Piezoelectric constant P_{pe}	0.24 [20]	
Longitudinal elastic constant c_l	$1.4 \cdot 10^{11} \text{ N/m}^2$ [20]	

of Pisarkiewicz and Look (eq. 2.20 and 2.16, respectively) have been chosen.

The first one was selected since it represents a commonly used description of the non-parabolicity of the conduction band in ZnO [27, 37, 38]. Look *et al.* found their expression valid for a wide range of doped ZnO thin films as well as for single crystals. The explicit values for the parameters used for the mobility model of D. Look with the effective mass approaches according to Look and Pisarkiewicz can be taken from table 2.2. Regarding the variety of given effective masses for ZnO in literature, the assumptions of Pisarkiewicz and Look represent reasonable values for an upper and lower boundary of m^* . The Fermi energy and effective mass of both approaches are depicted in figure 2.3 over a wide range of carrier concentrations n .

For their considerations, they use different values of m^* at the CBM, leading not just to a different development but to an offset, too.

2.1.5 Optical properties

The structural and electrical characteristics of ZnO have a direct influence on the interaction of electromagnetic waves within the material. Due to its direct band gap of 3.2 – 3.5 eV it belongs to the group of wide band gap semiconductors. Together with the large exciton binding energy of 60 meV ZnO is an ideal candidate not just for TCO applications but for short-wavelength optical devices, as well.

Figure 2.4 shows typical spectra of transmittance, reflection and absorption of a highly doped ZnO:Al thin film on glass. Here, three regions can be distinguished and will be explained in the following.

(1) Fundamental absorption

If ZnO is excited with light of a wavelength below λ_G the energy is sufficiently large to induce a transition of electrons from the valence band to the conduction band. The wavelength λ_G corresponds in the case of an undoped and stoichiometric crystal to the energy of the electronic band gap E_{G_0} . This situation is depicted in figure 2.5 a). The energy E_{G_0} represents the minimum of required energy to cause a band-to-band transition of electrons. This process is also called fundamental absorption.

However, if, e.g. due to a high n-type doping concentration, the Fermi energy is pushed into the conduction band and ZnO becomes degenerate, all states close to the conduction band minimum are populated. According to the Pauli exclusion principle, these states are no longer available for electronic transitions from the valence band. Therefore, the 'apparent' band gap increases. This shift of optical band gap energy is called *Burstein-Moss effect* [40, 41] and is illustrated in figure 2.5 b).

This band gap widening is counteracted by exchange interactions between electrons and the interaction of the electrons with ionised impurities [42]. This situation is shown in figure 2.5 c). However, in degenerate ZnO:Al the Burstein-Moss effect dominates [42, 43] and

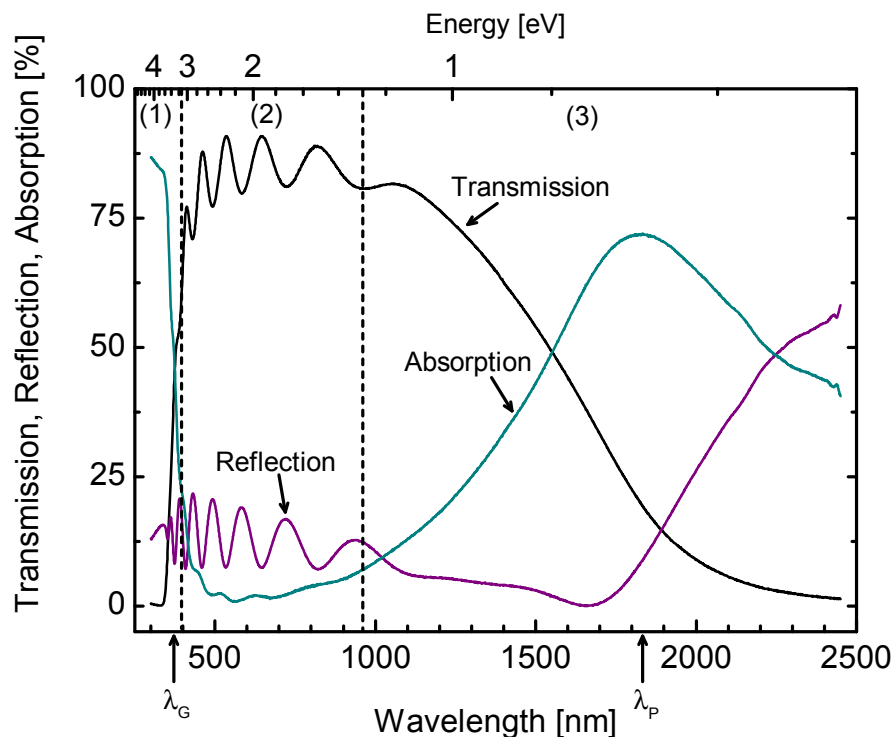


Figure 2.4: Exemplary optical transmittance, reflection and absorption of a ZnO:Al layer as function of photon wavelength and energy. The spectra can be divided into three regions: (1) fundamental absorption, (2) the optical window and (3) the free carrier absorption. For a more detailed explanation of the regions see text below.

2 Physical and experimental fundamentals

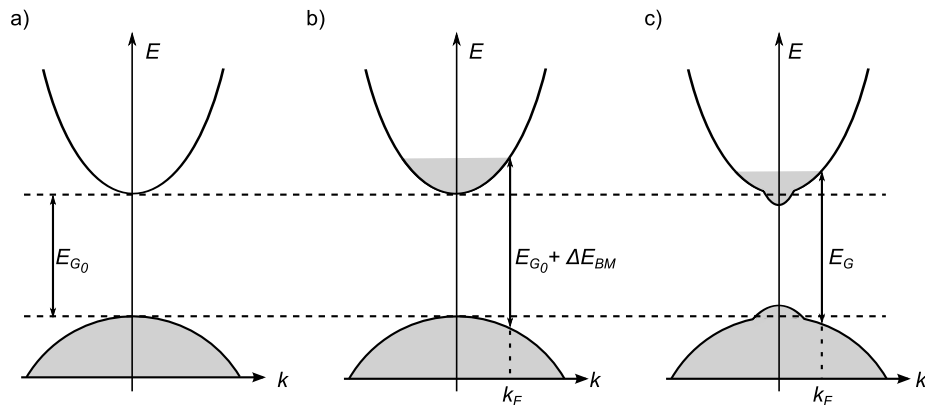


Figure 2.5: Fundamental absorption edge of a parabolic band structure for a) undoped semiconductor, b) degenerated semiconductor including Burstein-Moss shift and c) reduction of optical band gap by additionally considering many-body effects (see text); Figure according to Sernelius et al. [42]

the optical band gap energy E_G increases with raising carrier concentration.

Optical absorption near the band edge is actually determined by two processes: by the just explained band-to-band transition of an electron causing a continuous absorption spectrum with a rather sharp edge and the creation of excitons. The latter can be described as an excited electron bound to a hole via Coulomb interaction. The excitonic binding energy in ZnO is, with 60 meV, rather large [25]. Compared to the available thermal energy kT at room temperature of 25.6 meV it means that excitons in ZnO are stable at room temperature and provide an important feature for laser application.

For undoped semiconductors these excitonic states dominate the absorption below the fundamental absorption edge [44, 45].

However, for a highly, e.g. n-type doped, degenerated semiconductor these excitons are able to interact with the electron gas in the lowest conduction band states that drastically alters their binding characteristics and, therefore, the absorption near the band edge [46–48]. The free carriers screen the electron-hole attraction which may result in the case of highly doped semiconductors in dissociation of excitons. This process is also called *excitonic Mott transition* [23] and causes a vanishing of the excitonic absorption peak. However, it is believed, that even for semiconductors with very high carrier concentration the electron-hole pair is still able to form a bound state, the so-called *Mahan exciton* [46, 47]. Causing an absorption singularity at low very temperatures [46] it is assumed that the thermal energy at higher temperature and the finite lifetime of the excitons broaden this absorption edge abnormality [47, 48].

(2) Optical window

Photons with a wavelength larger than λ_G does not possess sufficient energy to excite elec-

trons from the valence into the conduction band, causing a strong decrease in absorption below 10 % and an increase in transmittance above 80 % . For up to a wavelength of around 1000 nm transmittance and reflection remain on a constant level only superimposed by interference features, caused by light reflected at front and back side of the ZnO layer. ZnO thin films behaves like a typical dielectric with a refractive index $n \approx 2$ on glass. This spectral region is called *optical window* and is of high interest regarding the application of the material as TCO.

(3) Free carrier absorption

In the near infrared region (NIR) the absorption increases again, reaching a maximum at $\lambda_P \approx 1800$ nm. In this area the *free carrier absorption* gains importance. Above a concentration of around $n \gtrsim 5 \cdot 10^{18} \text{ cm}^{-3}$ the electrons in ZnO can be approximated as free electron gas (see sec. 2.1.3). The absorption of light in this spectral region causes a collective excitation of these carriers [44, 49]. The associated wavelength λ_P of this oscillation of electrons is called plasma wavelength and is given by [50]

$$\lambda_P = \frac{2c\pi}{e} \sqrt{\frac{\epsilon_1 \epsilon_0 m^*}{n}}, \quad (2.31)$$

where c is again the speed of light, e the elementary charge, ϵ_0 the electric field constant and ϵ_1 the dielectric function at high frequencies.

The Drude theory [15] presents a good approximation to describe that interaction of an electric field with free electrons.

Introduction of the optical absorption coefficient

Generally, optical properties of a material are characterised by its interaction with electromagnetic waves. A theoretical description is given by *Maxwell's* equations.

An electromagnetic field \vec{E} causes an electric displacement field \vec{D} in the material, which is proportional to its dielectric function $\epsilon(\omega)$ and the electric field constant ϵ_0 :

$$\vec{D} = \epsilon(\omega)\epsilon_0\vec{E} = \epsilon_0\vec{E} + \vec{P}, \quad (2.32)$$

with \vec{P} as polarisation of the material.

The dielectric function $\epsilon(\omega)$ depends on the frequency ω of the interacting electromagnetic wave and possesses a real and imaginary part:

$$\epsilon(\omega) = \epsilon_1(\omega) + i\epsilon_2(\omega), \quad (2.33)$$

2 Physical and experimental fundamentals

which is connected to the complex index of refraction \tilde{n} by

$$\sqrt{\epsilon(\omega)} = \tilde{n} = n + i\kappa. \quad (2.34)$$

Here, n , denotes the real part of the refractive index, i.e. the phase velocity and κ the extinction coefficient, that accounts for the absorption loss when the electromagnetic wave propagates through the material.

The effect of the imaginary part of the refractive index can be demonstrated as following. Considering a homogeneously absorbing, isotropic material and light in the form of an electromagnetic plane wave propagating through it:

$$E(x, t) = E_0 \cdot \exp i(kx - \omega t) \quad (2.35)$$

$$\text{with } k = \frac{\tilde{n}\omega}{c} \quad (2.36)$$

$$\text{and } \tilde{n} = n + i\kappa, \quad (2.37)$$

then the amplitude of the wave decreases exponentially for positive κ :

$$E(x, t) = E_0 \exp\left(-\frac{\kappa\omega}{c}x\right) \cdot \exp\left(i\frac{\omega n}{c}x - i\omega t\right). \quad (2.38)$$

Therefore, the following applies for the intensity of the wave:

$$I(x) = I(0) \exp\left(-\frac{2\omega\kappa}{c}x\right). \quad (2.39)$$

The term in front of the spatial coordinate x is called *absorption coefficient* α :

$$\alpha(\omega) = \frac{2\omega\kappa}{c}. \quad (2.40)$$

Studying the absorption coefficient is attractive with respect to the characterisation of solid thin films. In contrast to the absolute absorptance, it is just dependent on material properties and not e.g. on the layer thickness. The issues regarding the experimental determination of it are discussed in detail in appendix A.

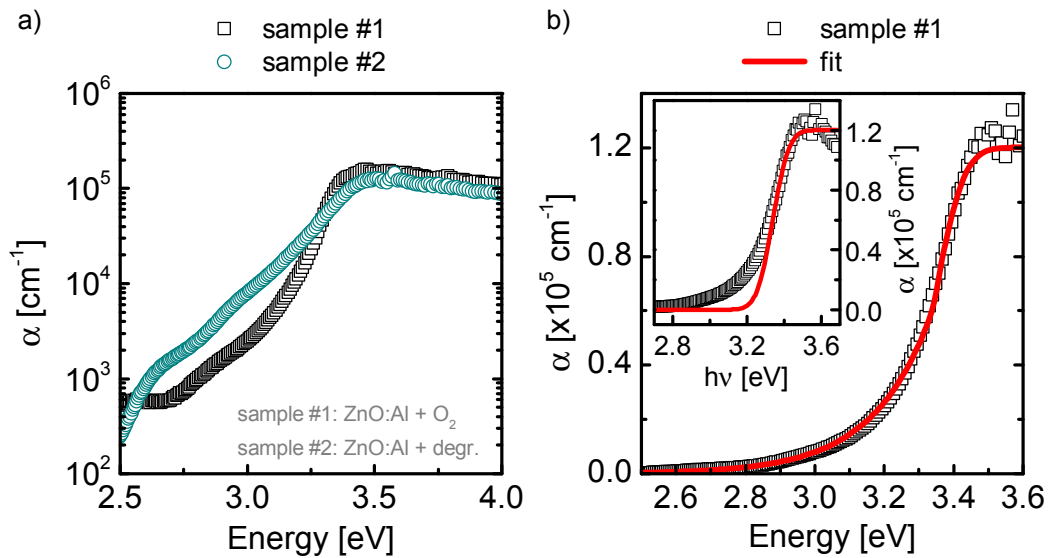


Figure 2.6: a) Absorption coefficient α , calculated from reflection and transmission measurements, of two exemplary samples with approximately the same band gap of 3.3 eV but different slopes of α at the fundamental absorption edge; b) Calculated absorption coefficient α and respective fit according to eq. 2.42 for sample #1; The inset shows a fit to the same sample using only the error function.

Determination of the absorption tail width

For a direct transition between valence and conduction band one actually expects no absorption below the band gap energy and, hence, a steeply rising fundamental absorption edge. For ZnO, as well as for a wide range of other semiconductors and insulators [51–55] it is observed, however, that optical absorption occurs below the band gap, exhibiting an exponential dependence on photon energy, and obeys the empirical Urbach relation [51].

For quantification, a conventional method is the fit of the linear section of the absorption coefficient in a semi-log plot with a linear function, where the slope is defined as Urbach energy [52, 56, 57]. However, while the upper boundary for the fit is usually the experimentally determined band gap energy, there is no consensus about an optimal lower limit for the fit which is always more or less freely chosen. For ZnO layer thicknesses above around 500 nm, interference effects arise within the band gap absorption. If the lower fit boundary is, then, not well adjusted, these interference fringes cause significant discrepancies for the determination of the Urbach energy (see appendix B).

Another issue disregarding a comparable determination of the Urbach energy is the calculation of the absorption coefficient itself. The most common method is the calculation via solely transmission or reflection [57–59] or using both, transmission and reflection measurements using Lambert-Beer's law in various modifications [60–62]. A more detailed description and discussion of this issue and interference in absorption spectra can be found in appendix A.

2 Physical and experimental fundamentals

Here, the absorption coefficient α has been obtained from transmission T and reflection R measurements via the inverse application of Lambert-Beer's law:

$$\alpha(E) = -\frac{1}{d} \ln \left(\frac{T(E)}{1 - R(E)} \right), \quad (2.41)$$

where d is the thickness of the ZnO layer. As discussed in appendix A, eq. 2.41 is just an approximation but describes the absorption coefficient of zinc oxide layers on glass correctly over a wide range of α . This includes the required range for analysis of Urbach energies.

Figure 2.6 a) shows the calculated absorption coefficient of two exemplary samples with approximately the same band gap of 3.3 eV. It can be clearly seen that sample #1 is characterised by a larger slope of the fundamental absorption edge than sample #2, caused by considerable parasitic absorption below the band gap energy. Additionally, it can be observed that the absorption onset possesses an asymmetric shape in the sense that the absorption disperses notably into the low photon energy regime. A full description, therefore, combines an Urbach tail expression for energies below and an error function above the band gap energy. Employing an error function is motivated by the fact that the derivative of the absorption coefficient can be fitted with a Gaussian function in order to derive the band gap energy [63]. The combined expression reads

$$\alpha(E) = \begin{cases} A \times \left(\operatorname{erf} \left(\frac{E - E_g}{\Gamma} \right) + 1 \right) & \text{if } E > E_0 \\ \exp \left(\frac{E - E_C}{E_U} \right) + \alpha_0 & \text{if } E \leq E_0. \end{cases} \quad (2.42)$$

For energies higher than E_0 , E_g describes the band gap energy, A is a fitting parameter denoting the maximum absorption and Γ specifies the broadening of the transition. For the sub-band gap absorption with $E < E_0$, E_U is the already mentioned Urbach energy, the measure of the energy range over which the absorption tails off. E_C is a numerically convenient way to introduce an amplitude for the exponential tail. α_0 represents a residual absorption.

It turned out that the attachment point on the energy scale of both functions, E_0 , is always smaller than the band gap energy E_g obtained by the fits. Therefore, it can be concluded that the error function is fitted just to values above the band gap E_g while the exponential absorption tail is obtained for the energy range below the E_g . A more detailed discussion of this issue can be found in appendix B.

An example of a fit using eq. 2.42 to experimentally obtained absorption coefficient data of an exemplary sample #1 is shown in figure 2.6 b). It can be seen that the proposed model represents the data reasonably well. The inset shows the same experimental data of sample #1 with a fit using the error function only. The discrepancy in the energy range below the band gap and the necessity to use a tail expression for an accurate description are obvious.

2.2 Experimental methods

This section describes the sample preparation and characterisation as well as the employed methods and equipment. All investigated samples are ZnO:Al thin films on glass prepared under various conditions in order to investigate the optoelectronic properties after application of thermal post-deposition treatments.

2.2.1 Sample preparation

2.2.1.1 Deposition of ZnO:Al

As substrate for ZnO:Al deposition Corning Eagle XG with a size of $10 \times 10 \text{ cm}^2$ has been chosen. Due to its high strain point of $669 \text{ }^\circ\text{C}$ [64], this material is very suitable for high temperature deposition and post-deposition treatments of ZnO.

In this thesis all investigated ZnO:Al films have been prepared by non-reactive magnetron sputtering from a circular planar ceramic target with a diameter of 250 mm and 1 %_{wt.} Al₂O₃. All processes were performed using rf-excitation of either pure argon or an argon-impurity mixture as sputtering gas. The discharge power was set in all cases to 750 W and the chamber pressure was maintained at $2.5 - 2.6 \cdot 10^{-3}$ mbar. During deposition, the substrate was rotating with 10 min^{-1} .

In order to investigate different specific problems and to create different material preconditions for later thermal post-deposition treatments, four major sample series have been prepared, all differing in their deposition conditions regarding substrate temperature and composition of sputtering atmosphere (table 2.3).

The 'temperature series' targeted the modification of morphology and composition achievable by applying a wide range of substrate temperatures during deposition.

Addition of oxygen and nitrogen to the growth process mainly aimed for the creation of acceptors, while hydrogen was added in order to study optical and electrical passivation effects.

To get clear information of both, optical and electrical measurements, the thickness of the studied ZnO:Al films in all experiments aimed to be between 600 and 700 nm. These relatively thick films produce interference fringes in reflection, transmittance and absorption spectra which impedes the evaluation of features at a low absorption level (see appendix A), but do not make them impossible. However, these film thicknesses allows an easier interpretation of their electrical properties, since the resistivity in this regime is not thickness dependent anymore and changes in carrier transport are determined by growth conditions and post-deposition treatments.

2 Physical and experimental fundamentals

Table 2.3: Division of samples investigated in this thesis into individual series

	Temperature series	Oxygen series
Substrate temperature	room temp. ³ - 500 °C	200 °C
Sputter pressure	$2.5 \cdot 10^{-3}$ mbar	$2.5 \cdot 10^{-3}$ mbar
Impurity gas concentration	—	O ₂ /Ar gas mixture, total O ₂ conc. 0 - 3 %
Ar gas flow	40 sccm	28 - 40 sccm
Cap material	a-Si:H	a-Si:H
Intention	changing preconditions for annealing by variation of substrate temperature	influencing stoichiometry to study possible impact of oxygen during annealing
Results in	section 3.1	section 3.2
	Nitrogen series	Hydrogen series
Substrate temperature	200 °C	100 °C, 100 - 500 °C ⁵
Sputter pressure	$2.6 \cdot 10^{-3}$ mbar	$2.5 \cdot 10^{-3}$ mbar
Impurity gas concentration	N ₂ , 1 - $60 \cdot 10^{-6}$ mbar ⁴	H ₂ , 0 - 10%
Ar gas flow	78 - 80 sccm	36 - 40 sccm
Cap material	a-Si:H	a-Si:H, a-Si, SiO ₂
Intention	investigation of nitrogen as possible driving factor during annealing	study influence of hydrogen on optical properties and impact on annealing when present in cap material
Results in	section 3.3	section 3.4

2.2.1.2 Deposition and removal of protective capping layers

Deposition

The idea to cover and anneal an ZnO:Al thin film with an amorphous silicon (a-Si) layer on top originates actually in the fabrication of silicon thin film solar cells based on the solid phase crystallisation (SPC) of silicon and the integration of ZnO:Al as transparent conductive front contact [65]. Here, the a-Si layer is transformed to polycrystalline silicon (poly-Si) through annealing at around 600 °C for 24 hours.

A side effect was the observation of considerably improved conductivity of the underlying ZnO layer [65]. Ruske *et al.* could show that instead of the 2 µm typically used in the SPC process, a 50 nm a-Si layer is already sufficiently thick to achieve comparable improvements [66].

Such protective capping layers have been employed in this work. Based on the SPC process and due to a suitable deposition rate those a-Si layers were standardly deposited by plasma enhanced chemical vapour deposition (PECVD). The deposition parameters for such a standard capping layer are given in table 2.4.

In chapter 3.4 the specific influence of hydrogen in the capping layer is studied. Therefore, a-Si layers deposited by electron beam evaporation⁶ have been additionally investigated since, compared to PECVD deposited a-Si:H, they are essentially hydrogen-free.

Table 2.4: Deposition parameters for a standard a-Si:H cap deposited by PECVD.

	standard a-Si:H cap
Substrate temperature	140 °C
Chamber pressure	3 mbar
Process gas	20 sccm silane (SiH ₄), 100 sccm H ₂
Plasma excitation	40 W, 13.56 MHz
Layer thickness	≈ 50 nm

³The specification room temperature (or RT) as used herein means that the sample was not intentionally heated.

⁴The N₂ gas supply was controlled by use of a needle valve. When the chamber base pressure was below 5·10⁻⁸ mbar, the valve has been opened until chamber pressure reached values as stated in the table above. Afterwards, the Ar gas flow controller was set to a total pressure of 2.6 ·10⁻³ mbar achieving N₂ concentrations in the sputtering gas of 0 – 2.5 %

⁵This temperature regime was used for the investigation of the influence of hydrogen in the cap material.

⁶For details about electron beam evaporation see [67]

2 Physical and experimental fundamentals

Cap removal by plasma-assisted dry etching

In order to enable the investigation of optical, electrical and structural properties of a cap-annealed ZnO layer, the prior deposited cap material has to be removed without damaging the ZnO layer itself. Due to the etchability of ZnO by acids and bases, a wet chemical removal of the protective layer is hardly possible. Therefore, a plasma-assisted dry etching step using NF_3 as etching gas has been employed which removes the silicon completely but leaves the ZnO layer undamaged. Two different PECVD chambers have been used to remove the a-Si:H capping layer. In both cases the chambers have been operated at room temperature and the cap removal corresponded to the standard cleaning process of the chambers only adapted in time.

2.2.1.3 Thermal post-deposition treatments

Thermal post-deposition treatments of ZnO have been widely applied and investigated with different results in the past, but their underlying mechanisms are still not fully understood.

The optoelectronic properties after annealing are strongly dependent on the used temperature regime, treatment duration and the composition of the annealing atmosphere. Generally improved optoelectronic properties after annealing are mostly related to sol-gel fabricated ZnO films [68–70]. An increase of conductivity for sputtered or PLD⁷ ZnO was found just for moderate temperatures in nitrogen atmosphere [71] or for higher temperatures in vacuum or hydrogen-containing atmospheres [72–74].

If ZnO is annealed in nitrogen and oxygen at high temperatures, a decrease of conductivity is observed [66, 74, 75] which is partially reversible if the films are subsequently annealed in hydrogen [76, 77].

Application of a capping layer, as already mentioned above, effectively protects the ZnO:Al from the influence of the annealing atmosphere [65, 66]. Furthermore, it could be shown by Wimmer *et al.* [78, 79] that the application of both treatments subsequently, first annealing

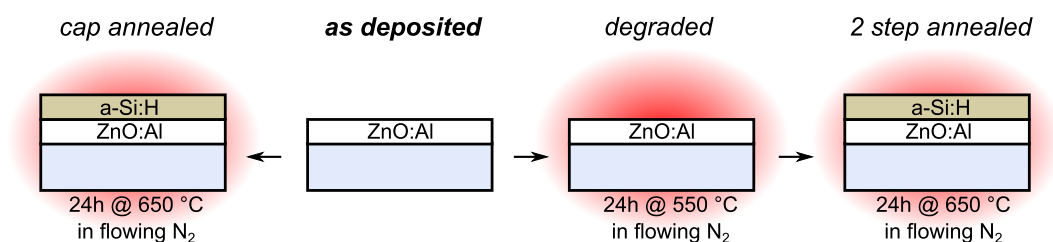


Figure 2.7: Illustration of the sample preparation procedure in case of thermal post-deposition treatments

⁷Pulsed Laser Deposition

without than with a protective capping layer, represents a suitable technique to tailor the optoelectronic properties of ZnO for TCO applications.

In the present work, applied heating processes were all carried out in a customised convection oven of HTM Reetz GmbH, Berlin, which reaches stable temperatures up to 700 °C. Since the thermal stability of the substrate has to be considered, all applied treatments have been set to temperatures below 650 °C. The heating power is controlled by monitoring of target and actual temperature. The loading of the oven usually took place at room temperature. Afterwards, the plateau temperature was approached with constant heating rates of 2.5 K/min up to 250 °C and 1.4 K/min above 250 °C. Since it does not possess any active cooling, the cooling rate was restricted. During heating, actual process and cooling the oven was permanently floated with nitrogen. However, the oven has not been evacuated before. Hence, contamination of the annealing atmosphere with hydrogen, oxygen and carbon can be expected.

In this work, three main annealing processes have been employed which are depicted in figure 2.7. Starting from the *as deposited* state, the *degradation* process denotes a heating step at 550 °C for 24 hours of the bare ZnO:Al film on glass.

For the *cap annealing*, the ZnO layer is coated with an a-Si protective cap, as described in the subsection above, and afterwards annealed at 650 °C for 24 hours.

The so-called *2 step annealing* consists of a standard degradation step and a subsequently applied cap annealing.

2.2.2 Characterisation methods

2.2.2.1 Optical characterisation

The optical characterisation of the samples was carried out by means of reflection and transmittance measurements using a high-performance Lambda 1050 double beam spec-

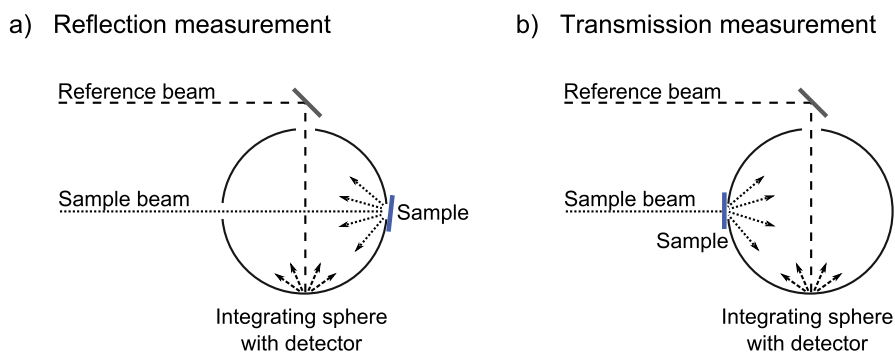


Figure 2.8: Schematic representation of setup configuration of a) reflection and b) transmittance measurements using an integrating sphere in a double beam spectrophotometer

2 Physical and experimental fundamentals

trophotometer of Perkin Elmer. This device covers a spectral range from 175 nm up to 2500 nm. The wavelength of 175 – 320 nm are generated by a deuterium lamp, the range of 320 – 2500 nm by a halogen lamp.

The light passes a monochromator and illuminates the sample perpendicularly in case of transmittance measurements and under an angle of 7° for reflection measurements. The transmitted or reflected light is spatially integrated (figure 2.8). The detection in the ultra violet and visible range (175 – 860 nm) occurs via a photomultiplier with an accuracy of 0.08 nm. For the near infrared region (860 – 2500 nm) an InGaAs detector is employed having a spectral resolution of 0.3 nm. However, the spectral resolution of the measurement is as well given by other setup configurations as gratings and slit widths. Overall, a measurement accuracy of 2 nm can be assumed.

All measured spectra are given relatively to a calibration measurement. For this, no sample is situated in the beam path in case of transmittance measurement and a white standard is used in case of calibrating the reflection measurement.

2.2.2.2 Electrical transport measurements

Four-point probe

For resistivity measurements, a four-point probe has proven to be a convenient tool. As the name suggests, the setup configuration consists of four probes. These are situated in a row whereas the outer two probes introduce a current I and the inner two measure the potential drop U .

The in this work employed setup Jandel RM3-AR uses a measuring head where the probes possess a tip radius of 40 μm and a separation of 1 mm. The characterised zinc oxide samples had at least a size of $2.5 \times 2.5 \text{ cm}^2$ and a thickness d between 600 and 700 nm. Therefore, the samples could be considered as 'thin' and the ZnO film as infinitely large with respect to the dimensions of the probe head.

Under these conditions, the sheet resistance ρ_{sh} is given by [80]

$$\rho_{\text{sh}} = \frac{\rho}{d} = \frac{\pi}{\ln 2} \cdot \frac{U}{I}. \quad (2.43)$$

To obtain the resistivity ρ the sheet resistance ρ_{sh} has to be multiplied with with the layer thickness d . The error of the resistance measurement due to measurement accuracy of the instrument is given with 0.3 %.

Hall measurements

As explained in section 2.1.3, the resistivity of a material is given by its carrier concentration n and carrier mobility μ :

$$\rho = (n\mu e)^{-1}, \quad (2.44)$$

with e as elementary charge. By resistivity measurements, just the product of carrier concentration and mobility $n \cdot \mu$ can be obtained but not the individual variables themselves. However, concentration of carriers and their mobility can be determined by means of Hall effect measurements in van-der-Pauw geometry [81]. This measurement configuration uses four point contact that get attached at the edges of a sample. The sample's geometry is not important as long as the following requirements are met:

1. The sample is singly connected, i.e. it has a smooth surface without any isolated holes or cracks.
2. The sample is homogenous in thickness.
3. The contacts are installed within the edges of the sample.
4. The ratio of contact size to sample size is sufficiently small.

The measurement method itself and an estimation of the obtained errors are discussed in detail in the work of van der Pauw [81].

Here, square samples with a side length of 5 mm have been used. The relative errors scale with the ratio of contact size to sample size and can be estimated according to *van der Pauw* as following:

$$\begin{aligned} \frac{\Delta\rho}{\rho} &< 1 \%, \\ \frac{\Delta\mu}{\mu} &\leq 5 \%, \\ \frac{\Delta n}{n} &\leq 5 \%. \end{aligned}$$

All Hall measurements have been carried out using a HMS-3000 setup by Ecopia in air and at room temperature. Prior to each measurement, a control measurement has been performed to ensure ohmic contacts.

2 Physical and experimental fundamentals

2.2.2.3 Raman spectroscopy

The Raman effect or Raman scattering describes the inelastic scattering of light with phonons in a solid [44, 82]. Photons scattered from an atom are mostly scattered elastically, this means, the scattered photons possess the same energy as the incident ones. This process is called Rayleigh scattering. However, a small fraction of photons get scattered inelastically and energy transfer takes place. Depending on the direction of transfer, the Raman effect is divided into Stokes and anti-Stokes scattering. Figure 2.9 depicts the most important scattering processes of light with phonons.

- **Stokes shift:** Energy is transferred from photons to phonons, leaving the phonons in an excited state and the photons with a reduced frequency ν_S in respect to the incident photons with ν_i .
- **anti-Stokes shift:** Energy is transferred from a phonon to a photon. The frequency of the emitted photons ν_{AS} is increased with respect to the incident photons while the phonons are in a lower energy level after scattering.

In general, Raman scattering can be understood as a three-body-process where an electron is excited to a virtual electronic intermediate state and then scattered by a phonon. Therefore, the scattering probability is very low. However, the scattering probability is significantly enhanced when the energy of incident photons is chosen in the vicinity of real electronic states, for example close to the band gap energy or defect states within the band gap. Then, interaction takes place and the Raman scattering cross section is enhanced [82, 83].

For Stokes and anti-Stokes Raman scattering energy and momentum conservation apply:

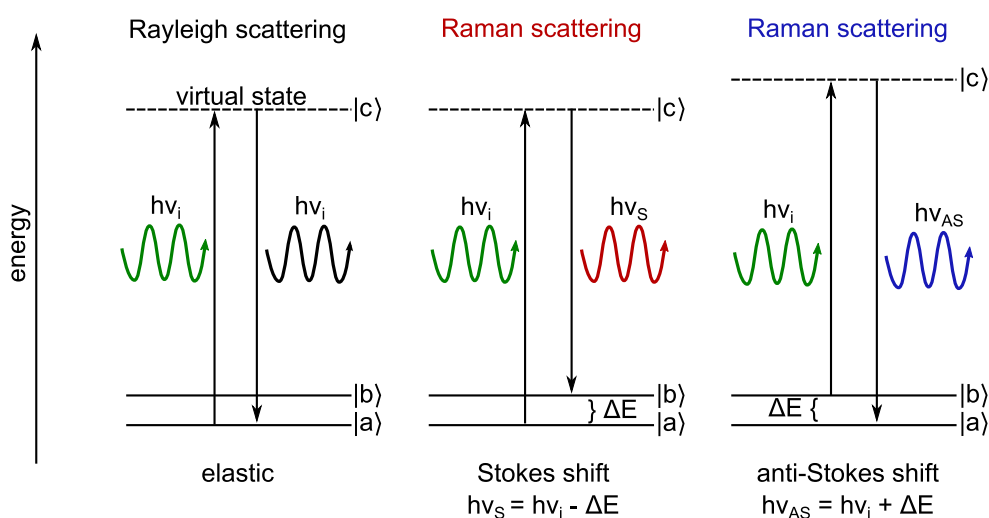


Figure 2.9: Scattering processes of light with phonons: elastic Rayleigh scattering and Raman scattering with Stokes and anti-Stokes shift

2.2 Experimental methods

$$h\nu_S = h\nu_i - h\Omega \quad \text{and} \quad \vec{k}_S = \vec{k}_i - \vec{q} \quad (2.45)$$

$$h\nu_{AS} = h\nu_i + h\Omega \quad \text{and} \quad \vec{k}_{AS} = \vec{k}_i + \vec{q}. \quad (2.46)$$

Ω and \vec{q} are frequency and wave vector of the respective phonon mode. $\vec{k}_{i/S/AS}$ are the wave vectors of the incident photons and the photons scattered via Stokes or anti-Stokes processes. Usually, monochromatic and coherent lasers with a wavelength in the visible range are used as light source for Raman spectroscopy of solids. The wavelength of the light is some orders of magnitude larger than the interatomic distance (lattice constant a) in a typical crystal ($\lambda_i \gg a$). Therefore, the magnitude of its wave vector k_i is much smaller than the dimensions of the Brillouin zone q_{BZ}

$$|\vec{k}_i| = k_i = \frac{2\pi}{\lambda_i} \approx 10^6 \text{ cm}^{-1} \ll q_{BZ} = \frac{2\pi}{a} \approx 10^8 \text{ cm}^{-1}. \quad (2.47)$$

Accordingly, one-phonon Raman scattering probes only excitations close to the center of the Brillouin zone [44]. For simplicity and since the Stokes shift has a larger scattering cross section [84], the following considerations are made just for the Stokes shift but apply for the anti-Stokes shift in a similar way. The total intensity I_s of Raman scattered light depends on the polarisation of incident and scattered radiation \vec{e}_i and \vec{e}_s , and electronic structure, hence, the lattice symmetry of the material [83]:

$$I_s \propto |\vec{e}_i \cdot \mathcal{R} \cdot \vec{e}_s|^2, \quad (2.48)$$

with \mathcal{R} is known as Raman tensor. It is a second-rank tensor which results from the electrical susceptibility χ :

$$\mathcal{R} = \left(\frac{d\vec{\chi}}{d\xi} \right), \quad (2.49)$$

where ξ is a unitary vector parallel to the atomic displacement and, hence, reflects the crystal symmetry. From eq. 2.48 lattice specific selection rules can be derived for Raman spectroscopy. For ZnO they are listed in table 2.1.

In this thesis a S & I TriVista Raman spectrometer with an argon ion laser source and a wavelength of 488 nm has been used. With this setup and configuration, a spectral resolution of less than 1 cm^{-1} was achieved. All data have been obtained in back scatter geometry and with a spatial resolution of around $1 \text{ }\mu\text{m}$.

2 Physical and experimental fundamentals

2.2.2.4 X-ray diffraction

For the structural analysis of the thin films, X-ray scattering is widely employed. Electromagnetic radiation impinging on a periodic arrangement of atoms causes a regular array of spherical waves. When the incident radiation is coherent and the wavelength in the order of the interatomic distances in the crystal, which would be the case for X-rays, these waves cancel out in most directions through destructive interference but interfere constructively in specific directions governed by Bragg's law:

$$2 \cdot d_{hkl} \cdot \sin\theta = n \cdot \lambda, \quad (2.50)$$

where d_{hkl} is the interplanar distance and n an integer, also called diffraction order. The angle θ is commonly called Bragg angle. The position of the diffraction maxima is, therefore, highly sensitive on the orientation of the crystal. Information about microstructural properties can, in generally, not just be derived from the peak position, but also from width and intensity [86]. The width of a diffraction reflex essentially depends on the number of coherently scattering lattice planes. However, apparative broadening and defect related microstress also have to be taken into account [85]. The often used Scherrer equation [87] for determination of grain size from the width at half maximum of a diffraction reflex can, therefore, be understood only as a rough estimation and lower limit of the grain size. It provides not necessarily more information than the simple evaluation of the peak widths. The intensity is mainly influenced by the amount of crystalline material that is measured. Hence, it is dependent on the layer thickness and angle of incident radiation. Furthermore, it is impaired by the inclination of the grains, i.e. slightly tilted crystallites may not be detected anymore. Hence, the diffraction intensities of the investigated ZnO layers are very difficult to analyse and have not been considered in this work.

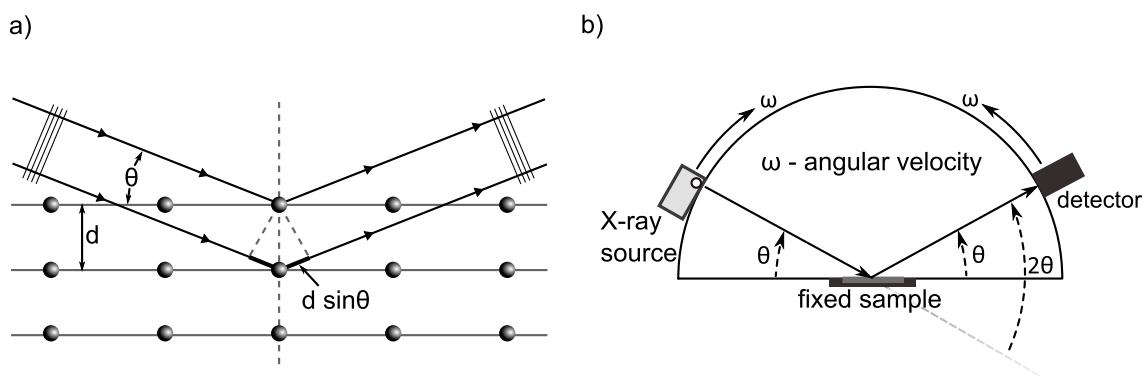


Figure 2.10: a) Illustration of diffraction conditions according to Bragg (eq.2.50); b) Bragg-Brentano focusing geometry, images according to [85]

2.2 Experimental methods

For experimental determination of the X-ray diffraction spectra a X'Pert Pro diffractometer of PANalytical with Bragg-Brentano focusing geometry is used where the sample's position is fixed and X-ray source and detector are moving on a semicircular arc. The setup is depicted in figure 2.10 b). For detection, a silicon pixel detector 'PIXcel' was employed. The spectra have been recorded in an angular range between $29^\circ \leq 2\theta \leq 75^\circ$ with an increment of 0.013° . Recording time per θ increment and aperture configuration behind the X-ray source and in front of the detector remained unmodified for each sample.⁸ As X-ray source a copper source was used. Utilisation of a selective metal filter, in this case nickel, monochromates the radiation to $\text{Cu } K\alpha_1$ and $\text{Cu } K\alpha_2$. To gain information on the crystal orientation of the investigated ZnO films, the experimental obtained data is compared to well-known powder spectra in literature (e.g. [88]).

⁸Behind X-ray source: divergence slit with 0.38 mm, Soller slit of 0.04° , apertures with $1/4^\circ$ and 5 mm; in front of detector: Soller slit with 0.04° , nickel filter

3 Physical properties of ZnO:Al thin films after application of thermal post-deposition treatments with and without protective capping layer

To gain a deeper understanding of the processes occurring in ZnO:Al during annealing, the main focus for the as deposited material was set on a variation of the substrate temperature and a systematic addition of oxygen, nitrogen and hydrogen, respectively, during deposition. The content of this chapter is the structural, electrical and optical characterisation of ZnO:Al thin films in the as deposited state and after application of thermal post-deposition treatments with and without protective capping layer in dependence on the deposition conditions. Except for section 3.4, PECVD amorphous silicon has been used as capping material.

The temperature during growth has a strong impact on the crystal quality and optoelectronic properties of the material. To what extent the results of thermal annealing are affected, will be the focus of the first subsection. It will answer the questions how far low temperature deposited, low-quality ZnO:Al can be improved and whether there are differences between ZnO:Al films deposited at high temperature and layers that were deposited at low temperatures but afterwards annealed. The collection of the samples whose properties are discussed in this section are hereafter referred to as '*temperature series*'.

Since the stoichiometry of the ZnO:Al is known to have a great impact on the physical properties of the material, the effect of variation of oxygen partial pressure during deposition will be discussed in the second section. This part refers to a series of samples produced with the name '*oxygen series*'.

In the third section attention is given to the role of nitrogen in ZnO:Al. It is known to have a great impact on the optical properties and can cause a yellowish to brownish colouring of ZnO:Al. To clarify whether nitrogen in the annealing atmosphere has an influence on optical and electrical properties during annealing, it has been intentionally added to the ZnO:Al growth process. The samples in this section, therefore, belong to the '*nitrogen series*'.

Since hydrogen is present in capping materials deposited using hydrogen containing precursors as in the PECVD process, the impact of hydrogen on untreated ZnO:Al has been

3 Change of physical properties of ZnO:Al thin films after thermal treatments

investigated in section 3.4 by means of the 'hydrogen series'. Since it was reported that hydrogen in the cap material is expected to cause the enormous improvement of electrical properties during cap annealing [66, 89], essentially hydrogen-free electron beam evaporated silicon capping layer have been employed to study the impact of hydrogen in the cap material, further.

3.1 Influence of the substrate temperature during deposition

3.1.1 Electrical, optical and structural properties in the as deposited state

For the ZnO:Al films of the *temperature series* the substrate temperature was varied over a wide range, from room temperature (RT) up to 500 °C, and characterised regarding their structural and optoelectronic properties before and after annealing.

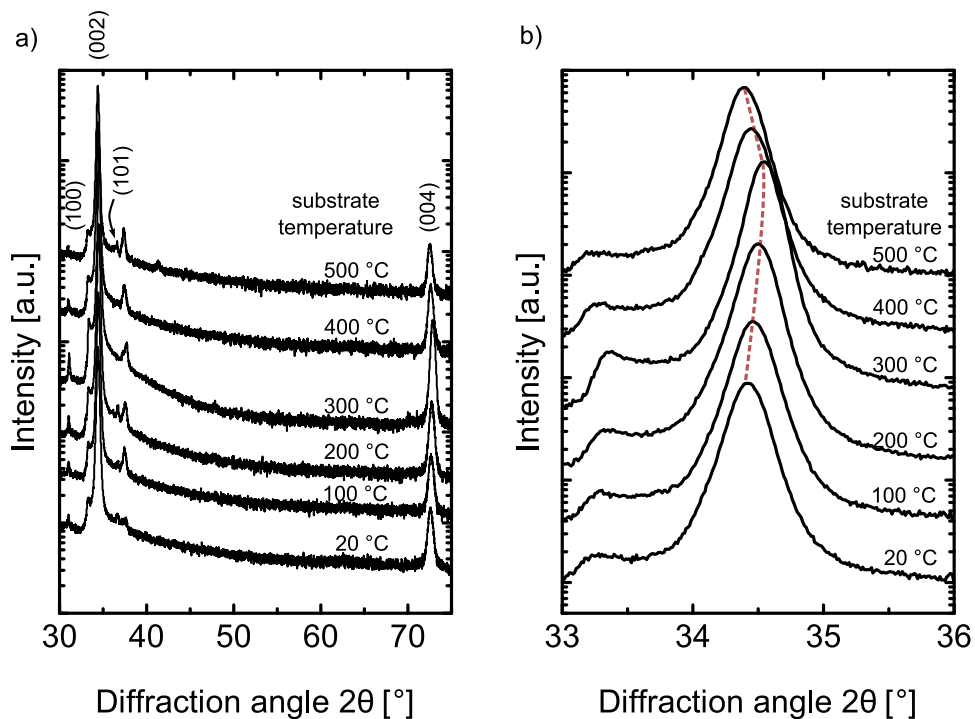


Figure 3.1: a) X-ray diffraction spectra between 30° and 75° and b) around the (002) reflex as function of the substrate temperature. The shift in position of the (002) reflex is indicated with a red dashed line. All spectra are normalised to their respective layer thickness and vertically shifted for clarity.

3.1 Influence of the substrate temperature during deposition

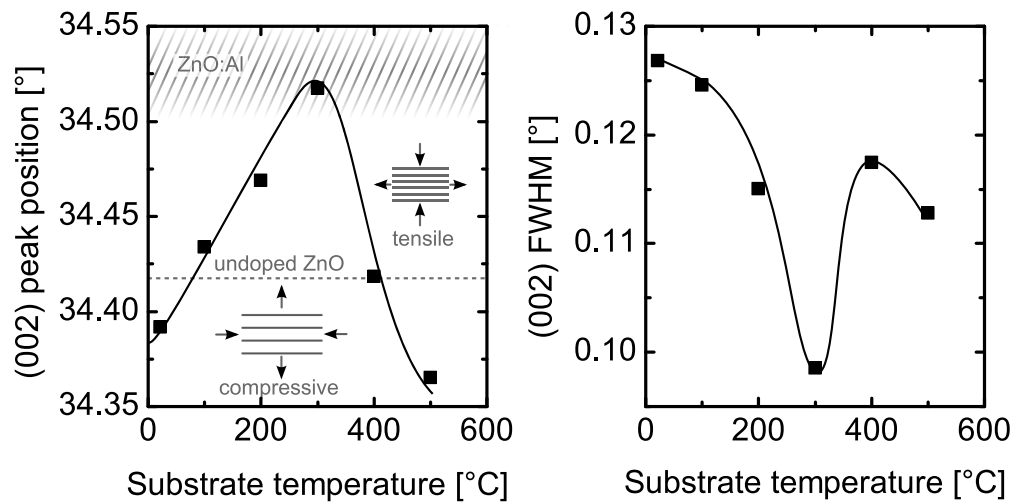


Figure 3.2: Peak position and FWHM of the (002) reflex as function of substrate temperature; The included lines are guides to the eye; The illustrations of tensile and compressive strain are with respect to the undoped ZnO reference.

Structure, Part I - X-ray diffraction

Figure 3.1 shows X-ray diffraction spectra from a) $2\theta = 30 - 75^\circ$ and b) a magnification of the (002) reflex in the range of $2\theta = 33 - 36^\circ$ for all samples in the as deposited state without further treatment. All ZnO:Al films are highly c-axis oriented, as seen by the strong domination of the (002) and (004) reflexes. Furthermore, a small (100) peak at 31° is observable, increasing up to $T_S = 300^\circ\text{C}$ and decreasing for higher substrate temperatures. Additionally, reflexes at around 36.24° , belonging to the (101) direction are visible.

The small feature appearing around 37.5° seems to be an artifact caused by the used XRD setup, as its appearance could not be reproduced in a repetition of the experiment on a different setup⁹.

The highly oriented growth can be traced back to the two stages of film growth, the initial growth, nucleation and coalescence during the first few nanometers, and the actual film growth. Due to different growth rates of different planes and their competition during nucleation only 'the fastest survives' [90, 91] which, in this case, is preferential growth of [001] planes.

A magnification of the angular area around the (002) reflex, as can be seen on the right side of figure 3.1, reveals a shift of the peak's position with change of growth temperature. The left part of figure 3.2 shows that position as function of the substrate temperature during deposition. Up to $T_S = 300^\circ\text{C}$ the peak shifts towards higher diffraction angles, while a further increase inverts that trend. Comparison of the shift relative to the reflex position of unstrained material would provide information about stress in the sample. Tensile strain

⁹RWTH Aachen, Roland Sittner

3 Change of physical properties of ZnO:Al thin films after thermal treatments

parallel to the substrates surface leads to a reduction in distance between the (001) planes in the crystal. Compressive strain on the other hand, results in an increased distance. According to equation 2.50, tensile strain is related to a shift to larger angles, compressive strain on the other hand to smaller angles.

However, the determination of a reference (002) reflex position for unstrained ZnO:Al is not trivial. For undoped ZnO, the (002) position is well known with 34.422° [88]. For highly aluminium doped ZnO one has to keep in mind that Zn^{2+} with an ionic radius of 72 pm is partially replaced by Al^{3+} with an radius of 53 pm [91]. A substitution of Zn by Al, therefore, results in a c-axis reduction so it can be assumed that the (002) position for ZnO:Al is not the same as for undoped ZnO. Earlier works suggest that the reflex position for unstrained ZnO:Al deposited from a target with 1 %_wt Al should be around 34.5° [92–94].

For further considerations the reference position of unstrained ZnO:Al has to be taken into account. Since it is not accurately known, it has been illustrated as shaded area around 34.5° in figure 3.2 a). Since the reflex positions of the samples investigated here are all smaller than that reference, all samples are assumed to be under more or less pronounced compressive stress. This compressive stress is more pronounced for room temperature deposited layers and appears to be reduced for increasing substrate temperatures during growth up to $300^\circ C$. A further increase of growth temperature seems to establish this stress again. These tendencies are known and already reported in literature [94, 95].

Deposition at low substrate temperatures causes a reduced diffusivity of the adatoms during the growth process resulting in a high growth rate but high porosity and highly compressive strained layers [96]. Supply of thermal energy during growth, therefore, yields more compact and less strained layers.

Furthermore, it is known that during sputter deposition the sputter gas, in this case argon, is implanted into the lattice resulting on one hand again to a reduced surface mobility of Zn and Al and on the other to an expansion of the lattice by exerting forces in all directions in space, since they occupy mainly interstitial sites [97]. Both effects induce compressive stress in the layers.

At elevated substrate temperatures compressive strain is not just reduced by improved

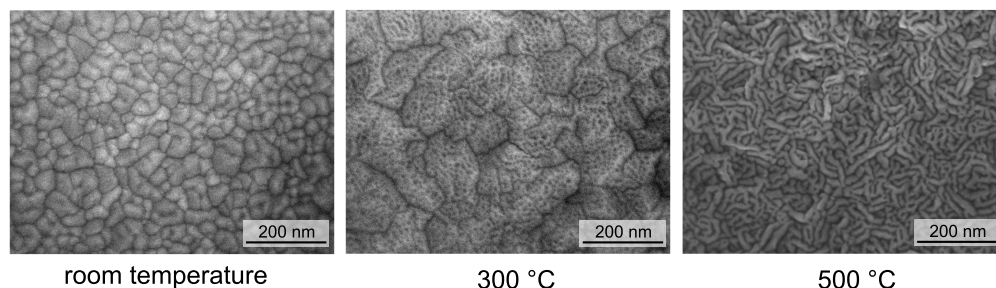


Figure 3.3: Surface SEM micrographs of ZnO:Al layer deposited at room temperature, $300^\circ C$ and $500^\circ C$

3.1 Influence of the substrate temperature during deposition

crystal growth and annealing of implantation defects but is as well substrate related. For all experiments, Corning Eagle XG glass has been used since it is thermally stable up to temperatures above our purposes. However, this substrate possesses a considerably small thermal expansion coefficient compared to ZnO [64, 98]. The mismatch up to 300 °C is around 35% leading to tensile stress depending on the temperature difference between measurement and deposition temperature. The lattice constant parallel to the substrate gets dilated, compressing the lattice parameter perpendicular to substrate according to Poisson's ratio and counteract, therefore, the compressive load due to sputter gas ion incorporation and residual porosity. Considering a shift in (002) position to at least 34.5° in stress-free state just due to Al doping, it seems that a deposition temperature of 300 °C yields nearly unstrained ZnO:Al films.

A change of growth behaviour can also be obtained from the FWHM of the (002) reflex as shown on the right side of figure 3.2. The width is determined by the size of the coherent scattering areas, stress within the crystallites and an instrument-based contribution. Since it is not just dependent on the crystallite size, the widely employed Scherrer formula [87] for determination of the grain size is not applied in this work.

However, for increasing substrate temperature up to 300 °C, a decrease in FWHM can be observed, indicating an improved crystallinity. Crystal growth starts to deteriorate at substrate temperature above 400 °C, resulting in again broadened reflexes. These results correlate very well with the morphology of the thin films obtained by SEM micrographs (fig.3.3). Here, the apparent grain size reaches its maximum for a substrate temperature of 300 °C. Lower and higher deposition temperatures yield smaller and, in case of 500 °C, in shape modified grains.

Structure, Part II - Raman spectroscopy

A modification in crystal structure is also observable employing Raman spectroscopy which is sensitive to the change of vibrational properties of the lattice.

Since the films investigated here possess a highly c-axis orientated wurtzite structure, in back scatter geometry only the E_2 modes at 99 cm^{-1} and 437 cm^{-1} , and the $A_1(\text{LO})$ at 574 cm^{-1} are Raman active [5]. Figure 3.4 shows an overview of Raman spectra between 80 and 700 cm^{-1} of ZnO:Al layers deposited between room temperature and 500 °C. The shape of occurring resonances change significantly with increasing substrate temperature. Next to the expected resonances in this measurement configuration at 99, 437 and 574 cm^{-1} additional modes (AM) appear. These are assigned with an asterisk.

Mode at 574 cm^{-1}

Although being a Raman resonances allowed in this configuration, the longitudinal optical (LO) phonons possess usually, a low Raman intensity, due to their high polarity [99]. Therefore, a pronounced appearance of a resonance around 574 cm^{-1} is rather unexpected. However, broad and asymmetric resonances in this spectral region are observed especially for those ZnO:Al films deposited below 300 °C. Higher substrate temperatures suppress the

3 Change of physical properties of ZnO:Al thin films after thermal treatments

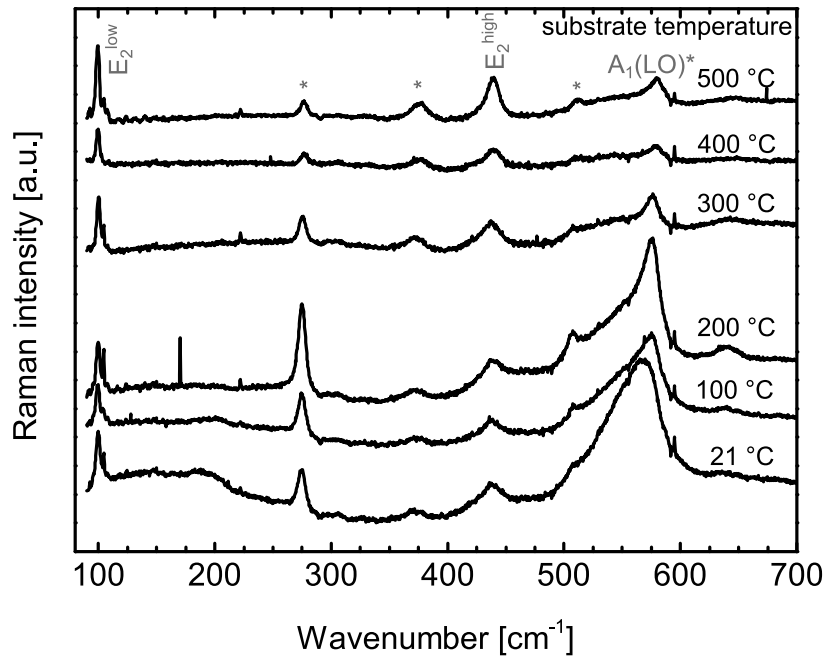


Figure 3.4: Raman spectra in the range between 100 cm^{-1} and 750 cm^{-1} for all samples of the temperature series in their as deposited state

development of that mode.

These results are consistent with those from the literature. It was found that this mode appears in heavily doped ZnO [100] and also in defect-rich grown ZnO [101] or in ZnO implanted with ex- or intrinsic atoms [102, 103]. Furthermore, it was shown that its intensity can be reduced significantly by thermal treatments [102].

Due to different experiments, various reasons for the occurrence of this resonance are given in literature among them electrical field effects [104], local defect modes and nitrogen incorporation [105] and disorder activated B-modes [106]. The most plausible reason was given by Friedrich *et al.* [99, 101] They ascribed the observation of the AM around 574 cm^{-1} to a defect induced Fröhlich-interaction [44] causing a defect-induced amplification of the LO-modes. The defects involved only have to possess energy states within the band gap of ZnO.

Mode at 275 cm^{-1}

For deposition temperatures below 300 °C , a pronounced mode around 275 cm^{-1} is visible whose intensity declines for substrate temperatures above 300 °C .

This resonance is controversially discussed in literature. Kaschner *et al.* [105] assigned the appearance of AMs at 275 cm^{-1} to the incorporation of nitrogen. Additionally, Friedrich *et al.* [107] showed by means of Zn isotope experiments and DFT calculations that a Raman mode at 274 cm^{-1} can be attributed to the oscillation of interstitial Zn atoms bound to

3.1 Influence of the substrate temperature during deposition

substitutional nitrogen ($Zn_{1-x}N_xO$). However, an assignment of this resonance to N alone cannot hold since Bundesmann *et al.* [100] observed an AM at 275 cm^{-1} in ZnO doped with group III and V elements without addition of nitrogen. Another explanation suggests that these modes arise from the activation of originally Raman-silent B-modes due to a broken translational symmetry of the lattice since they can be observed in other wurtzite structures, as well [104, 106].

A completely different approach is given by the work of Gluba *et al.* [108], where they assigned the AM at 275 cm^{-1} to the oscillation of interstitial zinc clusters.

Mode at 378 cm^{-1}

The AM at 378 cm^{-1} could be attributed to the $A_1(\text{TO})$ phonon which would only be observable in this measurement geometry if the crystallites structure deviates from c-axis orientation. However, XRD measurements showed that next to $[001]$ the only detectable other growth direction was $[100]$. The intensity of the corresponding diffraction reflex, however, decreases significantly while the AM at 378 cm^{-1} enhances with increasing deposition temperature. While an assignment of the 378 cm^{-1} resonance to the $A_1(\text{TO})$ phonon mode seems quite unlikely one has to keep in mind that XRD is just sensitive to perfectly oriented crystallites. Raman spectroscopy, however, is able to detect smaller deviations from the preferential orientation. Hence, the attribution of this AM to the $A_1(\text{TO})$ phonon mode cannot be excluded.

Electronic transport

Figure 3.5 shows the electron concentration n , electron mobility μ and resistivity as function of the substrate temperature during deposition for the as deposited ZnO:Al thin films. The

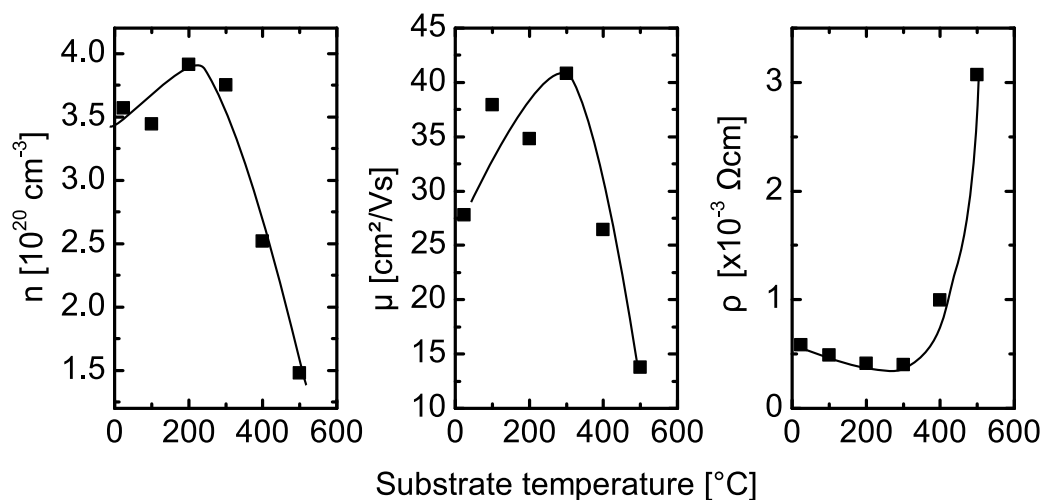


Figure 3.5: Carrier concentration, mobility and resistivity as function of substrate temperature for aluminium-doped zinc oxide in the as deposited state

3 Change of physical properties of ZnO:Al thin films after thermal treatments

highest mobility of $40.8 \text{ cm}^2/\text{Vs}$ was obtained for the sample deposited at 300°C . The best electrical properties coincides with the minimum of the XRD (002) FWHM, indicating that the best crystallinity yields the best electrical properties. As seen for the FWHM of the (002) reflex and on the SEM micrographs, grain growth starts to deteriorate at substrate temperatures above 300°C and so do the electrical properties. However, this correlation is not generally valid as will be shown for thermally annealed samples in the following subsection.

An initial improvement of electrical properties up to a certain threshold growth temperature and a strong deterioration afterwards is already known and published in various publications ([109, 110]). At which specific temperature the maximum is located, depends on the target doping concentration which has a strong influence on film growth and structural properties [94]. As can be found in several publications, the amount of Al in sputtered ZnO:Al from a ceramic target is almost independent of the deposition conditions and nearly the same as in the target, at least up to substrate temperatures of 250°C [91, 111]. Therefore, it can be assumed that the change of carrier concentration with variation of substrate temperature is mainly caused by a different activation of Al as dopant or the creation of acceptor-like defects.

Sub-band gap absorption

As already described in chapter 2, section 2.1.3, the optical properties of ZnO are very closely connected to the change in carrier concentration and mobility. The influence of the carrier concentration onto the position of the fundamental absorption edge of highly doped ZnO films [42, 63, 112] and the behaviour of the infrared free carrier absorption as function of carrier concentration, mobility and scattering mechanism have been studied

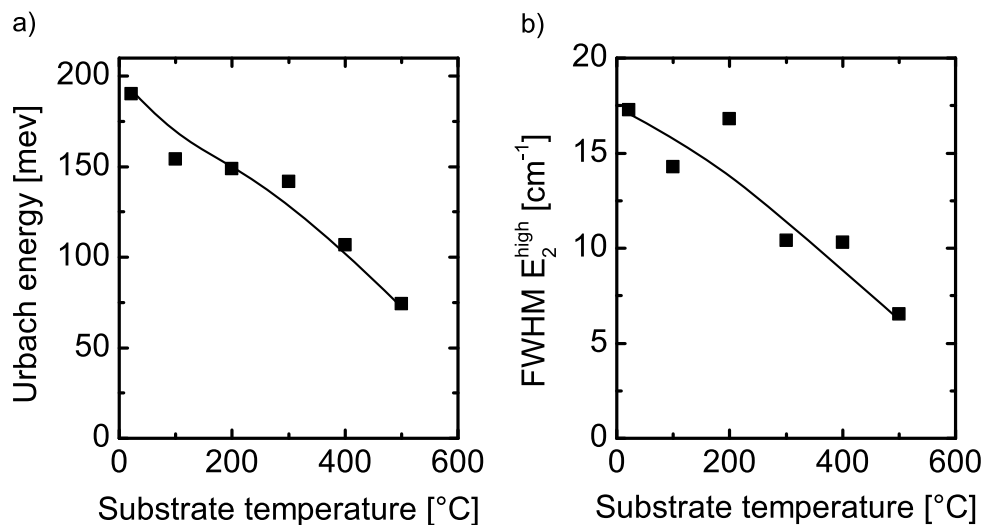


Figure 3.6: a) Urbach energy and b) FWHM of the Raman E_2^{high} mode as function of the substrate temperature during deposition. The FWHM was determined by a fit with a Lorentzian. The lines included are guides to the eye.

3.1 Influence of the substrate temperature during deposition

and discussed extensively during the past decades and will not be discussed here in detail [37, 113–115]. Instead, the focus within this work regarding the optical properties will be on the analysis of sub-band gap absorption below the fundamental absorption edge. When ZnO:Al is employed as transparent conducting oxide, occurrence and severity of this sub-band gap absorption can have a major influence on performance of optoelectronic devices [116].

From the fitting model described in section chapter 2, section 2.1.5, the exponential absorption tail width can be extracted and is illustrated in figure 3.6 a) for ZnO:Al layers as function of the substrate temperature during deposition. All samples, deposited at room temperature, possess parasitic absorption close to the band gap with Urbach energies above 180 meV. . An increase in substrate temperature results in a decreased tail width. A comparable behaviour has been published earlier [117].

Figure 3.6 b) shows the corresponding full width at half maximum (FWHM) of the Raman E_2^{high} resonance. The shape of the E_2^{high} mode provides information about the crystallinity of the material. Increased crystallinity leads to narrowing of the resonance. The width of the E_2^{high} mode has been determined by a fit with a Lorentzian and plotted against the substrate temperature. As the temperature increases the linewidth narrows, indicating an improvement of crystallinity in the sense that the areas of coherent Raman scattering are

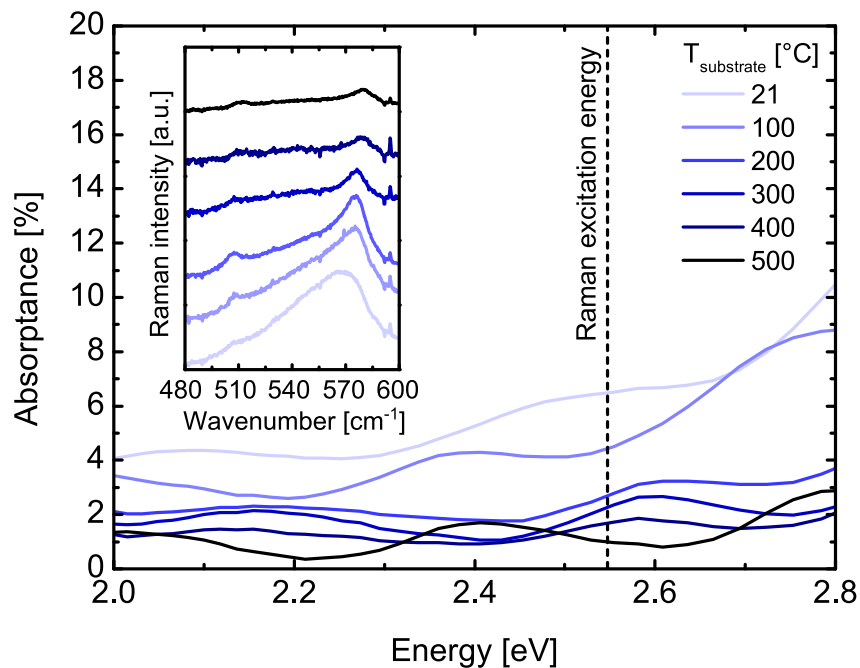


Figure 3.7: Absorbance of the ZnO:Al layers of temperature series in their as deposited state. For better comparison, the corresponding Raman spectra in vicinity of the 574 cm^{-1} resonance are given as an inset. The full spectra have been shown in figure 3.4.

3 Change of physical properties of ZnO:Al thin films after thermal treatments

enlarged. These areas are not necessarily comparable with the coherent scattering areas determined by X-ray diffraction spectroscopy (XRD). A comparison of the development of Urbach energy and the corresponding E_2^{high} FWHM with increasing substrate temperature suggests a strong correlation between the energetic width of sub-band gap absorption and structural defects within the sample that influence the Raman lineshape.

Correlation between sub-band gap optical absorption and resonant enhancement of the Raman mode at 574 cm^{-1}

For all Raman spectroscopy measurements a laser source with 488 nm, hence, 2.54 eV has been employed. Figure 3.7 shows the absorbance of the temperature series in the spectral range of the Raman laser excitation energy. Additionally, the Raman intensity around 574 cm^{-1} is given as an inset. As already mentioned before, the most plausible cause for the Raman resonance at 574 cm^{-1} is the resonant enhancement of the intrinsic longitudinal optical A_1 mode. As visible in the inset of figure 3.7, the intensity of that specific mode decreases systematically for increasing deposition temperature. At the same time, the absorbance of the ZnO:Al layers at the Raman excitation wavelength decreases. Therefore, it can be assumed that these tail states causing parasitic absorption in the spectral range of the laser excitation source are as well responsible for an amplification of the $A_1(\text{LO})$ Raman mode.

This assumption of the correlation between absorption behaviour and Raman response is further supported by the sample series in the following sections.

3.1.2 Influence of thermal treatments on the structure

The following subsection describes the influence of the application of post-deposition thermal treatments with and without protective capping layer on the structural and electrical properties as well as the impact on the absorption tail below the fundamental absorption edge. To recapitulate, the below named 'cap annealing' denotes an annealing treatment for 24 hours at 650 °C where the zinc oxide is protected by a 50 nm thick amorphous silicon layer deposited by chemical vapour deposition. The process 'degradation' represents an annealing step of the bare zinc oxide at 550 °C for 24 hours. Both treatments have been performed under atmospheric pressure and nitrogen flow.

Part I - X-ray diffraction

Figure 3.8 shows the XRD spectra of the temperature series between 30° and 75° after degradation and cap annealing, respectively, in comparison with the spectra in the as deposited state. After application of either thermal treatment, the ZnO:Al films still possess a c-axis texture with a dominant (002) reflex. Its position and FWHM as function of sub-

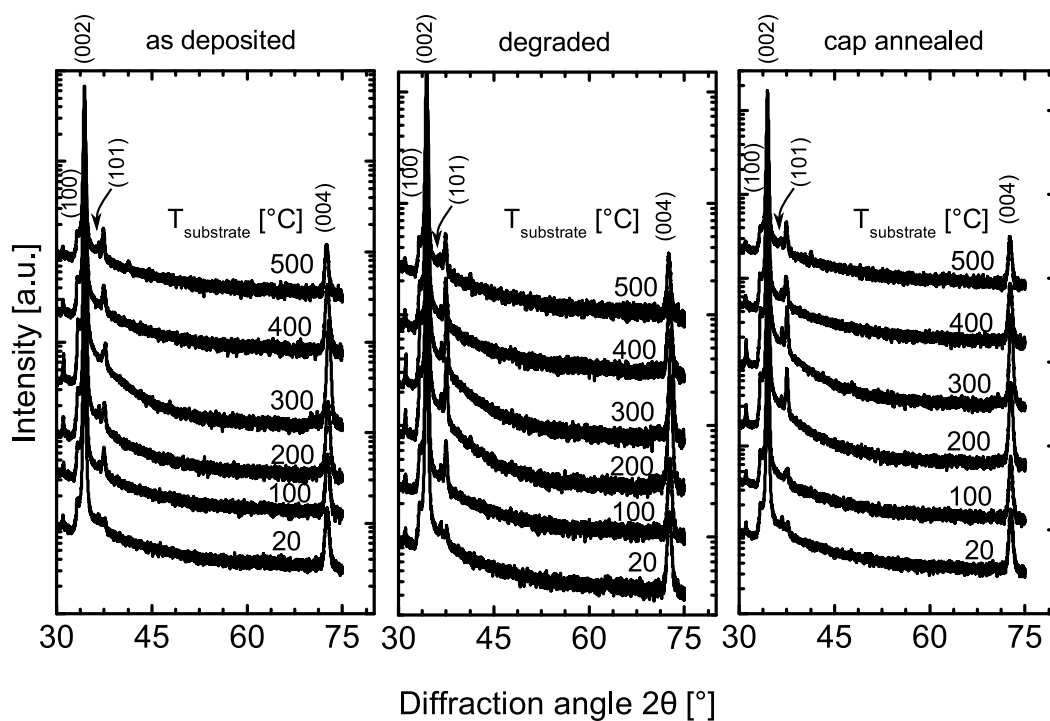


Figure 3.8: X-ray diffraction spectra between 30° and 75° for samples deposited between room temperature and 500 °C in as deposited state, after degradation and cap annealing, respectively; All spectra are normalised to their respective layer thickness and vertically shifted for clarity.

3 Change of physical properties of ZnO:Al thin films after thermal treatments

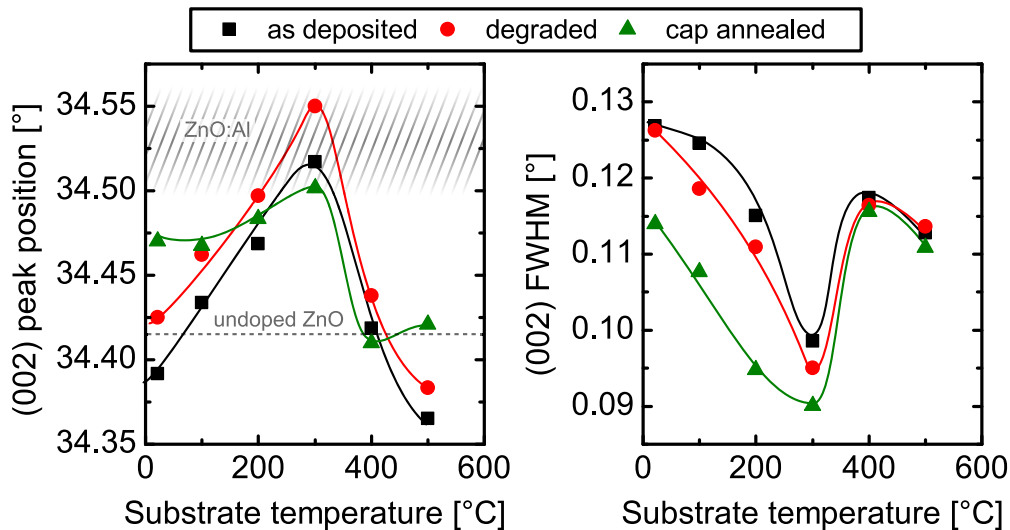


Figure 3.9: Comparison of peak position and FWHM of the (002) reflex as function of substrate temperature of as deposited state and after thermal treatment; The included lines are guides to the eye. The shaded area represents an angular region of a relaxed lattice of Al-doped ZnO. The dashed line on the other hand shows the reference value for undoped ZnO.

strate temperature during deposition after cap annealing and degradation, respectively, are depicted in figure 3.9.

The degradation treatment, the annealing of the bare ZnO:Al layer, shifts the (002) peak position systematically to larger angles, indicating a shortening of the c-axis. Assuming that for a strain-free lattice of sputtered ZnO:Al with a target doping concentration of 1 %_{wt} Al₂O₃ the (002) reflex is located slightly above 34.5°, this shift to higher angles, with respect to the as deposited states, indicates a partial relaxation of compressive strain, independent of the substrate temperature during growth. Apparently, the layers do not relax completely since an influence of the deposition temperature is still given and the reflex positions still deviate strongly from the one of the sample already deposited at 500 °C.

Change of the lattice after a thermal treatment at 550 °C is most probably related to annealing of structural defects that are growth condition based or the incorporation of species of the annealing atmosphere. Eligible specimens here are mainly nitrogen, residual oxygen, and carbon- and hydrogen compounds, since the treatment oven was not evacuated and operated only under nitrogen flow.

The change of the (002) position in case of cap annealing is inconclusive. For low substrate temperatures during growth, the (002) position shifts to a larger angle between 34.47° and 34.50°, nearly independent of the as deposited state. Deposition temperatures above 300 °C seem to cause another saturation level at a smaller angle compared to the low deposition temperatures. This is very likely related to the change in morphology of the layers as observable using SEM micrographs of the surface (fig. 3.3). The deviating behaviour of cap annealed ZnO:Al regarding the degraded layers can either be caused by the 100 °C higher treatment temperature or, less likely, an influence of the protective capping layer itself.

3.1 Influence of the substrate temperature during deposition

As it can be seen on the right side of figure 3.9, the width of the (002) reflex decreases for both annealing treatments for deposition temperatures below 300 °C. Above $T_S = 300$ °C thermal treatments in the temperature range used here do not have a significant influence on the (002) reflex' width. While for low deposition temperatures thermal treatments expand the size of coherent scattering areas slightly, hence, improve the crystallinity of the samples, no change in 'grain size' is expected for substrate temperatures above 300 °C.

This is also evident in SEM images of the surface morphology, which can be seen in figure 3.10. It is important to note, that the plasma etching procedure after cap annealing, in order to remove the protective a-Si layer, has no influence on the surface morphology. The degradation process, however, where bare ZnO:Al is exposed to the annealing atmosphere, apparently leads to a planarisation of the surface. Furthermore, it has to be mentioned that in most cases it was not possible to obtain a clear image of cap annealed samples, most likely due to a less conductive surface layer. Apparently, the cap annealing procedure modifies the surface that either a not sufficiently conductive layer remains on the sample

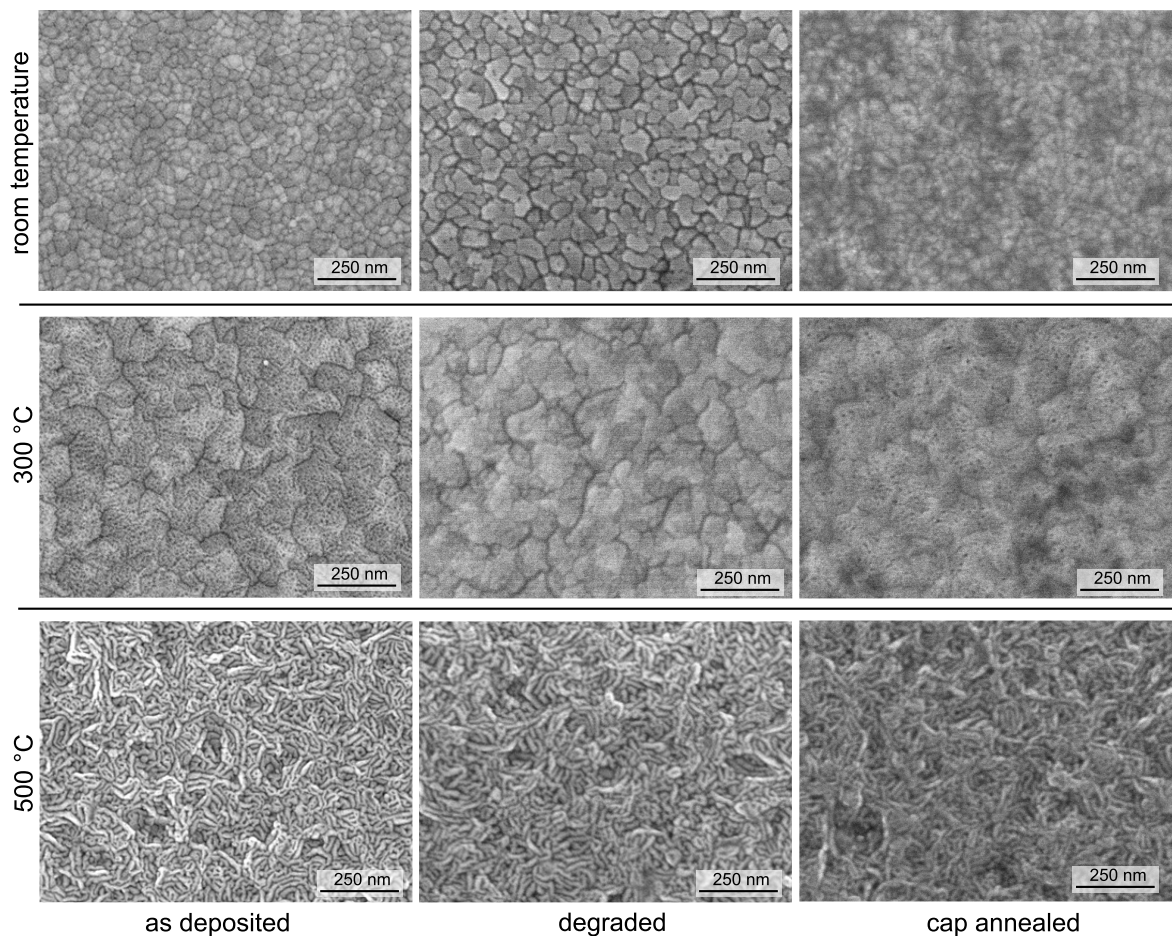


Figure 3.10: Surface SEM micrographs of ZnO:Al layer deposited at room temperature, 300 °C and 500 °C in as deposited state and after thermal treatment without cap (degraded) and with capping layer (cap annealed)

3 Change of physical properties of ZnO:Al thin films after thermal treatments

after cap removal or the cap annealing itself alters the surface layer in so far that a very thin surface ZnO:Al layer is nearly not conductive.

This effect can also be observed when cap annealed ZnO:Al is applied as front contact in a-Si/ μ c-Si tandem solar cells. A short dip of the layer in hydrochloric acid (HCl) is necessary to achieve a good performance of the cell. Without that dip the parameters of the cells are indicating a bad electrical contact between the ZnO:Al front electrode and the absorber of the solar cell [118].

A possible residual layer after cap removal might be SiO₂ created during cap annealing at the interface between ZnO:Al and the a-Si capping layer [119]. However, during experiments it could be shown that the employed plasma assisted etch step, in order to remove a-Si, etches SiO₂ as well with sufficiently high rate. Therefore, it seems unlikely that residual SiO₂ remains on the surface after cap annealing and cap removal. A further reason would be the creation of a Zn-rich layer due to oxygen depletion. This issue will be discussed in section 4.

Part II - Raman spectroscopy

Structural changes due to annealing can be also observed with Raman spectroscopy. Application of either annealing step changes the shape of Raman spectra significantly.

As it can be seen in figure 3.11 and figure 3.14 b), the E_2^{high} mode becomes sharper for both

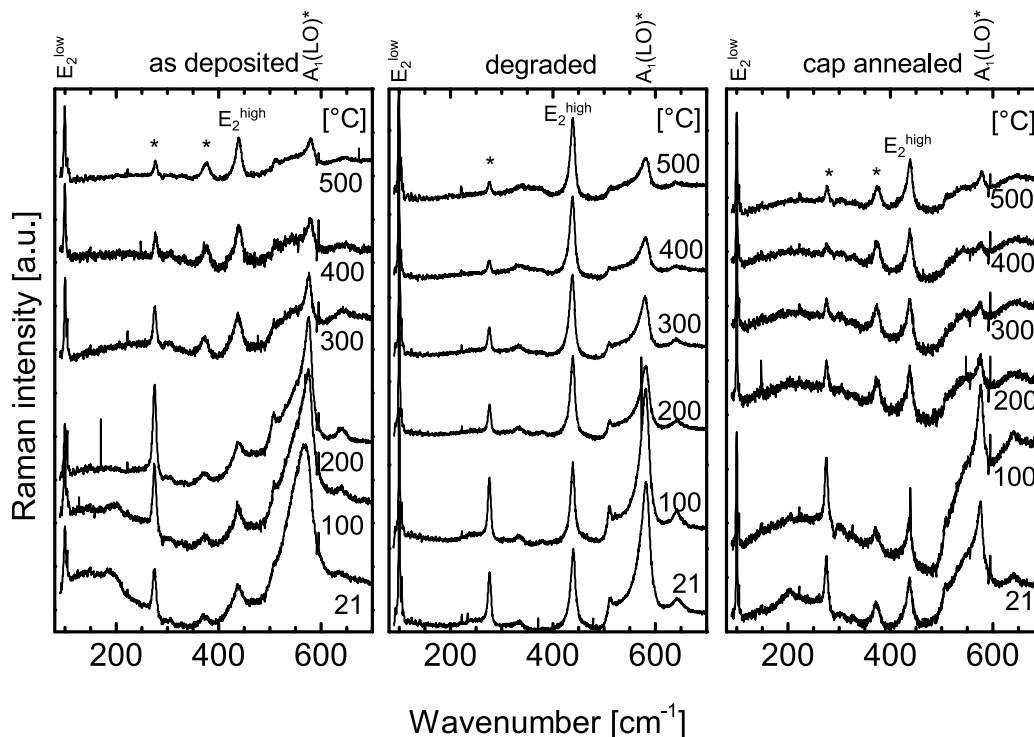


Figure 3.11: Raman spectra of the ZnO:Al thin films in as deposited state and after annealing; Substrate temperature of the individual samples are stated at the respective spectrum; All spectra are normalized to the E_2^{high} mode.

3.1 Influence of the substrate temperature during deposition

treatments which supports the concept of improved crystallinity. However, a comparison between the untreated ZnO:Al deposited at 500 °C with those deposited at lower temperatures but annealed at 550 °C shows again that both conditions result in very different structural properties.

Modes at 275 and 574 cm⁻¹

In accordance with the samples in their as deposited states the intensity of the resonance at 275 cm⁻¹ decreases systematically with increasing substrate temperature, also after application of either thermal treatments, with and without capping layer.

Interestingly, the intensity of the 574 cm⁻¹ resonance follows that behaviour. The correlation between both modes, in connection with the absorption behaviour of the respective samples will be discussed at the end of this subsection.

Mode at 378 cm⁻¹

The intensity of AM at 378 cm⁻¹ increases with raising deposition temperature for the as deposited state of the samples but vanishes almost completely if the samples have been degraded. Cap annealing, however, seems to increase its intensity even further reaching almost the intensity of the E₂^{high} mode.

For the as deposited samples, a relation to the intrinsic A₁(TO) could not be excluded. However, since no recrystallisation could be observed regarding the XRD results, the vanishing of the mode after degradation without major changes in crystal structure questions the assignment of this resonance to the intrinsic A₁(TO) mode.

3.1.3 Change of electronic transport and sub-band gap absorption after thermal treatments

Although no recrystallisation could be observed after annealing either with or without cap, the influence on the electrical properties are tremendous but expected as already explained in section 2.2.1.2.

As it can be seen in figure 3.12, all samples possess a strongly reduced electron mobility and concentration after thermal degradation with respect to the as deposited state. The carrier concentration drops by more than an order of magnitude and the mobility falls down to values of around 4 cm²/Vs. Looking at the resistivity of the samples, only weak dependence on the as deposited state and, therefore, the deposition temperature can be observed. Samples exhibiting a lower resistivity in the as deposited state possess a lower resistivity after thermal degradation, as well.

In contrast to the thermal degradation step, thermal annealing under a protective amorphous silicon capping layer yields electrically improved ZnO:Al films compared to the as deposited state. While the carrier concentration raises slightly with less than 10 % for samples deposited below 400 °C and approximately just doubles for layers above T_S = 400 °C, the

3 Change of physical properties of ZnO:Al thin films after thermal treatments

mobility increases significantly for all samples and reaches values up to $65 \text{ cm}^2/\text{Vs}$. Here, the dependence of electrical properties on the temperature during deposition is clearly reduced. The largest improvements were achieved for samples deposited at 400°C and 500°C with a decrease in resistivity from $9.9 \times 10^{-4} \text{ }\Omega\text{cm}$ to $3.0 \times 10^{-4} \text{ }\Omega\text{cm}$ and from $30 \times 10^{-4} \text{ }\Omega\text{cm}$ to $4.6 \times 10^{-4} \text{ }\Omega\text{cm}$, respectively.

In their as deposited state a clear correlation between enhanced structural quality, like larger grains and better crystallinity, and improved electrical properties was observable. However, especially in case of the degraded ZnO:Al films it becomes apparent that improved crystallinity does not necessarily lead to an enhanced mobility or carrier concentration.

Since the electrical properties could be significantly improved using cap annealing this treatment was applied on already degraded samples in order to examine a possible reversibility of the latter process. This combined treatment is called *2 step annealing* and presents an appropriate way to tailor the electrical properties of ZnO:Al as it was already shown by Wimmer *et al.* [78].

Generally, the dependence on the as deposited state for the 2 step annealed samples is very similar compared to the cap annealed films. The previously applied degradation step causes a generally decreased carrier concentration compared to the as deposited layers and those treated with cap annealing only. Additionally, the carrier mobility does not reach those high values achievable for cap annealing alone, but is still enhanced compared to the as deposited state.

Therefore, it can be concluded that there are at least two mechanisms causing the strong degradation of electrical properties where one of it can be reversed by application of cap annealing.

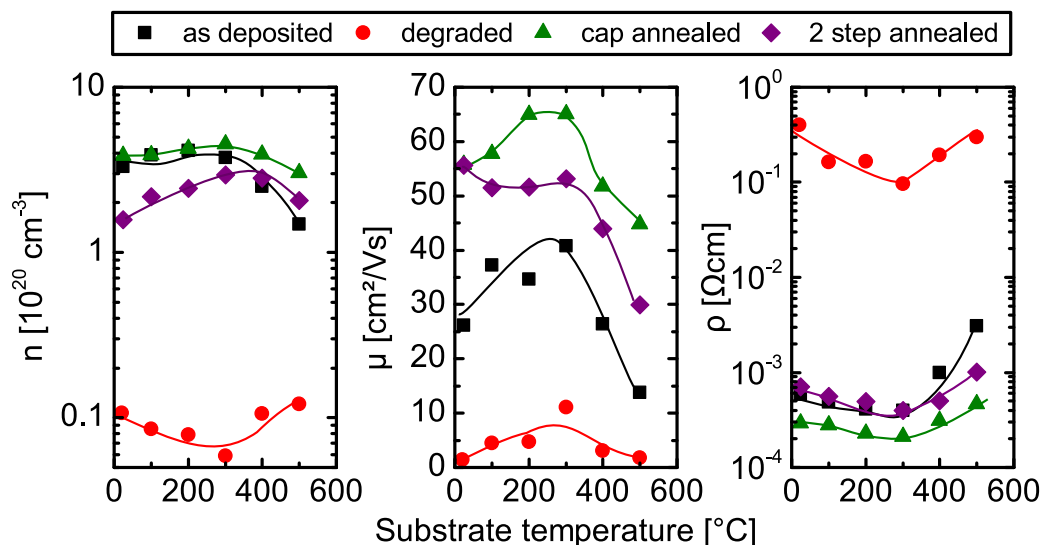


Figure 3.12: Carrier concentration, carrier mobility and resistivity as function of substrate temperature in the as deposited state and after thermal treatment; The included lines are guides to the eye.

3.1 Influence of the substrate temperature during deposition

Sub-band gap absorption

The changes of electrical properties are again reflected in the optical properties. Figure 3.13 demonstrate the alterations of absorptance in the vicinity of the band gap as well as in the infrared region for all thermally treated and untreated samples. All three groups of samples, as deposited in black, degraded in red and cap annealed in green, show clearly different absorption behaviour.

The strong degradation of electrical properties after annealing without capping layer is well reflected in the vanishing free carrier absorption (FCA) between 0.5 and 1 eV. Cap annealing results mainly in comparable carrier concentrations in respect to the as deposited state which can also be concluded from behavior of the FCA.

The strong decrease of the carrier concentration in case of the degraded films leads to a shift of the band gap to lower energies, due to the Burstein-Moss shift.

The slope at the fundamental absorption edge is strongly influenced by the application of thermal treatments, with and without cap. The width of the absorption tail is again determined using the model of eq. 2.42 and plotted against the substrate temperature for all

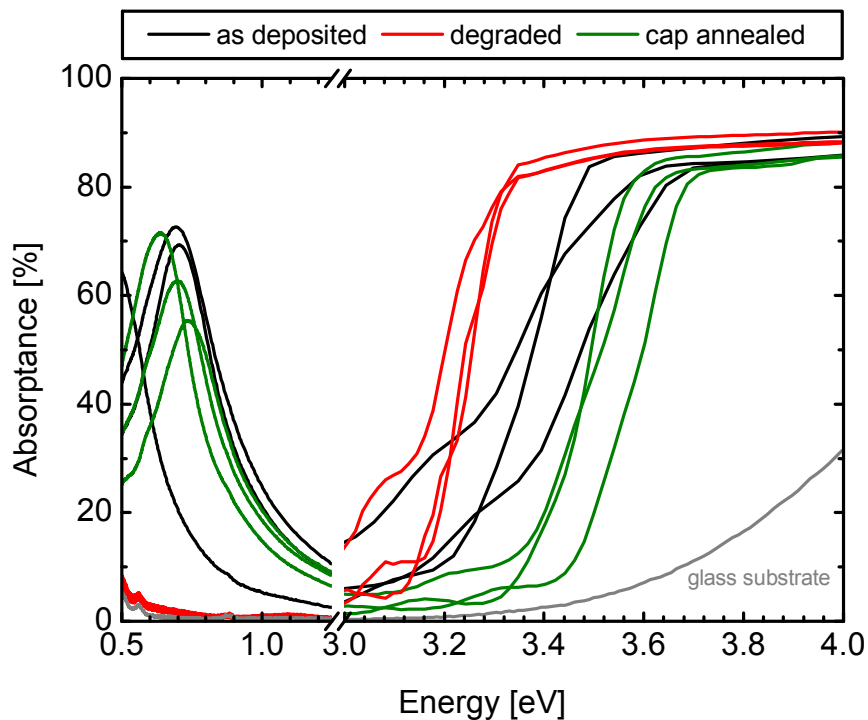


Figure 3.13: Absorptance of ZnO:Al films on glass of the substrate temperature series as function of photon energy; The film thickness of the layers is (668 ± 28) nm. The black lines represent the samples in their as deposited state. Green lines describe the absorptance of the samples after application of cap annealing. The absorptance of the bare glass substrate is shown as a grey line. For better resolution of the sub-band gap area close to the fundamental absorption edge and the free carrier absorption in the infrared region, the energy scale is interrupted between 1.25 eV and 3 eV.

3 Change of physical properties of ZnO:Al thin films after thermal treatments

treated and untreated states in figure 3.14 a).

Having this quantitative measure it is obvious that the supply of thermal energy, either already during growth via elevated substrate temperature or by application of post-deposition thermal treatments, significantly suppresses the development of absorption tails at the band gap.

Interestingly, although carried out at 100 °C higher plateau temperature, the Urbach energy E_U of cap annealed ZnO:Al layers are, independent of their initial state, higher than the E_U 's of the degraded films.

Generally it can be said that an influence of the thermal deposition conditions after annealing is just present for ZnO:Al films deposited at low temperature. For samples grown at 300 °C or more, some kind of lower boundary of the tail width exists.

It has to be noted that small Urbach energies in the range of the values determined for the thermally treated samples have to be regarded with special care respective the separation of Urbach tail and influence of the absorption edge broadening determined by the error function in eq. 2.42. This topic will be discussed in section 3.5 about multi-step annealing and in appendix section B.

Figure 3.14 b) shows the fitted linewidths of the E_2^{high} Raman mode.

Application of both treatments, either degradation or cap annealing, strongly decreases the FWHM. Furthermore, no connection to their as deposited state is observable anymore. Generally, cap annealed samples possess a wider linewidth as the degraded ZnO:Al films, which is conclusive to the findings of the Urbach energy. The conclusion, drawn for the as deposited ZnO:Al films that the width of the absorption tail is closely connected to the Raman influencing crystal quality, can, therefore, be confirmed.

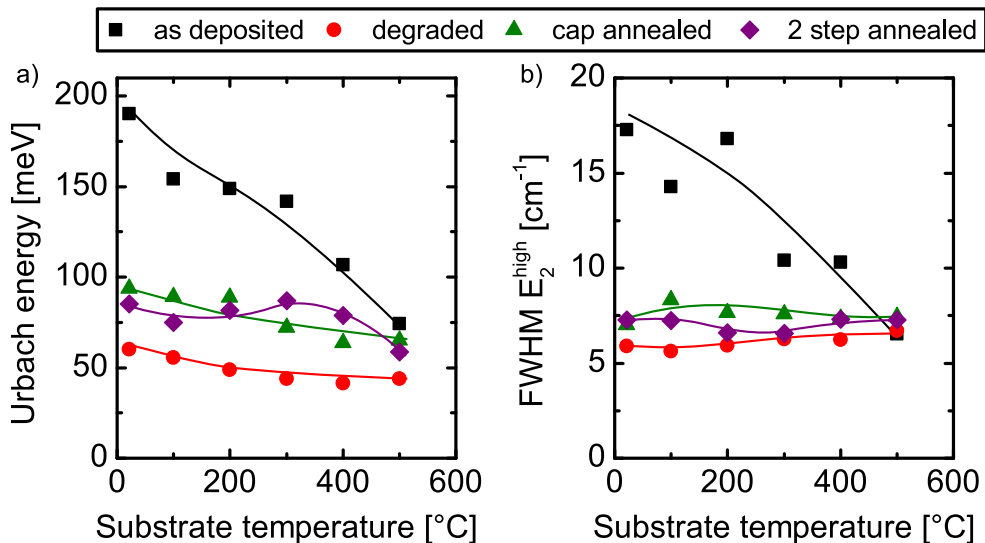


Figure 3.14: a) Urbach energy and b) FWHM of the Raman E_2^{high} mode as function of the substrate temperature during deposition in the as deposited state and after thermal treatment. The included lines are guides to the eye.

3.1 Influence of the substrate temperature during deposition

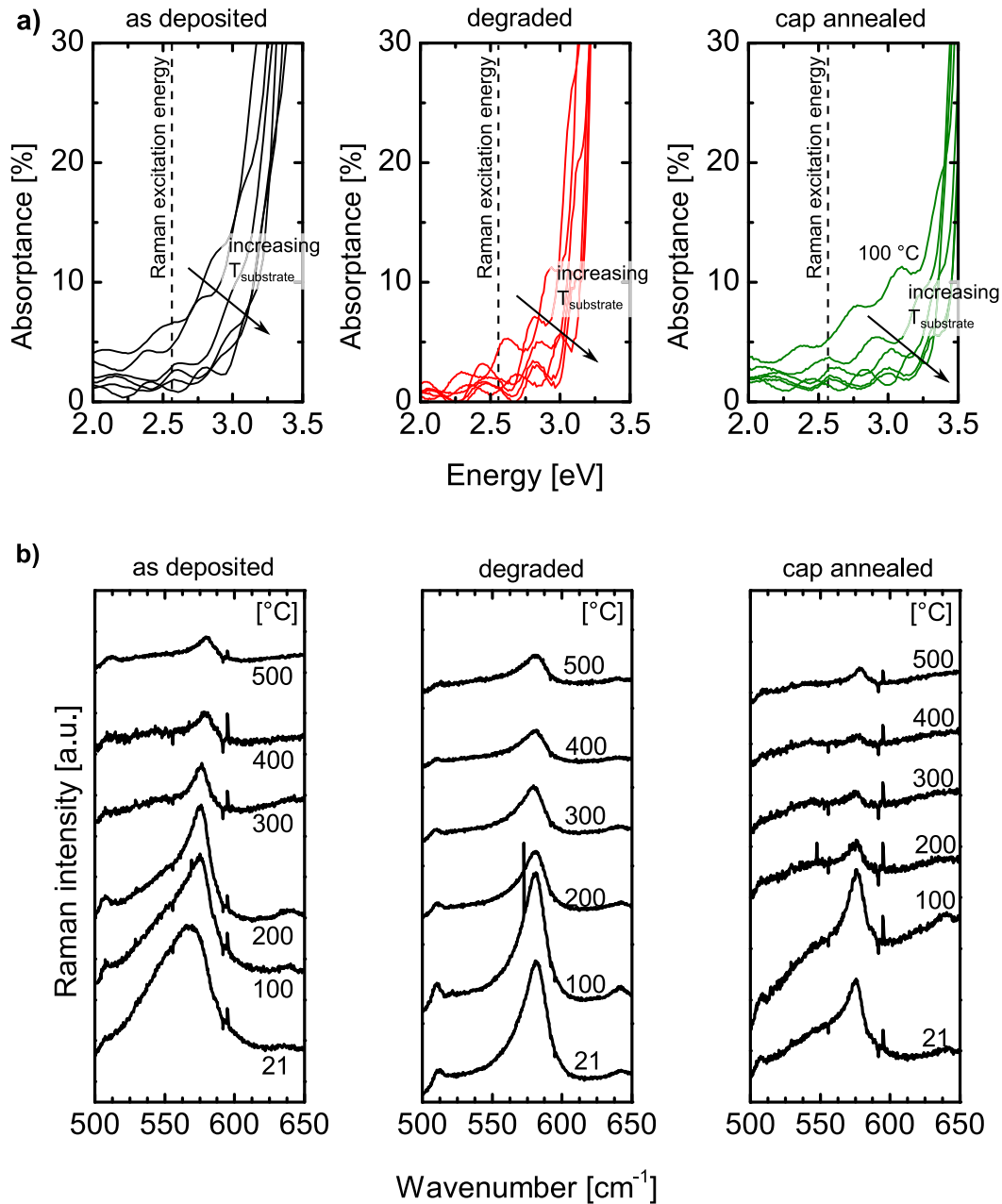


Figure 3.15: a) Absorbance in the spectral range of the Raman excitation energy of ZnO:Al layer of the temperature series in their as deposited state and after application of degradation and cap annealing, respectively. Part b) shows the corresponding Raman spectra in the range of $500 \text{ cm}^{-1} - 650 \text{ cm}^{-1}$. The full spectra can be seen in figure 3.11.

3 Change of physical properties of ZnO:Al thin films after thermal treatments

Correlation between sub-band gap optical absorption and resonant enhancement of the Raman mode at 574 cm⁻¹

Increase of substrate temperature during deposition causes a decrease in Urbach energy and, hence, a decreasing absorption at 2.54 eV, the employed Raman excitation energy. This is not only the case for the as deposited state of the samples. Both treated sample groups, degraded and cap annealed, exhibit the same tendency, which is shown in figure 3.15 a). For a better comparison with the behaviour of the corresponding Raman mode at 574 cm⁻¹, the relevant parts of the Raman spectra (fig. 3.11) have been extracted and plotted in fig. 3.15 b).

Comparing the absorbance around 2.54 eV with the intensity of the Raman 574 cm⁻¹, a direct correlation between decreasing absorption in the spectral range of the Raman excitation and attenuation of the resonant enhancement of the A₁(LO) Raman mode at 574 cm⁻¹ can be observed not just for the as deposited samples but after annealing as well.

3.1.4 Discussion regarding microscopical changes during annealing

As shown in the previous section, thermal post-deposition treatments of bare ZnO:Al films at high temperatures result in significant deterioration of electrical properties, but if protected by a silicon cover layer in considerable improvement.

These effects have been already reported e.g. by Lee *et al.* [65], Ruske *et al.* [66], Wimmer *et al.* [79] and Neubert *et al.* [116]. However, the main mechanisms which cause such behaviour remained still unclear.

Discussions of changes of electrical transport should happen in context of their dependence on scattering mechanisms and carrier concentration. Since the electrical transport in semi-conductors is rather complex and involves a wide variety of scattering sites, such as phonons (PS), ionised (IIS) and neutral impurities and grain boundaries, a very good description of the experiment would just be possible with an equally complex theory.

Here, a simplified model as described in section 2.1.4 is used instead, considering only IIS and PS. This is insofar acceptable, since for ZnO:Al, at high carrier concentrations, they are assumed to be the dominating scattering sites [20, 26]. For low carrier concentrations, however, the influence of grain boundaries (GB) increase significantly. Its contribution is hard to estimate as both, tunneling and thermionic emission over GB's should be considered.

The ZnO:Al films studied here in their as deposited, cap annealed and 2 step annealed state possess carrier concentrations far above the Mott criterion (see section 2.1.3). Hence, they are considered degenerated and the model by Look is suitable to analyse the change in their donor and acceptor concentrations. Degraded samples, due to their critically low carrier density, are excluded from the analysis using this model considering just IIS and PS. From the theory alone, however, it seems reasonable to assume a high compensation ratio of the samples, but exact values are almost impossible to derive due to the strong influence of small experimental uncertainties in this range of mobilities and due to the unknown contribution of grain boundaries.

As introduced in section 2.1.4, two different approaches for determination of the required effective mass m^* are considered. Both result in different contributions of PS and IIS to the maximum obtainable mobility μ_{\max} at a certain carrier concentration.

The results of μ_{\max} , according to Pisarkiewicz's and Look's m^* assumptions, can be seen in figure 3.16. Additionally to μ_{\max} the individual contributions for IIS and PS are illustrated for the Pisarkiewicz approach. The lower effective mass used by Pisarkiewicz leads to a higher mobility limit compared to the approach of Look, both differing by 15 cm²/Vs at a maximum in the considered range of n .

Next to the theoretical mobility limits figure 3.16 a) and b) show the experimentally determined mobility μ as function of carrier concentration for all ZnO:Al films of the temperature series in their as deposited state and after degradation, cap annealing and 2 step annealing. Given the variation of used parameters in literature, the highest obtained mobility corresponds well to the predictions.

3 Change of physical properties of ZnO:Al thin films after thermal treatments

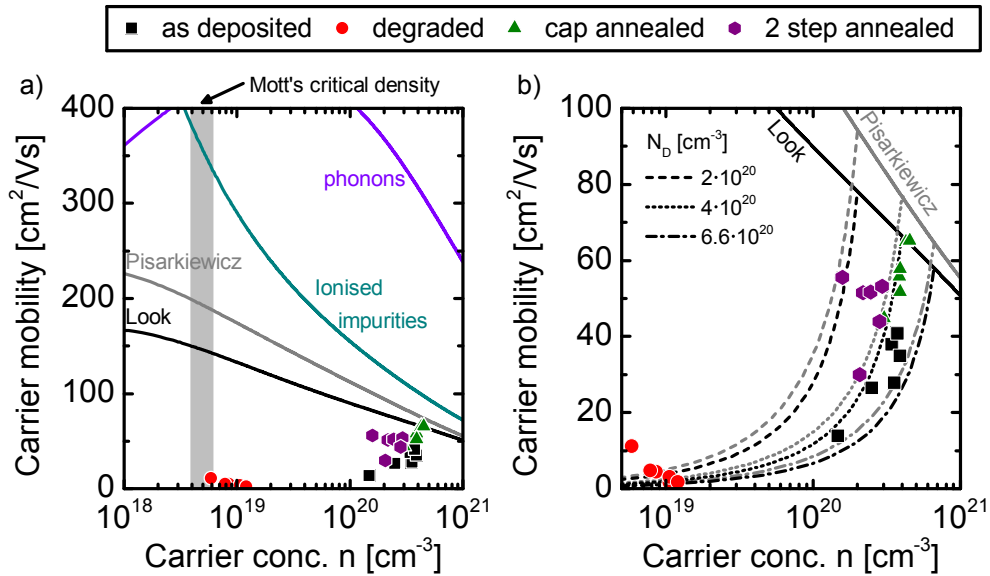


Figure 3.16: a) Mobility limits according to Look and Pisarkiewicz; The individual components for ionised impurity and phonon scattering are given for the effective mass approach of Pisarkiewicz; b) Additionally to the mobility limits according to Look and Pisarkiewicz the respective declines in mobility for increasing acceptor concentration at different fixed donor concentrations N_D are given. For further information, see text.

Assuming that the (de-)activation of donors and creation of acceptors are the driving mechanisms for changes in carrier concentration and mobility, it is interesting to calculate μ as function of n for a fixed donor but increasing acceptor concentration. The dashed and dotted lines in figure 3.16 b) represent the results of this calculation for both effective mass approaches with fixed donor concentrations of 2, 4 and 6.6 · 10²⁰ cm⁻³. The latter was chosen since it corresponds to the Al concentration in the employed target and would equal a doping efficiency of 100 %.

Already this simple assumption of a μ -dependence on only the compensation of donors describes the experimentally obtained data already pretty well.

In a next step, the donor N_D and acceptor concentrations N_A have been calculated by fitting n and μ using the scattering model of D. Look but the effective mass approach of Pisarkiewicz. At this point it should be noted again that only singly charged donors and doubly charged acceptors have been considered, taking into account aluminum donors (Al_{Zn}) and zinc vacancies (V_{Zn}) as dominant ionised defects. The resulting values have been plotted in figure 3.17 for the as deposited, cap annealed and 2 step annealed samples of the temperature series.

Here, three groups of samples, situated in different regions, evolve, mainly dependant on the experienced treatment. Within these groups, the change in donor and acceptor concentration is clearly related to the applied substrate temperature T_S during deposition.

In case of the as deposited samples, an increase of T_S up to 300 °C yields both, lower

3.1 Influence of the substrate temperature during deposition

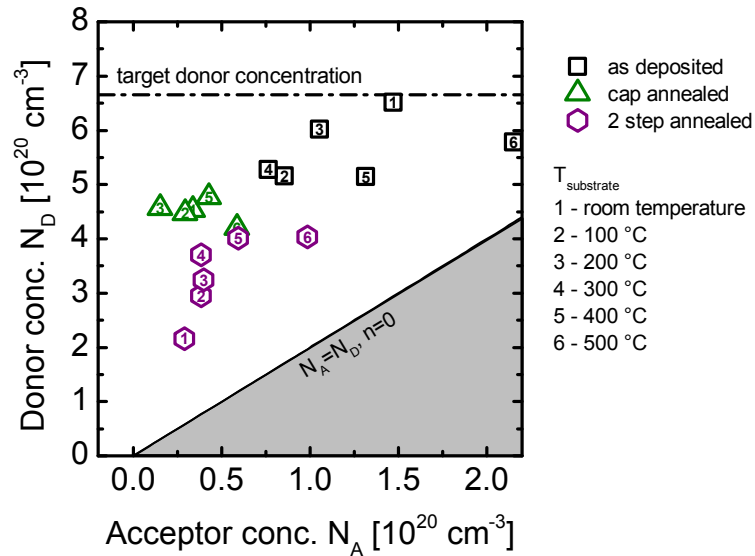


Figure 3.17: Donor and acceptor concentration for the as deposited and annealed ZnO:Al layers of the temperature series according to the scattering model of D. Look using the effective mass approach of Pisarkiewicz

N_D and lower N_A , explaining the observed increase in mobility in this temperature regime. A further raise of T_S results in significant increase of N_A which might be related to the observed changes in grain size and shape at high T_S .

Cap annealed ZnO:Al films possess in general a significantly reduced acceptor concentration but forfeit in donor concentration, as well. Both effects, but especially the reduction of double charged acceptors, result in the significantly enhanced mobility by annealing under an a-Si cap due to strongly reduced IIS. The disproportionate decrease in acceptor concentration and, hence, a reduced compensation ratio explains the slight increase in carrier concentration after cap annealing.

The influence of the substrate temperature is considerably reduced. However, while for up to 300 °C the reduction in acceptor concentration becomes larger, the trend reverses for higher substrate temperatures.

Application of cap annealing on already degraded ZnO:Al (2 step annealing) leads to a tendentially higher acceptor and lower donor concentration with respect to cap annealing of the as deposited samples. It seems that the prior applied degradation partially induces states that irreversibly deactivate donors or trap electrons. However, it demonstrates as well, that a major part of the degradation mechanism is reversible.

The generally different behaviour of the 2 step annealed ZnO:Al layers deposited above 300 °C is most likely again owed to their very different structure.

Even if degraded layers cannot be considered using the simple compensation model of D. Look due to their critically low carrier concentration, conclusions can be still drawn

3 Change of physical properties of ZnO:Al thin films after thermal treatments

using the results of the 2 step annealing.

In the framework of dominant IIS, the strong decrease in carrier concentration after annealing without cap could be explained with the deactivation of donors and the compensation of donors by formed acceptors. Both processes would increase the concentration of neutral scattering sites (NIS) and IIS. However, the scattering probability is significantly larger for IIS and causes, therefore, a higher impact on the mobility.

A comparison of the N_A/N_D results of cap and 2 step annealed samples indicated that a degradation step irreversibly deactivates parts of the incorporated donors, not recoverable by cap annealing.

The reversible component may partly be related to the diffusion of hydrogen from the a-Si:H cap into the ZnO layer, acting as shallow donor and passivating acceptor-like defects [89]. The influence of hydrogen on the annealing process will be discussed in detail in section 3.4.

Both annealing procedures, with and without cap, occur in the same temperature regime. Therefore, it is unlikely that the very different change in electrical properties associated with these treatments is primarily temperature related. The major difference of both procedures is the presence or absence of a capping layer that shields the underlying ZnO:Al from influences of the annealing atmosphere.

Hence, it can be assumed that an exchange with the atmosphere is the main driver for the strong degradation of electron concentration and mobility during annealing without cap. Annealing atmosphere have been in all cases flowing nitrogen with a purity of 99.9999 %, however, the oven was not evacuated prior the treatment. It is, therefore, expected, that residual oxygen is still present in the atmosphere. Incorporation of nitrogen or oxygen would very likely lead to the creation of acceptors in ZnO:Al [120, 121]. In addition, Al oxidizes very easily at high temperatures and in the presence of oxygen. However, as will be shown in section 3.3 nitrogen incorporation can be excluded and does not have any influence on the annealing results.

3.1.5 Summary

Modification of the substrate temperature has a huge impact on the structural properties like grain size and surface morphology of the deposited ZnO:Al thin film. Major influencing factors are the diffusivity of adatoms, thermal mismatch between layer and substrate, atomic impinging during sputtering and doping. Thermal annealing with and without cap in nitrogen atmosphere at 550 °C and 650 °C, respectively, do not lead to any major recrystallisation but to enhanced vibrational properties.

The changes of sub-band gap absorption, described by Urbach-like tails, are primarily temperature related. It could be observed that after thermal treatment both, electrically excellent (cap annealed) and electrically deficient (degraded) ZnO:Al films, possess very narrow absorption tails. The width of the Urbach tail correlates with those structural defects influencing the Raman crystallinity.

3.1 Influence of the substrate temperature during deposition

Furthermore, it could be shown that pronounced Urbach tails can resonantly enhance LO phonon modes even if the Raman excitation energy is chosen within the band gap.

As expected, cap annealing significantly improves the electrical properties of ZnO:Al films, especially their carrier mobility. Annealing without cap deteriorates the electrical transport. The changes of electrical properties after application of thermal post-deposition treatments has been examined in the context of donor (de-)activation and compensation by acceptors. While as deposited samples are characterised by a high donor concentration and partial compensation, the latter can be significantly reduced by cap annealing. However, this is accompanied by a slight reduction of the donor concentration. The further, partly considerably decreased donor concentration of 2 step annealed ZnO:Al, comparing to only cap annealed layers, indicates that the applied degradation step is able to irreversibly deactivate parts of the incorporated donors, not recoverable by cap annealing.

The applied temperature during annealing can be excluded as main cause for changes in electrical transport since both thermal treatments, with and without cap, were carried out in the same temperature regime but yield very different, contrasting electrical properties for the treated ZnO:Al layer. Hence, an interaction with the cap material and the annealing atmosphere, respectively, is suspected.

In this context, possible candidates for influencing the donor and acceptor concentration in the material are oxygen, nitrogen or hydrogen, which are present in either annealing atmosphere or capping layer.

Considering the electrical properties, a dependence on the initial deposition conditions, i.e. the substrate temperature, remains even after high temperature treatments. This is very likely due to the different structure of the films and, hence, different annealing behaviour of the samples.

3.2 Systematic variation of oxygen addition during deposition

The supply of oxygen during film growth influences the stoichiometry and, therefore, the optoelectronic properties significantly. As already explained in the previous section, it is assumed to play a key role in thermal annealing processes [66]. In this section oxygen supply during deposition was successively increased to investigate the impact on properties of as deposited and thermally treated films and to answer the question whether a possible oxygen incorporation during annealing is comparable to incorporation already during film growth.

3.2.1 Electrical, optical and structural properties in the as deposited state

Electronic transport

Oxygen incorporation significantly influences electronic properties of ZnO:Al, as it can be seen in figure 3.18. The carrier concentration decreases exponentially with linear increase of oxygen supply during growth over three orders of magnitude within the investigated range of oxygen concentration. Up to 0.75 % oxygen/Ar the mobility decreases significantly and saturates at very low level with values below $2.5 \text{ cm}^2/\text{Vs}$. Both together cause a resistivity increase of about five orders of magnitude and a saturation at around $10^4 \text{ }\Omega\text{cm}$. This behaviour is already known and reported in literature [122–124].

Structure part I - X-ray diffraction

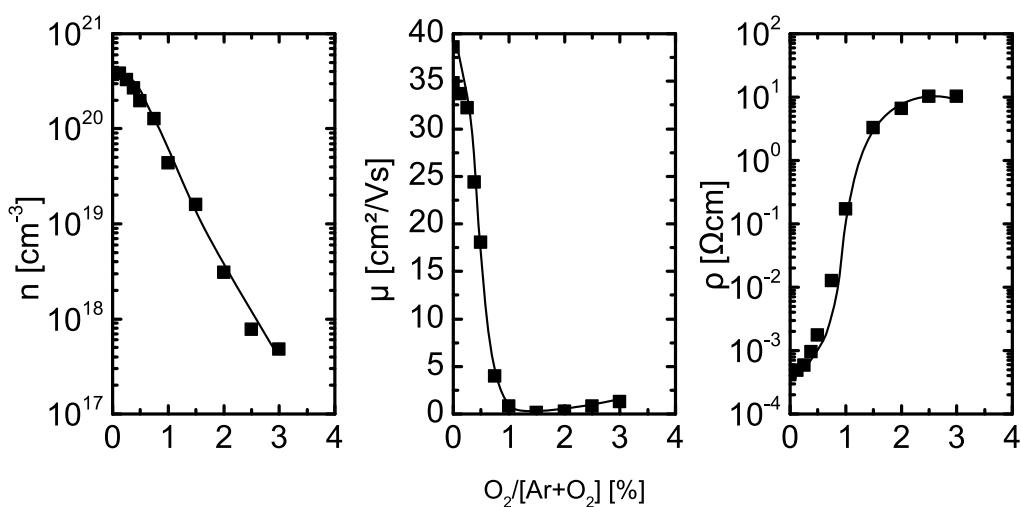


Figure 3.18: Carrier concentration, mobility and resistivity as function of oxygen to argon ratio in sputter atmosphere; The included lines are guides to the eye.

3.2 Systematic variation of oxygen addition during deposition

Like in case of the temperature series, samples of the oxygen series have been investigated regarding their structural properties using XRD, Raman spectroscopy and SEM images of the surface.

As it can be seen in figure 3.19, XRD spectra show significant changes above an oxygen concentration of 0.75 % in the sputter atmosphere, a critical concentration regarding the electrical properties, as well. While the diffraction reflex of the [100] direction at 31.1° vanishes, reflexes of the directions [102] at 47° and [103] at 62° start to evolve. However, for all samples a preferential (002) texture with grain growth along the c-axis is maintained even though the relative intensity of the [001] direction reflexes are decreased for increasing oxygen partial pressure during deposition.

This reduction of the degree of c-axis orientation is accompanied by a drop of deposition rate, as can be seen in figure 3.20 a). The initial increase of growth rate up to 1 % could be explained by a decrease of desorption of metallic Zn due to an increased supply of oxygen as reactant gas. The subsequent drop of deposition rate with even more supply of oxygen is either related to a change of adhesion of species arriving at the substrate or a change in sputter rate.

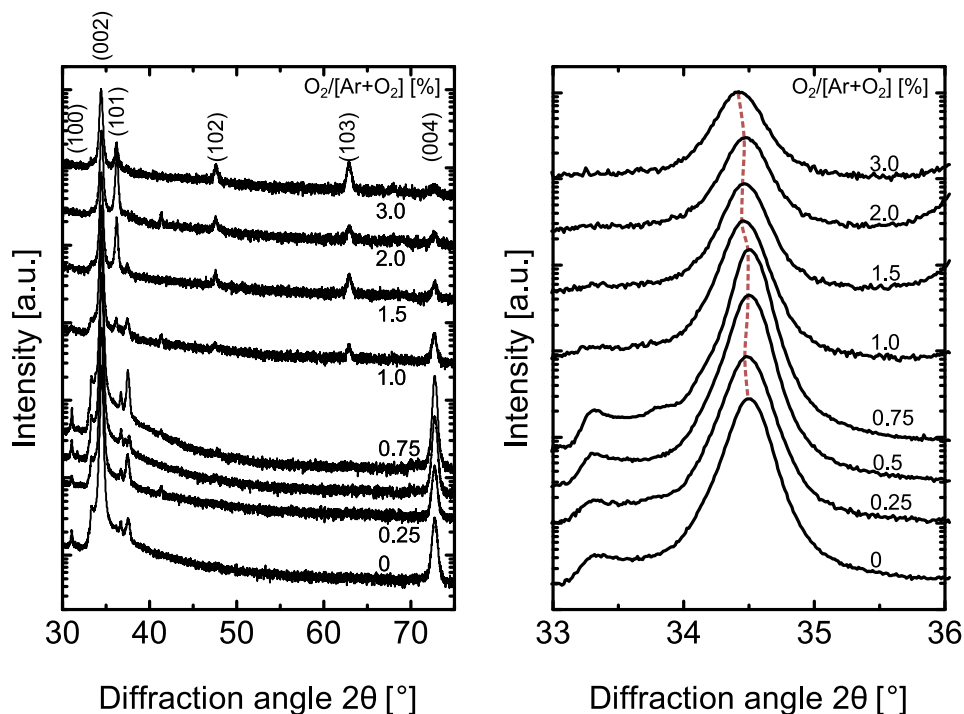


Figure 3.19: X-ray diffraction spectra between 30° and 75° and b) around the (002) reflex as function of the oxygen to argon ratio in the sputtering atmosphere. The shift in position of the (002) reflex is indicated with a red dashed line. All spectra are normalised to their respective layer thickness and vertically shifted for clarity. The individual $O_2/[Ar+O_2]$ ratio is stated at the respective spectrum.

3 Change of physical properties of ZnO:Al thin films after thermal treatments

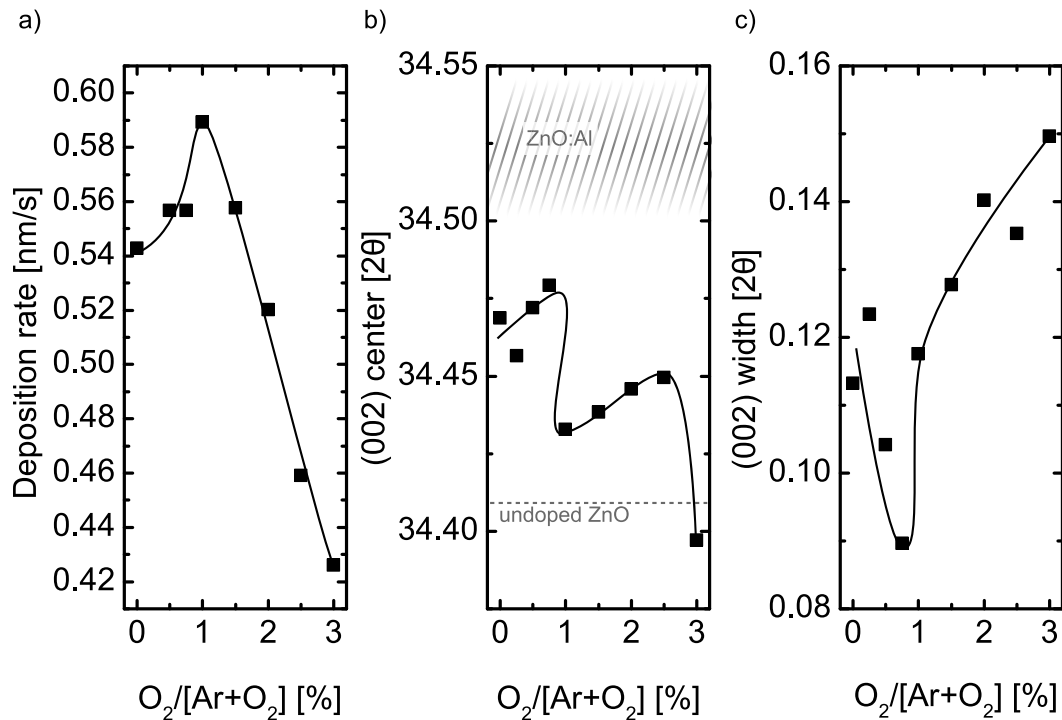


Figure 3.20: Peak position and FWHM of the (002) reflex as function of the oxygen to argon ratio in the sputtering atmosphere; The included lines are guides to the eye.

Figure 3.20 shows the center of the (002) reflex and its FWHM as function of the oxygen to argon ratio used during sputter deposition. Up to 0.75 % O_2/Ar the (002) peak position does not change significantly. However, above 0.75 %, the appearance of additional growth directions is accompanied by a considerable shift of (002) reflex position to smaller angles indicating an elongation of the c-axis. It can be assumed that, due to competing growth, the (002) grains get compressed by grains of other growth directions.

At low oxygen partial pressures ZnO:Al thin films grow sub-stoichiometrically and, therefore, less homogeneously. More crystallographic defects are constructed and the long-range order is disturbed. For this series, this is the case for samples prepared with an oxygen to argon ratio below 0.75 %. Additionally, the surface of the sample deposited with O_2/Ar of 0.75 % exhibits the most homogeneous surface morphology compared to samples deposited at lower or higher oxygen partial pressures, as it can be seen in figure 3.21. Furthermore, this critical oxygen concentration regarding structural properties can be observed not only in the reduction of the line width of the (002) peak in the XRD spectra (figure 3.20), but also of the E_2^{high} obtained with Raman spectroscopy (fig. 3.24).

3.2 Systematic variation of oxygen addition during deposition

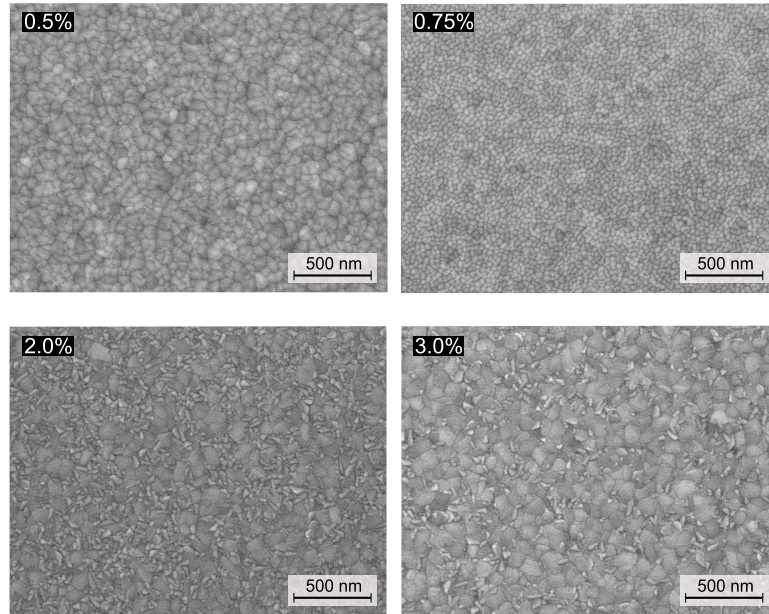


Figure 3.21: SEM surface micrographs of ZnO:Al layers with increasing O_2/Ar ratio during growth; The individual ratios are given at the respective image.

Structure, Part II - Raman spectroscopy

Figure 3.22 shows the corresponding Raman spectra of the ZnO:Al layers deposited under variable oxygen content in the sputtering gas.

Considering the E_2 modes, no remarkable change with increasing oxygen concentration takes place. However, the additional mode at 275 cm^{-1} and the longitudinal optical mode at 574 cm^{-1} possess a strong dependence on the oxygen supply during growth.

Mode at 574 cm^{-1}

The additional mode, which could be attributed to the resonantly enhanced $A_1(\text{LO})$ mode in ZnO, decreases significantly with addition of a small quantity of oxygen but generally increases again with raising oxygen concentration in the sputtering gas during deposition. A comparison with the optical absorption, as it has been done for the samples of the temperature series, will be given at the end of this subsection.

Mode at 275 cm^{-1} and 510 cm^{-1}

Regarding the AM at 275 cm^{-1} two features are remarkable. The addition of oxygen generally decreases the intensity of that mode. Considering the assignment of that resonance to interstitial zinc clusters [108], this behaviour is not unexpected since additional oxygen during film growth oxidises excess zinc and reduces, therefore, the incorporation of zinc at interstitial lattice sites.

3 Change of physical properties of ZnO:Al thin films after thermal treatments

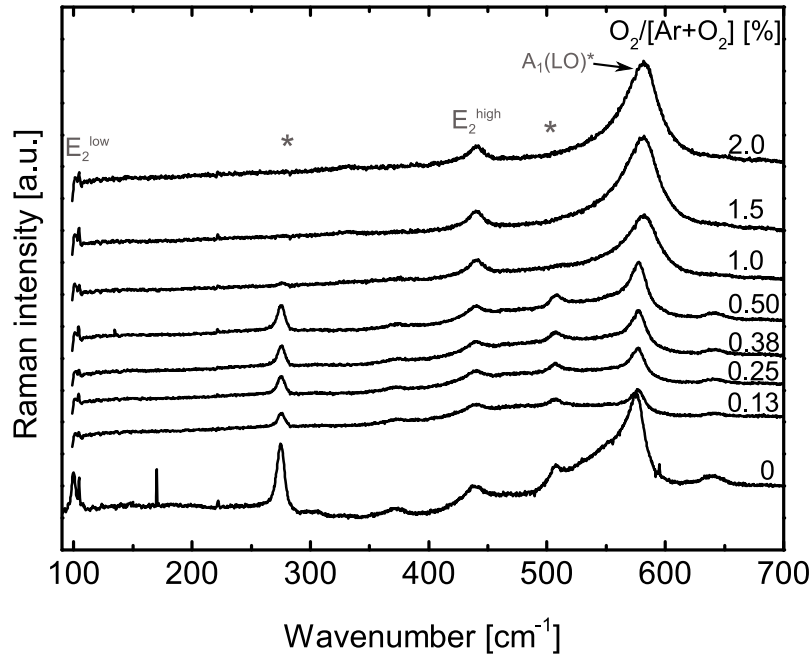


Figure 3.22: Raman spectra of ZnO:Al layers deposited with additional oxygen in the sputtering gas. The oxygen to argon ratio is given at the respective graphs. All spectra are normalised to the E_2^{high} mode and vertically shifted for clarity.

However, increase of oxygen concentration from 0.13 to 0.5 % results in a small increase of intensity while at a concentration of 1 % the resonance vanishes completely. The appearance of an AM at 510 cm^{-1} seems to be closely connected to the one at 275 cm^{-1} . As it will be shown at the end of the following subsection, which describes and discusses the influences of thermal treatments on the properties of sputtered ZnO:Al grown under additional oxygen supply, the resonant enhancement of the $A_1(\text{LO})$ Raman mode due to sub-band gap absorption can be affirmed. The absorption in the spectral range of the Raman excitation energy is affected not just by the width of the Urbach tail as proposed for the samples of the temperature series, but is influenced by absorption correlated with the appearance of the AM at 275 cm^{-1} , as well.

Sub-band gap absorption

The deposition conditions regarding the oxygen content in the sputter atmosphere influence also the position and shape of the fundamental absorption edge. The significant reduction in carrier concentration results in a shift of the band gap to lower energies according to the Burstein-Moss shift. In figure 3.23 the absorption coefficient α is given for ZnO:Al thin films with a thickness of $700 \pm 15 \text{ nm}$ deposited with different oxygen concentrations in the sputtering gas. Additionally, the absorbance A_{visible} of these layers, averaged over the

3.2 Systematic variation of oxygen addition during deposition

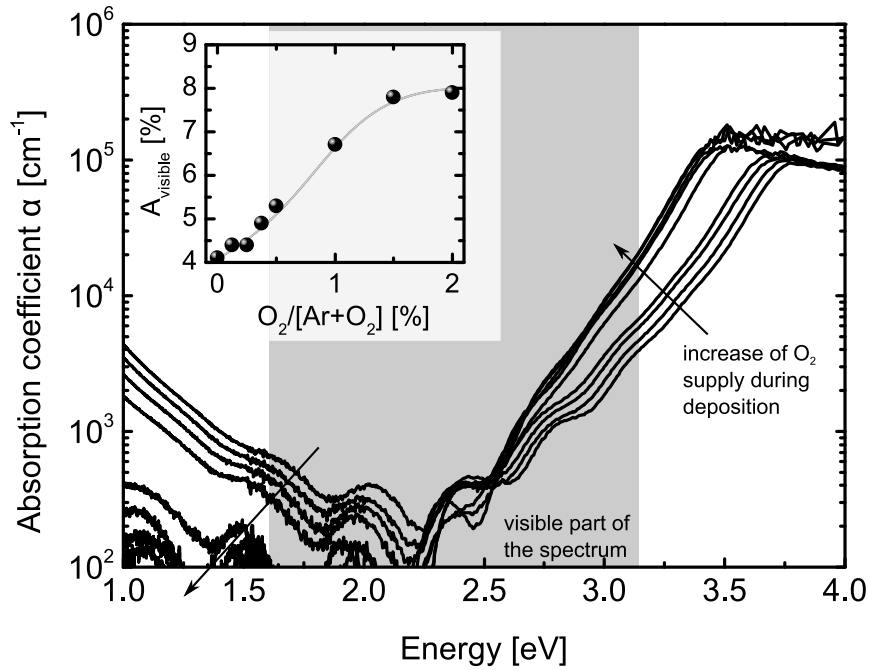


Figure 3.23: Absorption coefficient of the samples of the oxygen series in their as deposited state; The grey area illustrates the visible part of the spectrum. As inset the absorptance in the visible range of the spectrum A_{visible} as function of the oxygen to argon ratio of the sputter gas during deposition is given.

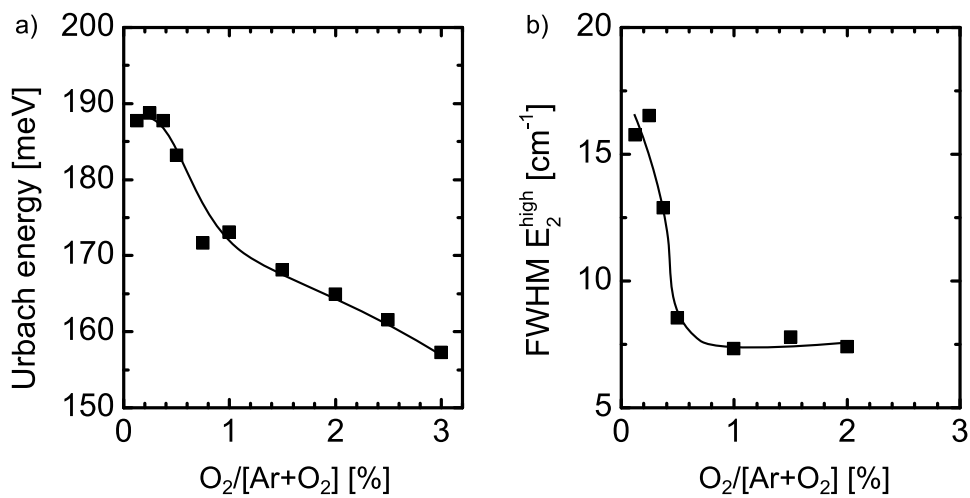


Figure 3.24: a) Urbach energy E_U and b) FWHM of the Raman E_2^{high} mode of thermally treated ZnO:Al layers as function of oxygen to argon ratio in the atmosphere during growth

3 Change of physical properties of ZnO:Al thin films after thermal treatments

visible range of the spectrum (390 - 790 nm and 3.18 - 1.6 eV, respectively), is depicted in the inset.

It can be seen that the increase of oxygen supply during growth shifts the band gap but does not significantly alter the slope of the fundamental absorption edge. Just slight narrowing of the Urbach tails can be recognised.

The redshift of the optical band edge energy due to decreasing carrier concentration with increasing oxygen supply means that the still pronounced absorption tails are pushed into the band gap. Accompanied by this shift is a minor reduction of absorption in the red part of the spectrum due to a decrease in free carrier absorption. However, the enlarged absorption in the blue part dominates and leads to a greenish appearance of ZnO:Al films.

Figure 3.24 a) presents the extracted Urbach energies E_U according to the model described in equation 2.42. Over the studied range of oxygen concentrations in the deposition atmosphere, the width of the Urbach tail E_U decreases steadily from around 190 meV down to 160 meV. However, generally it can be said that for this wide range of oxygen supply during growth, which affects the electrical and structural properties of the layers significantly, the sub-band gap absorption remains on a high level.

A comparison of the Urbach energy with the width of the Raman E_2^{high} mode for the samples of the temperature series in section 3.1 allowed the assumption that structural defects, modifying the Raman response, are causing these absorption tails. This cannot be confirmed regarding the correlation between E_U and the FWHM of the E_2^{high} mode for the samples of the oxygen series. A direct correlation, as observed for the substrate temperature series, would lead to much lower Urbach energies in the range of 50-75 meV for samples deposited above 0.75 % oxygen to argon ratio in the deposition atmosphere.

If structural defects cause Urbach tails, than the evolution of such tails is superimposed by another reason.

3.2.2 Influence of thermal treatments on the structure

Raman spectroscopy

The application of both thermal post-deposition treatments, with and without capping layer, affects the shape of the Raman spectra significantly (see fig. 3.25). It can be assumed, as in case of the samples of the temperature series, that the crystal quality improves with annealing. This is understandable since, by means of the supplied thermal energy, atoms move to energetically more favourable sites and structural rearrangements are possible.

Mode at 574 cm⁻¹

Particularly noticeable is the strong suppression and complete vanishing of the pronounced resonance around 574 cm⁻¹ in case of degradation and cap annealing, respectively, especially for higher oxygen concentrations. As already commented on in section 3.1, this mode is most likely a resonant enhancement of the intrinsic longitudinal optical A_1 phonon mode. This enhancement takes place if real electronic states are in vicinity of the virtual states excited by the Raman excitation source. As shown and described in the following, this

3.2 Systematic variation of oxygen addition during deposition

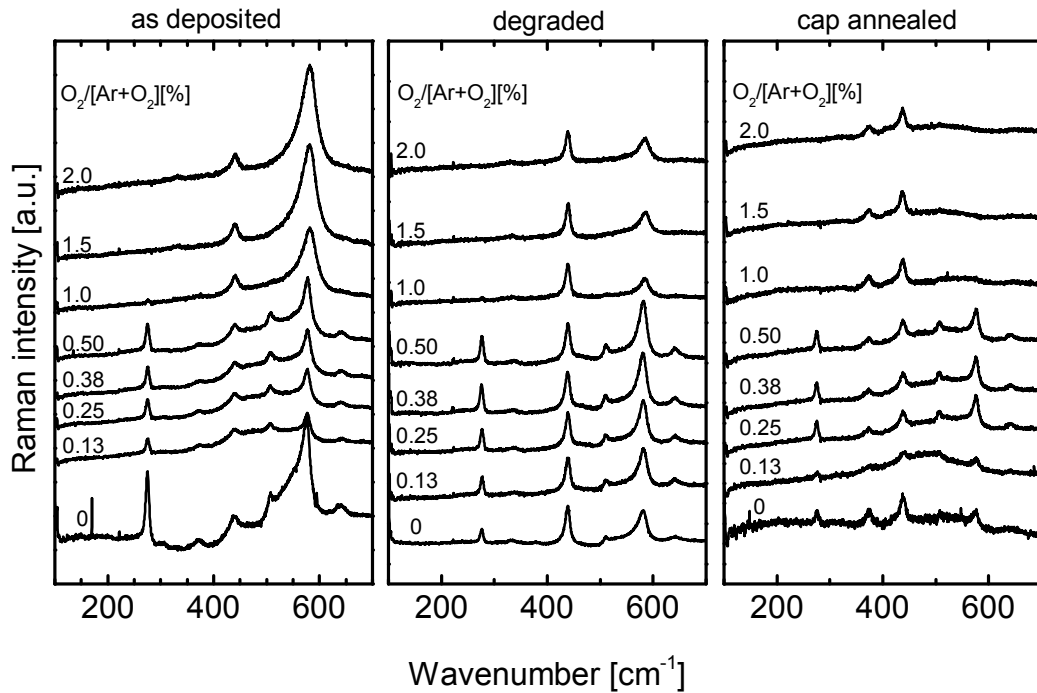


Figure 3.25: Raman spectra of ZnO:Al thin films deposited with variable Ar/O₂ ratio in their as deposited and annealed states; All spectra are normalised to the E₂^{high} resonance.

resonant enhancement is caused by an interaction of position of the energy gap, width of the Urbach tails and an additional absorption feature energetically below the Urbach tail but above the free carrier absorption.

3.2.3 Change of sub-band gap absorption and electronic transport after thermal treatments

Sub-band gap absorption

The left side of figure 3.26 shows the absorption tail width E_U and the right the FWHM of the Raman E₂^{high} mode of samples of the oxygen series after thermal annealing with and without cap.

As in case of the substrate temperature series, both annealing treatments lead to significantly reduced Urbach energies just very weakly depending on the as deposited state. Application of annealing without cap results again in the narrowest absorption tails. A comparison with the FWHM of the Raman E₂^{high} mode, employed as measure for the crystal quality, in the as deposited state did not support the theory that structural defects are the main cause for the development of absorption tails as could be assumed for the results

3 Change of physical properties of ZnO:Al thin films after thermal treatments

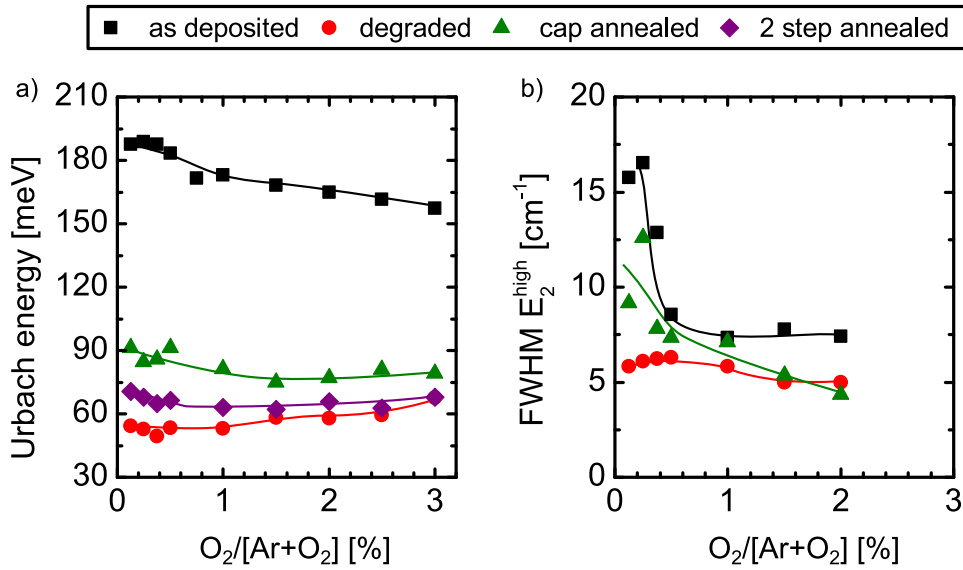


Figure 3.26: a) Urbach energy E_U and b) FWHM of the Raman E_2^{high} mode of ZnO:Al layers as function of oxygen to argon ratio in atmosphere during growth

of the substrate temperature series. However, application of both thermal post-deposition treatments leads to very narrow Raman modes for all samples, indicating significantly improved crystal quality, independent of the applied substrate temperature (fig. 3.14) and the oxygen supply during growth. This strongly reduced FWHM of the E_2^{high} mode after thermal annealing is accompanied by highly suppressed Urbach tails. Therefore, temperature dependent structural defects must be regarded as the main cause of absorption tails superimposed by an oxygen related additional factor.

Correlation between sub-band gap optical absorption and resonant enhancement of the Raman mode at 574 cm^{-1}

The appearance of additional modes (AM) in Raman spectra (figure 3.25) is closely related to the position of the optical band gap energy and the width of the Urbach tail. Figure 3.27 a) shows the intensity of the Raman resonance at approximately 574 cm^{-1} and in part b) the absorbance of the ZnO:Al layers of the oxygen series in their as deposited state, after degradation and after cap annealing. Additionally, the excitation energy of the Raman laser source is indicated with a dashed line at 2.54 eV (488 nm).

Samples in their as deposited state of this series are characterised by a pronounced Urbach tail over the wide range of investigated O_2/Ar ratios during film growth (fig. 3.26). The optical band gap energy of the samples with values between 3.33 and 3.64 eV are energetically considerably far away from the Raman excitation energy of 2.54 eV . However, as it can be seen in figure 3.27, the wide tails are causing non-negligible absorption in the vicinity of the Raman excitation energy. With increasing oxygen content in the growth atmosphere, the carrier concentration decreases and so does the optical band gap energy. This leads to

3.2 Systematic variation of oxygen addition during deposition

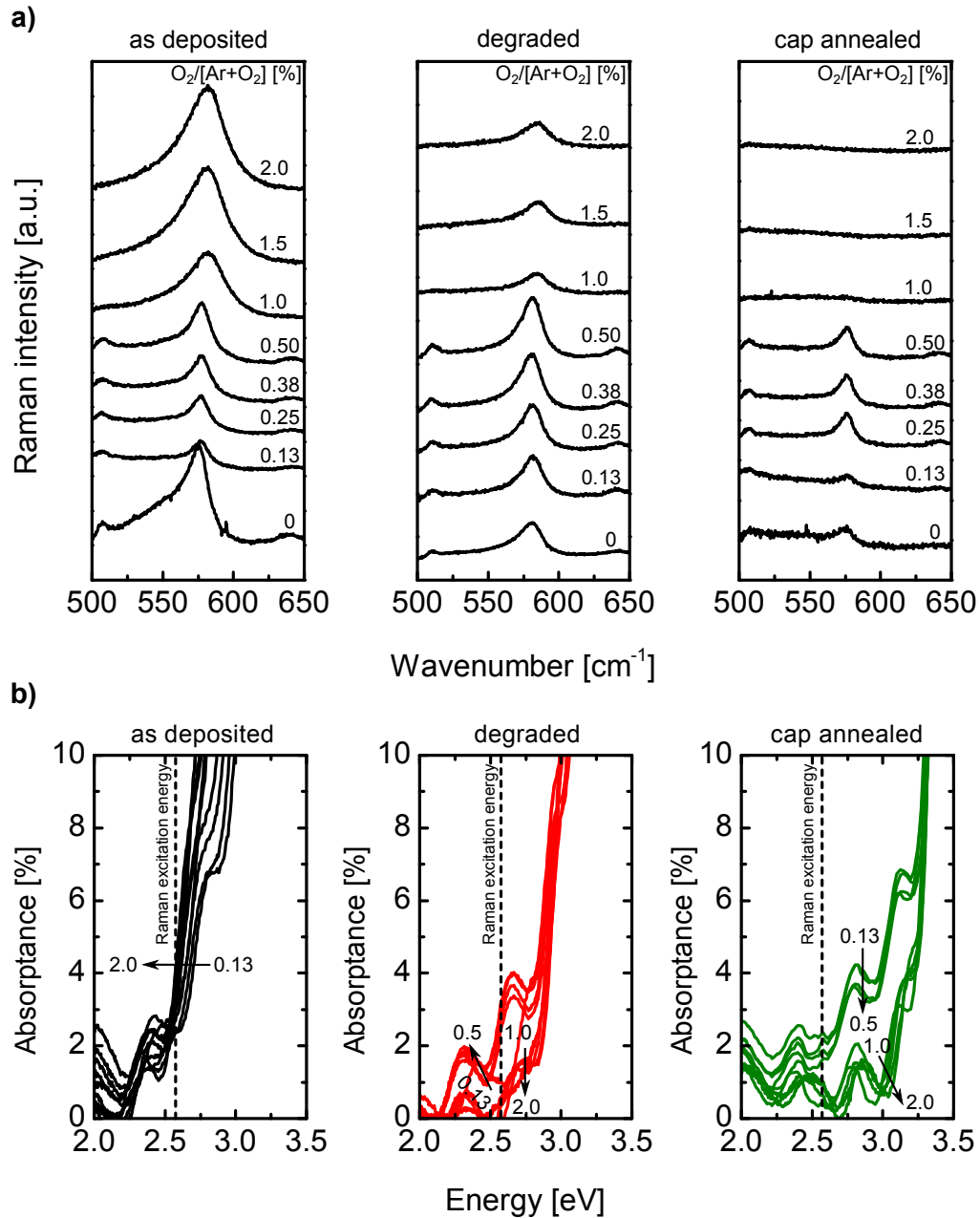


Figure 3.27: a) Raman spectra around the $A_1(LO)$ resonance at 574 cm^{-1} of ZnO:Al deposited under different oxygen to argon ratios in as deposited, degraded and cap annealed state; b) Corresponding absorption coefficients α as function of photon energy; The dotted lines indicate the excitation energy of the Raman laser source. The numbers at the graphs represent the respective oxygen to argon ratio of the sputter gas.

3 Change of physical properties of ZnO:Al thin films after thermal treatments

a small but effective shift of the tails towards the Raman excitation region.

A comparison with the pronounced Raman mode at 574 cm^{-1} (fig. 3.27 a)) it can be obtained that this band gap shift and E_U related enhancement of absorption around 2.54 eV causes an enhancement of the resonance at 574 cm^{-1} , as well.

This becomes even more apparent for the thermally treated samples. The post-deposition treatments of degradation and cap annealing, both, strongly reduce the sub-band gap absorption close to the optical band gap. Therefore, the tail states do not reach the Raman excitation energy as they do for the as deposited samples. However, for both sets of samples, another absorption feature, energetically below the Urbach tail, becomes visible. From the occurrence and intensity of this feature it is dependent whether and how pronounced the mode at 574 cm^{-1} occurs.

For layers deposited with an O_2/Ar ratio from 0.13 up to 0.5 % the 574 cm^{-1} -mode is gaining intensity as does the absorption feature at 2.54 eV . Above 0.5 %, both, the absorption and the intensity of the Raman mode decrease significantly or vanish as in case of the cap annealed layers. It is important to note that not just the appearance but also the intensity of the additional absorption feature below the Urbach tail is very closely connected to the appearance of the AM at 275 cm^{-1} . Since elemental, interstitial Zn is absorbing in this spectral range, it is very likely that the AM at 275 cm^{-1} can be attributed to interstitial Zn, as it was already done in literature [108].

In summary, it can be concluded that for the used excitation source and for low Urbach energies, the appearance of the modes at 275 and 574 cm^{-1} are directly correlated. This correlation, however, is masked for high Urbach energies, hence, wide absorption tails.

Electronic transport

Figure 3.28 shows the carrier concentration n , carrier mobility μ and the resistivity ρ of ZnO:Al layers deposited with additional oxygen in their as deposited state and after degradation, cap annealing and 2 step annealing.

Regarding the carrier concentration of the samples, cap annealing removes the influence of additional oxygen during deposition almost completely. All samples possess a carrier concentration comparable with ZnO:Al deposited without any further oxygen supply. The carrier mobility, however, still shows a dependence on the deposition conditions. A significant increase is still observable even for layers deposited at high oxygen concentration but the mobility does not reach those high values up to $65\text{ cm}^2/\text{Vs}$ achievable for ZnO:Al deposited without or just very little additional oxygen.

The electrical properties of degraded ZnO:Al show just a weak dependence on the oxygen concentration during deposition of the films. Although providing a very different initial state compared to the as deposited material, cap annealing of degraded samples (2 step annealing process) results in very similar behaviour of n , μ and ρ as cap annealing alone.

3.2.4 Discussion regarding oxygen related changes during annealing

As for the samples of the temperature series, the model of Look with the effective mass approaches of Look and Pisarkiewicz have been applied, in order to determine the donor and acceptor concentrations N_D and N_A , respectively.

In figure 3.29 it can be seen that again some cap annealed samples reach the mobility limit predicted by Look. One has to keep in mind that his chosen assumption for the effective mass at the conduction band minimum is rather high and the resulting maximum mobility represents, here, a lower limit. The dashed and dotted lines describe again the development of μ as function of n if a fixed donor concentration is assumed and n is just varied by a change in concentration of acceptors. As in case of the temperature series, this rather simple model is sufficient to describe the electrical properties of oxygen series before and after annealing quite well.

For the proper determination of N_D and N_A , both, have been set as variable parameters in the model of Look. The results of these calculations are shown in figure 3.30.

The observed drop in carrier concentration and mobility with increasing oxygen supply during growth is, according to the model of Look, caused by the creation of compensating acceptors. Interestingly, there is no significant impact on the donor concentration. Hence, an oxidation of Al can be excluded at least for those samples whose electrical properties have been fittable. A decrease in donor concentration, however, cannot be excluded for those samples whose electrical properties have been too poor to obtain reliable results with the compensation model of Look for N_A and N_D .

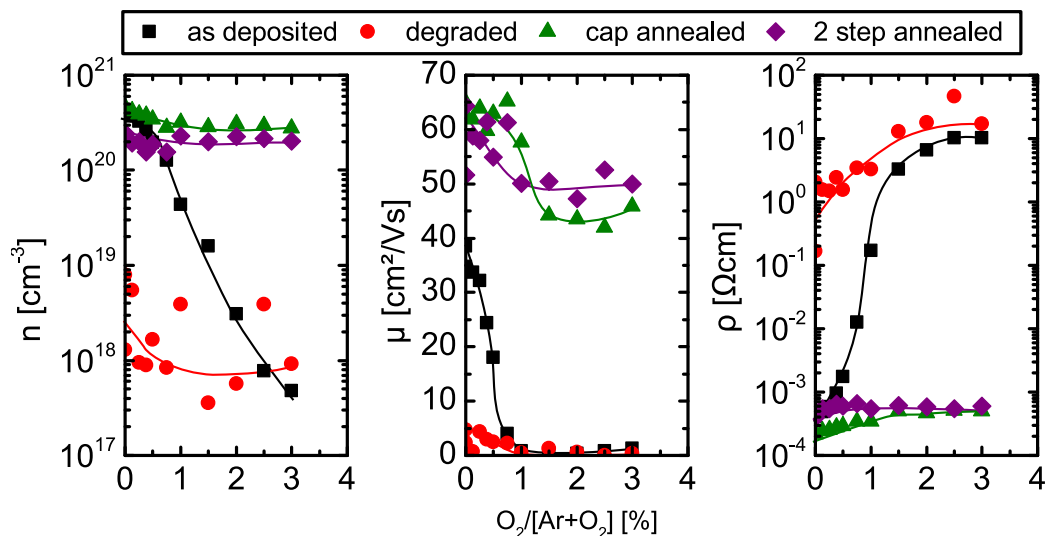


Figure 3.28: Carrier concentration, mobility and resistivity as function of oxygen to argon ratio in sputter atmosphere for the as deposited state and after thermal treatment; The included lines are guides to the eye.

3 Change of physical properties of ZnO:Al thin films after thermal treatments

As in case of the temperature series, a decrease in donor concentration is obtained for those samples annealed with a cap. The drop in N_D after cap annealing becomes larger for increasing oxygen supply during deposition up to 0.75 % and occurs at fairly constant acceptor concentration. For any higher oxygen concentrations, however, the acceptor concentration is influenced, as well. This might be explained, if the acceptors created during deposition with increasing oxygen pair up with donors during the cap annealing. This would result in a drop of N_D related to the oxygen flow for small oxygen addition, while the concentration of effective acceptors is only raised for cap annealed samples originally deposited at high oxygen flow.

This behaviour is very likely structure related. Above that critical oxygen concentration of 0.75 % the degree of c-axis orientation is reduced by development of other growth directions and the vibrational properties of the layers, obtained by Raman spectroscopy, get modified as well.

ZnO:Al layers that got degraded and subsequently cap annealed (2 step annealed) are again characterised by a lower donor concentration as only cap annealed samples, indicating once again that the degradation process obliterates donors which are not recoverable with annealing under a cap.

Generally, it can be noted that for layers grown under oxygen-rich atmosphere (over 2 % O_2 in Ar) it is possible to obtain comparable electrical properties as after annealing without cap (figure 3.12). Thus, it can be assumed that the oxygen partial pressure during annealing plays an important role for the resulting electrical properties.

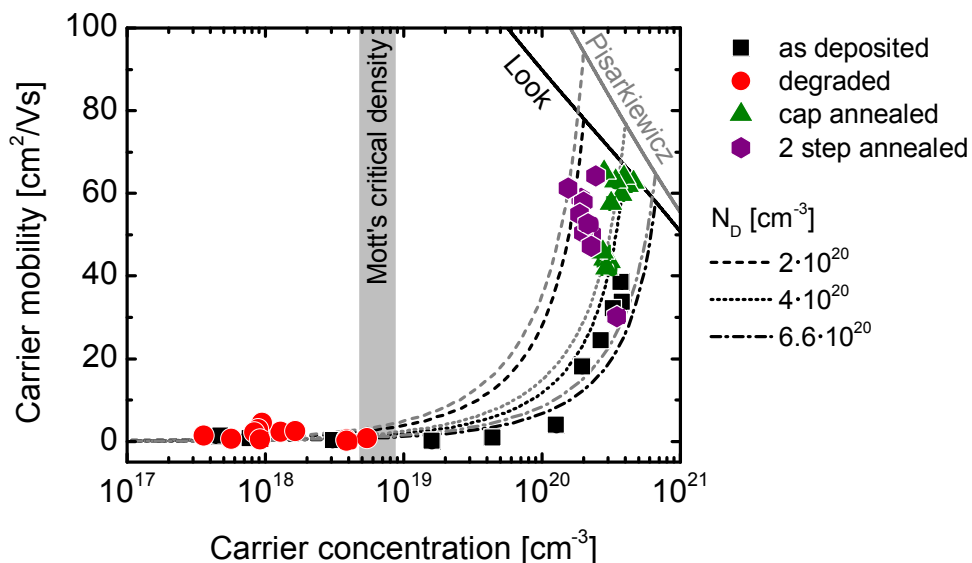


Figure 3.29: Electron mobility as function of electron concentration for as deposited and thermally treated ZnO:Al thin films from the oxygen series; Additionally, the mobility limits of Look and Pisarkiewicz are given (solid lines). The dashed and dotted lines represent the development of μ with increasing acceptor concentration but at fixed donor concentrations of 2, 4 and $6.6 \cdot 10^{20} \text{ cm}^{-3}$.

3.2 Systematic variation of oxygen addition during deposition

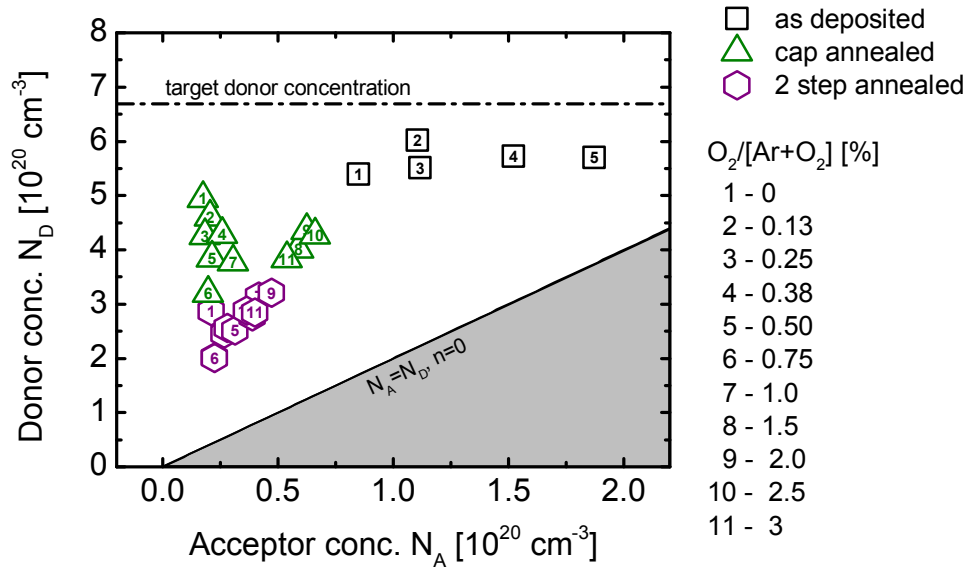


Figure 3.30: Donor and acceptor concentration for the as deposited and annealed ZnO:Al layers of the oxygen series according to the scattering model of D. Look using the effective mass approach of Pisarkiewicz

3.2.5 Summary

Up to a critical oxygen concentration in the growth atmosphere the grains of the resulting layers exhibit almost exclusively (002) orientation. Any further increase modifies the grain growth by benefiting multiple other orientations. This goes along with a change in vibrational properties, e.g. a significantly narrowed Raman E_2^{high} mode, indicating enhanced crystallinity.

In contrast to the findings of the temperature series, this improved crystallinity in the as deposited state is not accompanied by a reduction of sub-band gap absorption. The sub-band gap absorption, described with an Urbach tail, slightly lowers with increasing oxygen supply but remains on a very high level.

Only the application of thermal treatments at high temperature, independent whether with or without cap, is able to diminish the absorption tails at the band edge. Hence, even structurally superior layers suffer decreased transmission in the vicinity of the absorption edge.

The pronounced absorption tails in the as deposited state of the samples can cause a resonant enhancement of the LO phonon modes in Raman measurements again. For the thermally treated samples with very narrow tails, however, it could be shown that a resonant enhancement is not caused by Urbach tails anymore but from absorption related to the appearance of an additional mode at 275 cm^{-1} in the Raman spectra.

As expected, the supply of oxygen during ZnO:Al film growth causes a severe decrease of both, carrier concentration n and mobility μ . By calculating the donor and acceptor

3 Change of physical properties of ZnO:Al thin films after thermal treatments

concentrations, it could be shown that this deterioration of electrical properties is primarily caused by the creation of acceptors.

No significant change in donor concentration could be observed in the as deposited state of the samples up to a critical oxygen concentration in the atmosphere. It indicates that oxidation of Al does not occur in this range but cannot be excluded for higher oxygen quantities.

The enormous increase of mobility after cap annealing can be explained by a reduction of, both, donor and acceptor concentrations, leading to less ionised impurity scattering. The observed recovery of the carrier concentration even for large oxygen supply during growth is due to a disproportionate decrease in number of acceptors.

Annealing without cap decreases, as expected, n and μ at least for those samples deposited with low and intermediate oxygen supply. ZnO:Al layers grown under very oxygen-rich atmospheres (over 2 % O₂ to Ar), however, cannot be degraded any further, indicating that the degradation process during annealing without cap is oxygen related.

3.3 Systematic variation of nitrogen addition during deposition

Nitrogen is always present in industrial sputter coaters for ZnO thin films and is known to deteriorate, both, optical and electrical properties. Since a degradation of optoelectronic properties of bare ZnO:Al is also observable in nitrogen containing annealing atmospheres, it seems obvious to investigate how far small quantities of nitrogen influence the characteristics of ZnO:Al during film growth directly after deposition and after annealing with and without protective capping layer. The analysis of the annealing behaviour in the previous sections demonstrated that the knowledge about structural changes is crucial for evaluation of the optoelectronic properties of ZnO:Al. Therefore, the impact of nitrogen on the structure, determined by means of XRD and Raman spectroscopy measurements, is again presented prior to the analysis of electrical transport and sub-band gap absorption.

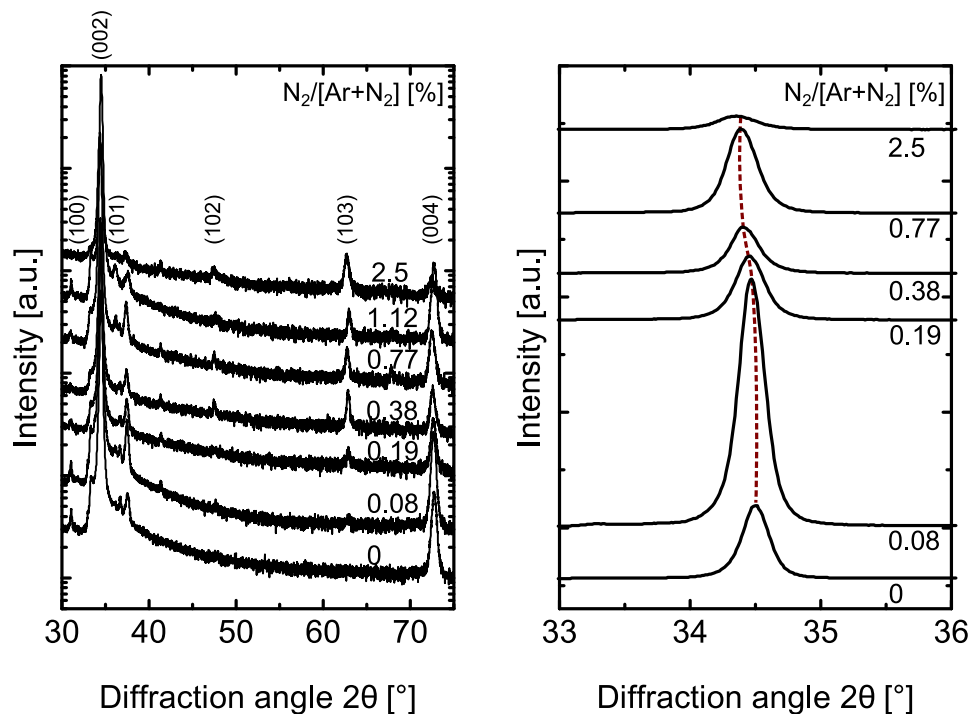


Figure 3.31: X-ray diffraction spectra between 30° and 75° and b) around the (002) reflex as function of the nitrogen partial pressure in the sputtering atmosphere. The shift in position of the (002) reflex is indicated with a red dashed line; All spectra are normalised to their respective layer thickness and vertically shifted for clarity.

3 Change of physical properties of ZnO:Al thin films after thermal treatments

3.3.1 Structural, electrical and optical properties in the as deposited state

Structure, Part I –X-ray diffraction

In figure 3.31 a) full XRD spectra between 30° and 75° and b) a magnification of the range between 33° and 36° of ZnO:Al layers, deposited under nitrogen (N_2) containing atmosphere with variable N_2 content, are shown.

Up to a critical concentration, in this case 0.08 % N_2 of the entire atmosphere, the ZnO:Al films possess a very strong domination of grain growth in [001] direction. Further increase of the N_2 content in atmosphere during growth results in appearance of additional reflexes which can be assigned to the (101), (102) and (103) planes in ZnO. Supply of N_2 , therefore, benefits the growth of grains in directions other than [001] above a certain concentration. Comparing the XRD result with those of the systematic increase of O_2/Ar ratio during deposition (fig. 3.19) it turns out that the supply of both elements, N_2 and O_2 , cause a very similar growth behaviour.

In figure 3.31 b) and figure 3.32 a) it can be seen that the increase of N_2 content in the sputtering gas leads to a shift of (002) position towards smaller angles, hence, a systematic dilatation of the c-axis. Furthermore, a widening of the (002) reflex peak is visible (fig. 3.32 b)) related to a reduction of coherent scattering areas.

The surface morphology of four representative samples is illustrated in figure 3.33 by means of SEM surface micrographs. Already the supply of small quantities of nitrogen causes

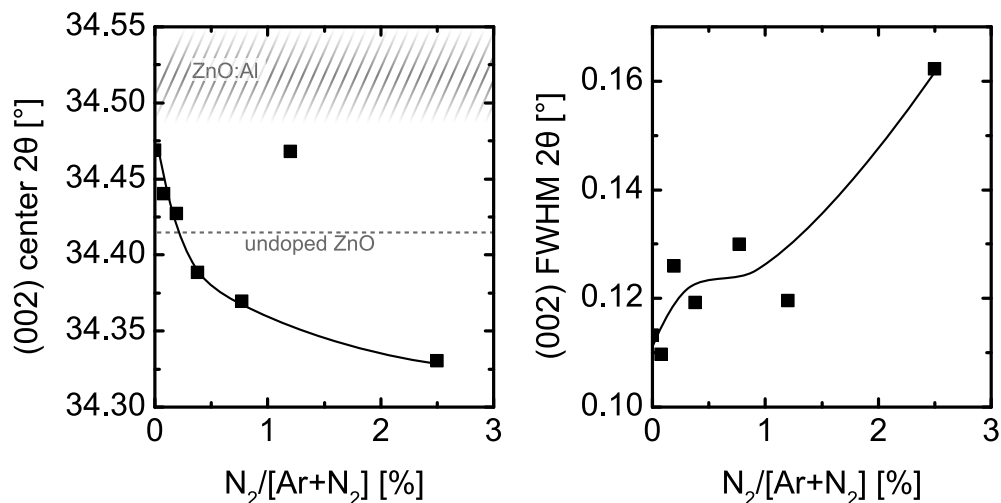


Figure 3.32: Peak position and FWHM of the (002) reflex as function of the nitrogen to argon ratio during deposition; The included lines are guides to the eye. The grey shaded area indicates the range of reference values for Al-doped ZnO. The (002) center position for undoped ZnO is given as grey dashed line.

3.3 Systematic variation of nitrogen addition during deposition

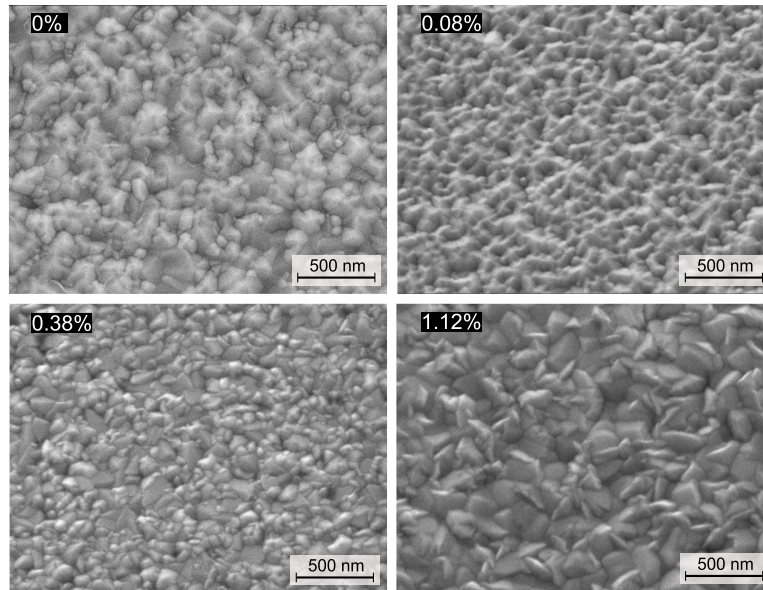


Figure 3.33: SEM surface micrographs of ZnO:Al layers deposited under nitrogen containing atmosphere; The N_2/Ar ratio is given at the respective image; The images were taken from samples tilted by 30° .

very different surface morphologies of the respective ZnO:Al films as could already be suspected considering the XRD results.

Structure, Part II –Raman spectroscopy

Figure 3.34 shows an overview of Raman spectra of ZnO:Al deposited under systematically increased nitrogen concentration in the growth atmosphere.

The dominating resonances for all samples are the additional mode at 275 cm^{-1} and the mode at 575 cm^{-1} . The intrinsic E_2 modes are already weak for samples deposited at very low nitrogen concentrations and vanish completely later on. Furthermore, a systematic broadening or smearing of all appearing resonances can be observed indicating strong deterioration of the structural quality.

Combined with the results of the XRD measurements it can be concluded that nitrogen incorporation mainly perturbs the vibration properties than the general growth behaviour of the lattice, i.e. it mainly changes the point defect concentration, for which XRD spectroscopy is rather insensitive.

Mode at 574 cm^{-1}

The resonance at 574 cm^{-1} was assigned to the resonant enhanced $A_1(\text{LO})$ mode in the previous two sections. The occurrence of this resonance is closely connected to the appearance of the AM at 275 cm^{-1} in case of small Urbach tails. Here, both modes are only together present, as well.

3 Change of physical properties of ZnO:Al thin films after thermal treatments

However, as it will be seen in the following subsection, nitrogen containing ZnO:Al layers possess pronounced sub-band gap absorption in the visible range including the spectral area around 2.54 eV, the used Raman excitation energy. Hence, the presence of absorbing states in vicinity of this energy would again explain the resonant enhancement of the intrinsic $A_1(\text{LO})$ mode at 574 cm^{-1} .

Mode at 275 cm^{-1} and 510 cm^{-1}

For all nitrogen concentrations, the AM at 275 cm^{-1} is present and very distinctive. While it seems to increase slightly up to 0.12 % of the nitrogen to argon ratio in the sputtering gas it starts to broaden severely for any higher concentrations. For the temperature and oxygen series the resonances at 275 and 510 cm^{-1} occur always simultaneously. For the nitrogen containing samples, however, the resonance at 510 cm^{-1} vanishes in case of high nitrogen concentrations even though the 275 cm^{-1} mode is still obtruding.

Electrical properties

Nitrogen incorporation strongly influences the electrical properties of ZnO:Al. As it can be seen in figure 3.35, both, electron concentration n and mobility μ , decrease significantly above a nitrogen concentration of 0.12 %. For concentrations above 0.4 %, the electrical

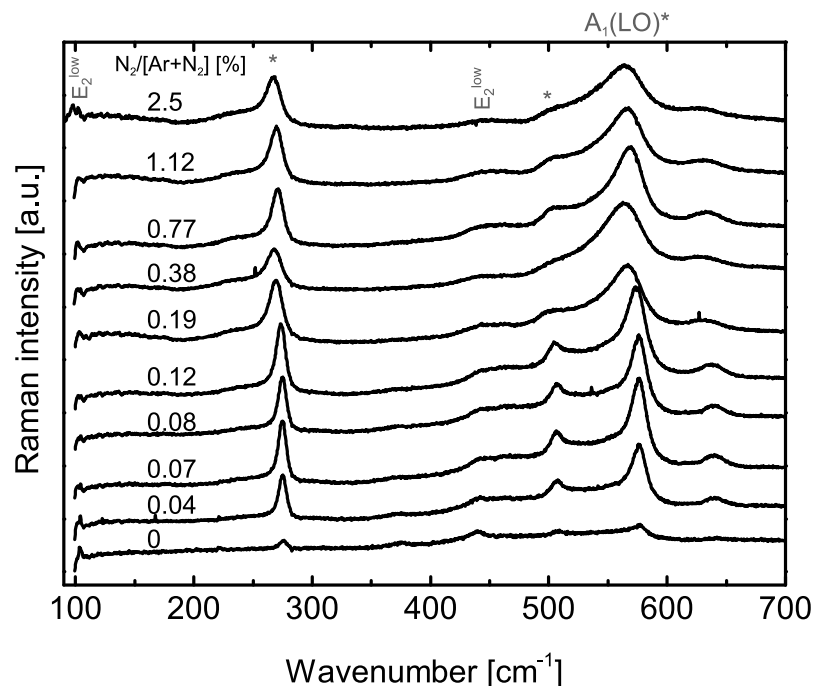


Figure 3.34: Raman spectra of ZnO:Al deposited under systematically increased nitrogen concentration in growth atmosphere; All spectra are vertically shifted for clarity.

3.3 Systematic variation of nitrogen addition during deposition

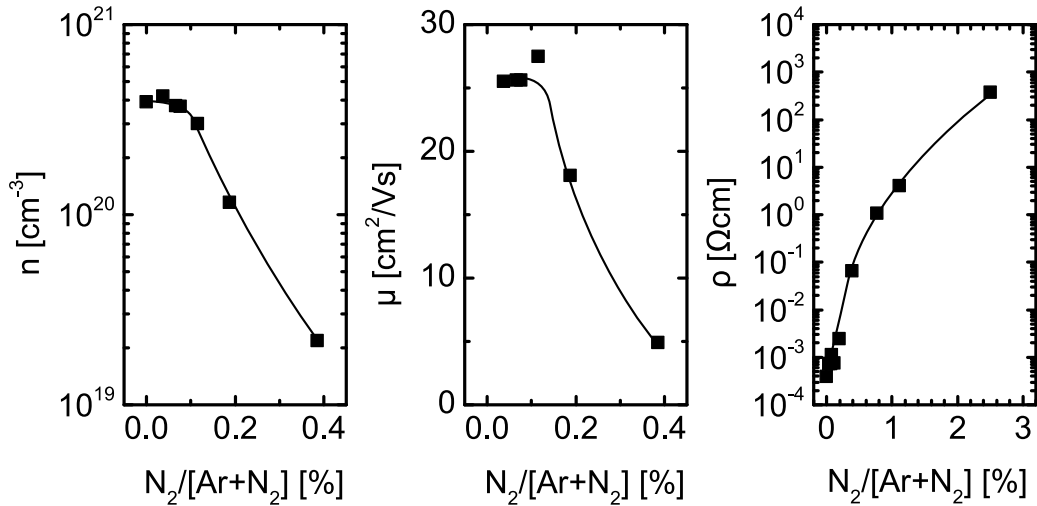


Figure 3.35: Carrier concentration n , carrier mobility μ and resistivity ρ as function of nitrogen content in atmosphere

properties have not been determinable by Hall measurements, anymore.

Instead, the resistivity has been determined by the layers thickness and its resistance, measured with a four-point-probe. The resistivity gradually increases with raising N_2 to Ar ratio during growth over six orders of magnitude. The strong deterioration of n and μ coincide with the sudden significant broadening of all resonances observable in the corresponding Raman spectra, that is related to reduced crystal quality. However, it is expected that structural depreciation is not the main reason for the strongly decreased carrier concentration and mobility, but the creation of ionised impurities due to the incorporation of nitrogen as acceptor, which will be discussed later on.

Sub-band gap absorption

The nitrogen supply during growth has a considerable influence on the optical properties of the resulting ZnO:Al layers. As it can be seen in figure 3.36 a), an increase of nitrogen content in the sputter atmosphere is leading to the development of a broad absorption feature in the visible range of the spectrum, which gives the ZnO films a yellow-brownish appearance.

This additional absorption cannot be fitted with a simple Urbach tail, as can be seen in figure 3.36 b). Here, an exemplary set of absorption coefficient data is shown. Since the model described by eq. 2.42 and introduced in section 3.1 has to be adapted, a Gaussian function was added to account for the nitrogen related absorption feature:

3 Change of physical properties of ZnO:Al thin films after thermal treatments

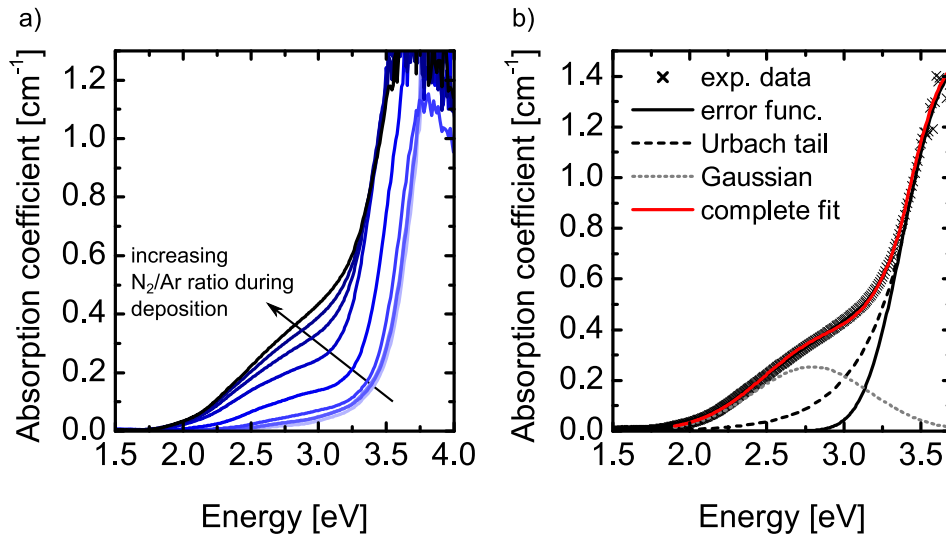


Figure 3.36: a) Development of absorption for ZnO:Al deposited with increasing amount of nitrogen in sputter atmosphere; b) Exemplary absorption coefficient of nitrogen containing ZnO:Al and fit with model according to eq. 2.42 with addition of a Gaussian

$$\alpha(E) = \begin{cases} A \times \left(\operatorname{erf}\left(\frac{E-E_g}{\Gamma}\right) \right) + 1, & \text{for } E > E_0 \\ \exp\left(\frac{E-E_c}{E_U}\right) + \alpha_0 + \frac{F}{w\sqrt{\pi/2}} \cdot \exp\left(-\frac{2(E-E_{gc})^2}{w^2}\right) & \text{for } E \leq E_0, \end{cases} \quad (3.1)$$

where F is area of the Gaussian, E_{gc} its center position and w the width. As it can be seen in fig. 3.36 b), this extension agrees very well with the experimental data.

3.3.2 Changes of properties after application of thermal treatment

The main aim of nitrogen doping in this work is to clarify the role of nitrogen during the annealing process of ZnO:Al.

So far it was shown that the incorporation of nitrogen during growth results in a strongly enhanced resistivity of the ZnO:Al layer very similar to the results obtained by thermally treated samples in nitrogen atmosphere.

For further investigations, the degradation process has been slightly varied. Bare ZnO:Al layers deposited at 200 °C and using a sputter atmosphere containing 1.12 % and no N₂ have been thermally treated in the standard annealing atmosphere at temperatures between 300 °C and 600 °C for two hours.

Additionally, all samples of that series have been subjected to the standard degradation and cap annealing procedures as done for the ZnO:Al layers of the temperature and oxygen series.

3.3 Systematic variation of nitrogen addition during deposition

Structure

The XRD spectra of weakly annealed nitrogen containing ZnO:Al layers in dependence of the treatment temperature can be seen in figure 3.37. Except of the (002) reflex position, no major change upon annealing can be observed. Hence, a recrystallisation of the material due to the provided thermal energy can be excluded again.

The (002) reflex position is shifted for any annealing temperature towards smaller angles, indicating an increase in interplane distance parallel to the c-axis.

Electronic transport

Figure 3.38 shows the resistivity of the ZnO:Al layers annealed without cap for two hours at 300, 400, 500 °C and 600 °C and for 24 hours at 550 °C in nitrogen. The latter conditions correspond to the standard degradation process.

Here, it can be seen that, depending on the treatment temperature, two different groups of treatment results can be distinguished.

Thermal treatments for two hours with a temperature below 400 °C result in comparable or slightly improved resistivity. A short annealing between 500 °C and 600 °C, however, increases the resistivity by approximately three orders of magnitude independent of the

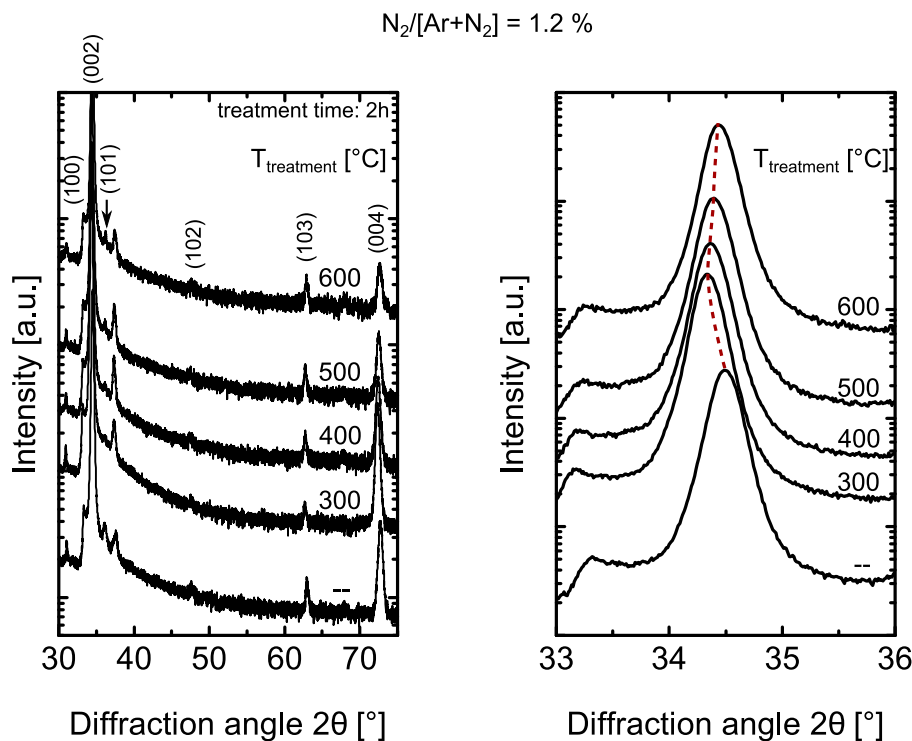


Figure 3.37: XRD spectra of nitrogen containing ZnO:Al in their as deposited state and after short thermal treatments at 300, 400, 500 °C and 600 °C; Treatment time was set to two hours in all cases.

3 Change of physical properties of ZnO:Al thin films after thermal treatments

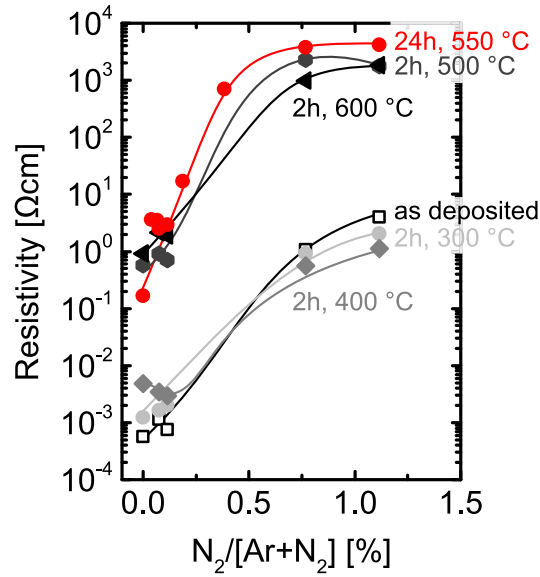


Figure 3.38: Resistivity of ZnO:Al after annealing without cap for 24 hours at 550 °C and for two hours at 300, 400, 500 and 600 °C, respectively, as function of nitrogen to argon ratio during growth; The included lines are guides to the eye.

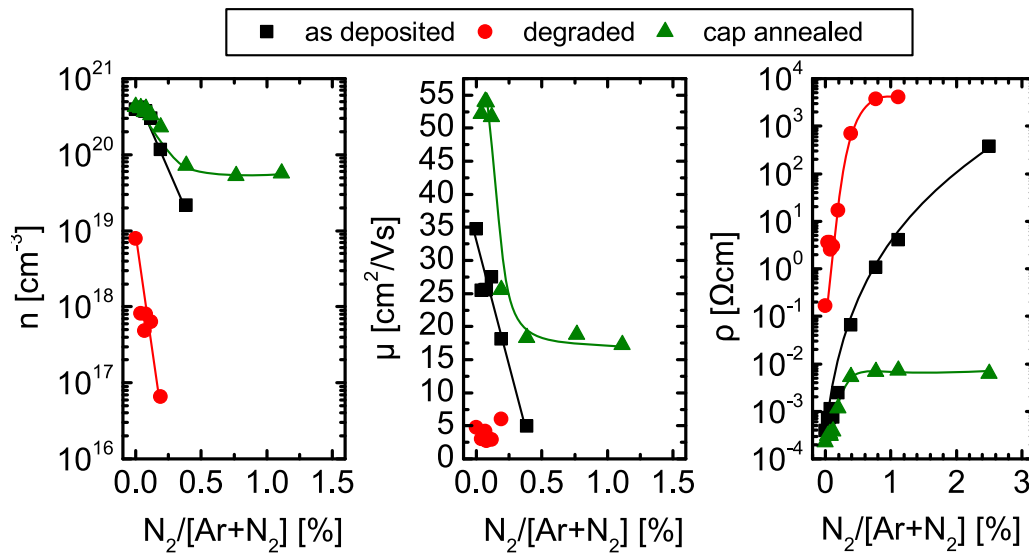


Figure 3.39: Carrier concentration n , carrier mobility μ and resistivity ρ as function of nitrogen content in the deposition atmosphere for ZnO:Al layers in their as deposited state and after degradation and cap annealing, respectively. The included lines are just guides to the eye.

3.3 Systematic variation of nitrogen addition during deposition

nitrogen concentration during deposition. An extension of the treatment time, as in case of the standard degradation process (24 h), has just a subordinate influence on the resistivity. Hence, strong degradation of the electrical properties during thermal annealing occurs somewhere between 400 °C and 500 °C, even for those samples deposited already under a nitrogen rich atmosphere, and is most probably caused by a deactivation or compensation of donors.

For further analysis, Hall measurements have been carried out on ZnO:Al layers grown using nitrogen containing atmosphere in their as deposited state and after the standard degradation and cap annealing process. Due to a very low conductivity, Hall measurements could not be applied on all samples. Therefore, four-point probe measurements, as described in section 2.2.2.2, have been employed to determine the resistance of all samples. The results can be seen in figure 3.39.

In case of nitrogen addition, the general trend observed for the previous sample series still applies: cap annealing improves electrical properties while application of the degradation process causes deterioration. For high nitrogen concentrations, carrier concentration, mobility and, hence, resistivity seem to saturate after application of cap annealing. The same applies for the resistivity of the degraded samples but on a much higher level. Their carrier concentration and mobility have been mainly too low to determine by Hall measurements.

Sub-band gap absorption

Figure 3.40 shows the absorption coefficient for ZnO:Al layers deposited without and with up to 1.2 % nitrogen content in the sputtering gas in their as deposited, degraded and cap annealed state.

The application of the thermal treatments result, again, as for any other samples so far, in

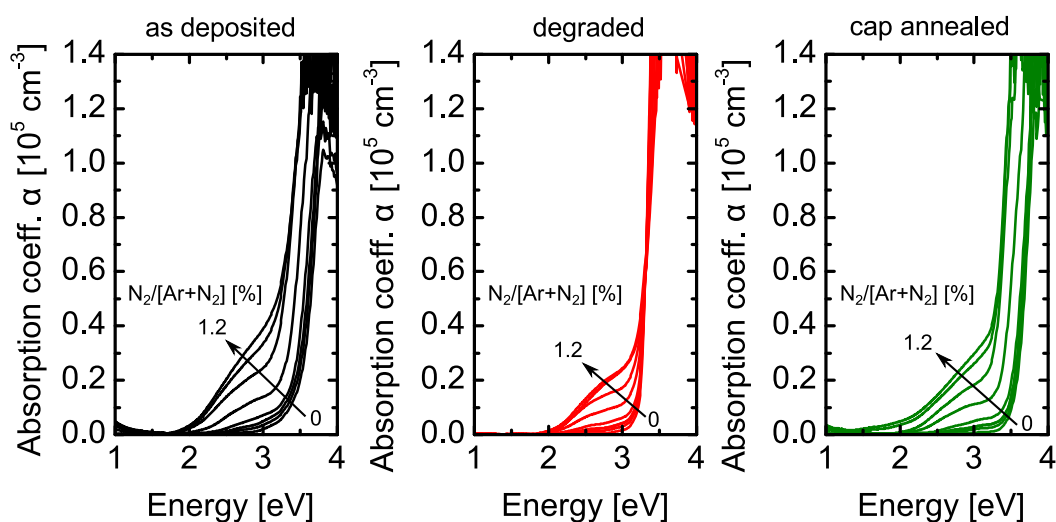


Figure 3.40: Absorption coefficient for the ZnO:Al layers of the nitrogen series in their as deposited, degraded and cap annealed state

3 Change of physical properties of ZnO:Al thin films after thermal treatments

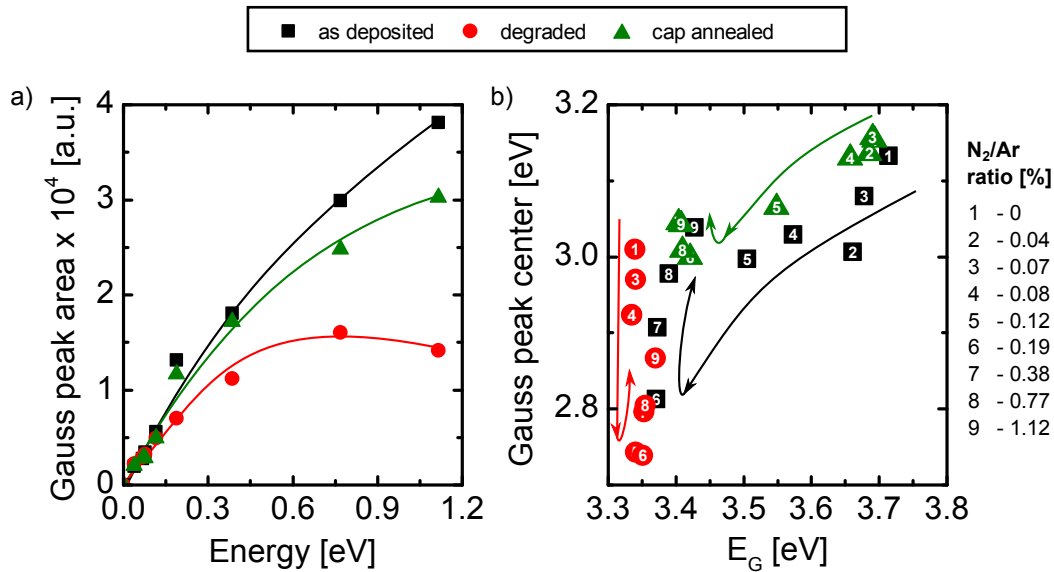


Figure 3.41: a) Gaussian peak area as function of nitrogen to argon ratio of the sputtering atmosphere and b) Gaussian peak center as function of the optical band gap energy for the samples of the nitrogen series

very steep absorption edge slopes. Furthermore, a shift of the optical band gap towards lower energies, due to the significant decrease in carrier concentration, can be observed for the degraded samples. Interestingly, the nitrogen related absorption feature gets reduced for both thermal treatments but does not vanish completely. Additionally, a shift of its position is observable.

The by means of eq. 3.1 extracted Gaussian peak width and its center are shown in figure 3.41. Compared to the annealing with cap, annealing without cap leads to significantly smaller Gaussian peak areas (figure 3.41 a)). Assuming that a reduction of absorption in this spectral range is related to the removal of nitrogen from the ZnO lattice, this result is comprehensible since nitrogen can diffuse more easily into an a-Si capping layer is not present.

It can be observed that the applied treatments are apparently not able to remove that absorption completely. This fact is also demonstrated by energy-dispersive X-ray spectroscopy (EDX) measurements, that are discussed at a later point.

Part b) of figure 3.41 shows the extracted Gaussian peak center positions. As already mentioned earlier, it is expected that nitrogen incorporation into ZnO leads to the creation of acceptors, compensating intrinsic and extrinsic donors.

The origin of this broad absorption band could, indeed, be nitrogen as deep acceptor. In contrast to the prevailing opinion that substitutional nitrogen is a *shallow* acceptor with a position of a few 0.1 eV above the valence band maximum (VBM) [13, 125], there is strong evidence that nitrogen actually forms a *deep* acceptor. This situation is illustrated

3.3 Systematic variation of nitrogen addition during deposition

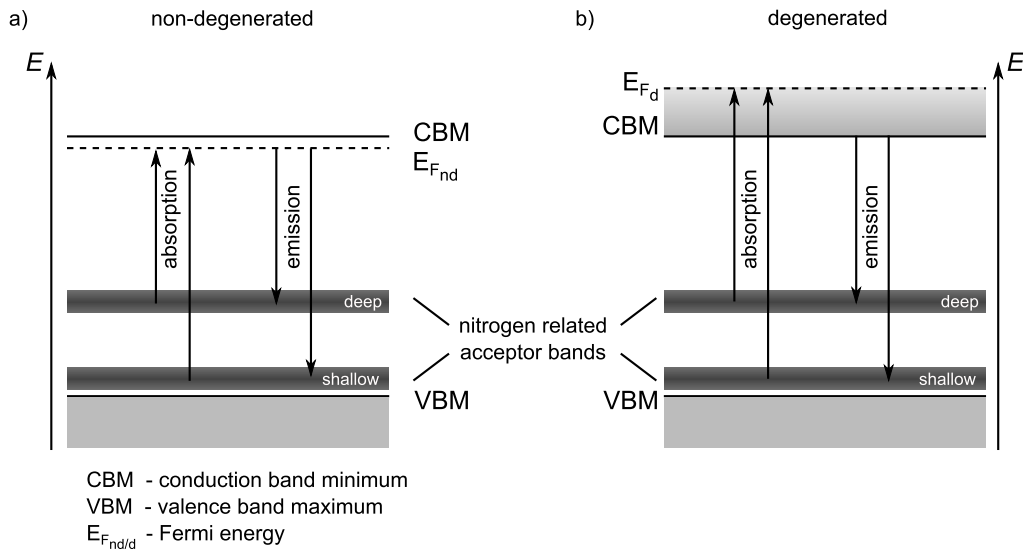


Figure 3.42: Schematic band diagram of a) non-degenerated and b) degenerated ZnO with nitrogen related possible acceptor bands

in figure 3.42 a).

Garces *et al.* found an optical absorption band down to 2.25 eV after annealing undoped ZnO single crystals in nitrogen between 600 °C and 900 °C [120]. Furthermore, they could show by means of EPR measurements¹⁰ that neutral (paramagnetic) nitrogen acceptors can be photoinduced when excited by a laser source with various photon energies down to as low as 2.4 eV. An excitation energy of 2.4 eV should not be able to remove an electron from an acceptor state in ZnO if its energy position is just a few 0.1 eV above the VBM. Lyons *et al.* predicted, by means of advanced first principle calculations of N doped ZnO, the existence of a broad absorption band centering at 2.4 eV with an onset around 2.1 eV caused by deep nitrogen acceptors [127]. The relaxation of that excited acceptor should occur at an energy of 1.7 eV for which Tarun *et al.* found experimental evidence by means of photoluminescence spectroscopy [128].

The Gaussian peak center positions obtained for the here investigated films are slightly higher than the 2.4 eV predicted by Garces and Lyons *et al.*. This is expectable since the ZnO films investigated here are highly Al-doped and are, except for some samples treated with the degradation procedure, always strongly degenerated. Since the Fermi energy is located above the conduction band minimum (CBM) this offset has to be taken into account when evaluating the energetic position of the nitrogen related acceptor which is assumed to be responsible for the additional absorption feature. This situation is depicted in figure 3.42 b). The Gaussian centre position for the samples in their as deposited state, as well as after both thermal treatments, show a generally decreasing trend with decreasing optical band gap energy up to 0.38 % N₂ in the sputtering gas. This indicates a decrease in Fermi energy.

¹⁰Electron paramagnetic resonance (EPR) measurements detect paramagnetic states in the material by means of resonant microwave absorption. For an introduction in EPR spectroscopy see [126].

3 Change of physical properties of ZnO:Al thin films after thermal treatments

Therefore, the Gaussian centre position should shift towards lower energies, as well. Above 0.38 % N₂ the Gaussian position shifts again towards higher energies, but at nearly unchanged band gap energy. Those ZnO:Al films possess a carrier concentration below approximately $5 \cdot 10^{18} \text{ cm}^{-3}$ and are at the transition point to non-degeneracy (see section 2.1.3). Therefore, the optical band gap is fairly independent of the carrier concentration and, hence, unaffected by a further rise of nitrogen and acceptor concentration, respectively, in the layer.

The nevertheless occurring shift in position of the Gaussian peak coincides with significant broadening of Raman resonances and a vanishing E_2^{high} mode, as could be seen in figure 3.34. Hence, it can be suggested that a change of crystal quality might be correlated with it.

In order to clarify the influence of the the nitrogen content on the appearance of the additional absorption feature EDX measurements have been carried out to determine the composition of selected samples. The results are illustrated in figure 3.43.

As already expected, an increase of the nitrogen concentration in the sputter atmosphere results also in an enhanced incorporation of nitrogen in the deposited ZnO:Al.

If nitrogen is incorporated into ZnO:Al when a concentration of 0.08% nitrogen in the sputtering gas is chosen, the resulting nitrogen content in the layer is below the detection limit of EDX¹¹.

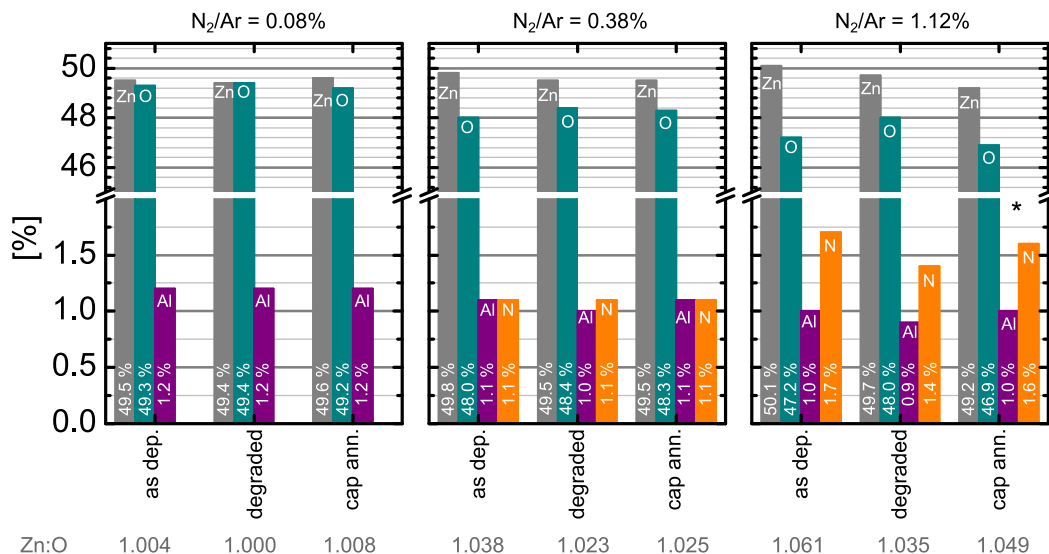


Figure 3.43: EDX determined material composition of ZnO thin films doped with Al and N in their as deposited state and after degradation and cap annealing, respectively; Below each sample, the zinc to oxygen ratio is given. The sample marked with an asterisk contained as only one additionally 1.3 % fluorine, which is most likely a remain of the NF₃ etch process after cap annealing.

¹¹For most elements with an atomic number greater than ten (i.e. sodium), the detection limit can

3.3 Systematic variation of nitrogen addition during deposition

An increase of nitrogen concentration in the sputtering atmosphere to 0.38 % results in a nitrogen content of 1.1 %_{at} in the grown ZnO film. Simultaneously, the stoichiometry of the ZnO film deteriorates slightly, meaning that the oxygen content decreases by around 1 %_{at}. This indicates that nitrogen is mainly incorporated at oxygen sites, producing N_O acceptors as already suspected regarding the electrical and optical properties of the sample.

After application of the degradation and cap annealing treatments, the nitrogen content in the layer remains stable although the observation of a decreased additional absorption around 2.8 eV after degradation suggests a decrease in nitrogen content.

However, the reduction in intensity of this absorption is not pronounced, therefore, it can be expected that nitrogen might be released in the range of the detection error of EDX. The intensity of the additional absorption feature, quantified by the Gaussian peak area (fig. 3.41) does not differ significantly after cap annealing from the as deposited state of the nitrogen containing samples. This is consistent with the finding of a nearly unchanged nitrogen content by means of EDX.

According to figure 3.41 a), a stronger reduction but not complete removal of nitrogen content in the ZnO:Al film is expected for the sample deposited with 1.12 % nitrogen in the sputtering gas. Here, the decrease in nitrogen related absorption is much larger after degradation than after cap annealing.

As a matter of fact, this trend can be observed regarding the EDX results of the sample. The layer has, as expected, in its as deposited state a larger nitrogen content compared to those samples deposited with lower nitrogen concentrations. Degradation of the ZnO:Al layer leads to a decrease in nitrogen content of 0.3 %_{at}, while cap annealing, on the other hand, reduces the nitrogen content in the layer just by 0.1 %_{at}, improving both the Zn to O ratio.

Considering the electrical and optical properties in combination with the EDX results, it can be concluded that raising the nitrogen content in the growth atmosphere increases the the number of N_O acceptors in the material, resulting not just in a degradation of electrical properties but significant sub-band gap absorption as well. Nitrogen, once incorporated, cannot be removed completely applying the, here, investigated thermal treatments.

roughly be estimated to 0.1–0.2 %_{wt}. For elements of lower atomic number, like nitrogen and oxygen, the detection limit is significantly larger.

3 Change of physical properties of ZnO:Al thin films after thermal treatments

3.3.3 Discussion of nitrogen incorporation during annealing without cap in nitrogen ambient

Figure 3.44 presents a comparison of electrical properties of ZnO:Al from the substrate temperature and the nitrogen series. One has to keep in mind that all samples of the nitrogen series have been deposited at 200 °C and the substrate temperature itself has strong influence on the properties of the resulting ZnO:Al thin film. For better comparison, in figure 3.44 the samples of the temperature series deposited at 200 °C have been specially marked.

ZnO:Al films deposited with high nitrogen content in the deposition atmosphere are, indeed, electrically comparable to degraded films, deposited at same temperature but without nitrogen in the sputtering gas. Hence, acceptors created by nitrogen incorporation during annealing without cap in nitrogen could be responsible for the observed strong decrease in carrier concentration and mobility.

However, regarding the optical properties, major differences can be observed. Figure 3.45 illustrates a comparison of absorption coefficients of ZnO:Al films obtained by application of thermal degradation process and ZnO:Al deposited with additional oxygen and nitrogen,

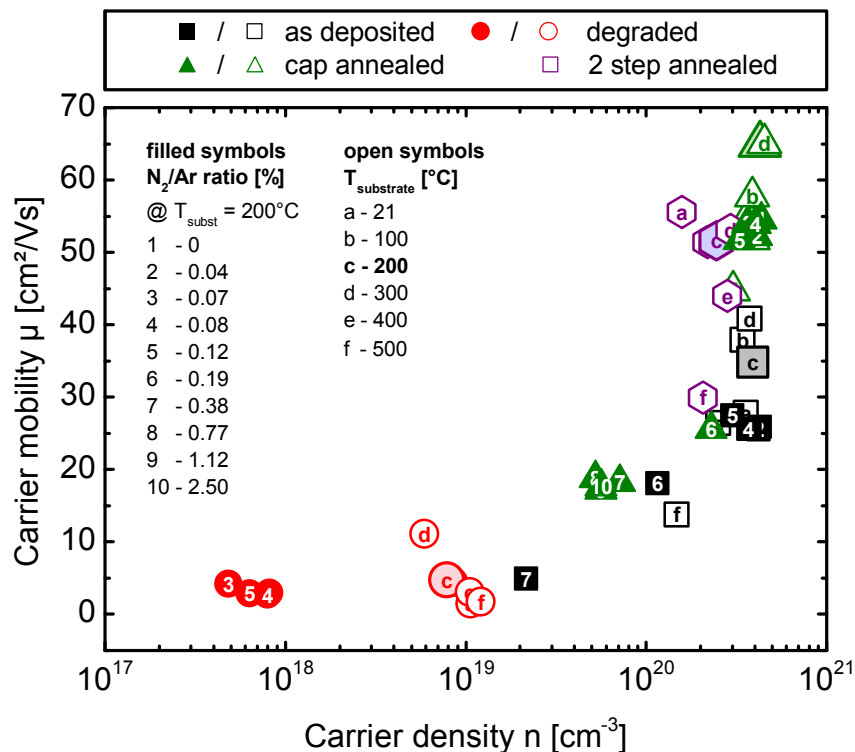


Figure 3.44: Carrier mobility μ as function of carrier concentration n for the samples of the nitrogen series (filled symbols) and temperature series (open symbols); Since the samples of the nitrogen series are deposited at 200 °C the corresponding samples of the temperature series are specially marked.

3.3 Systematic variation of nitrogen addition during deposition

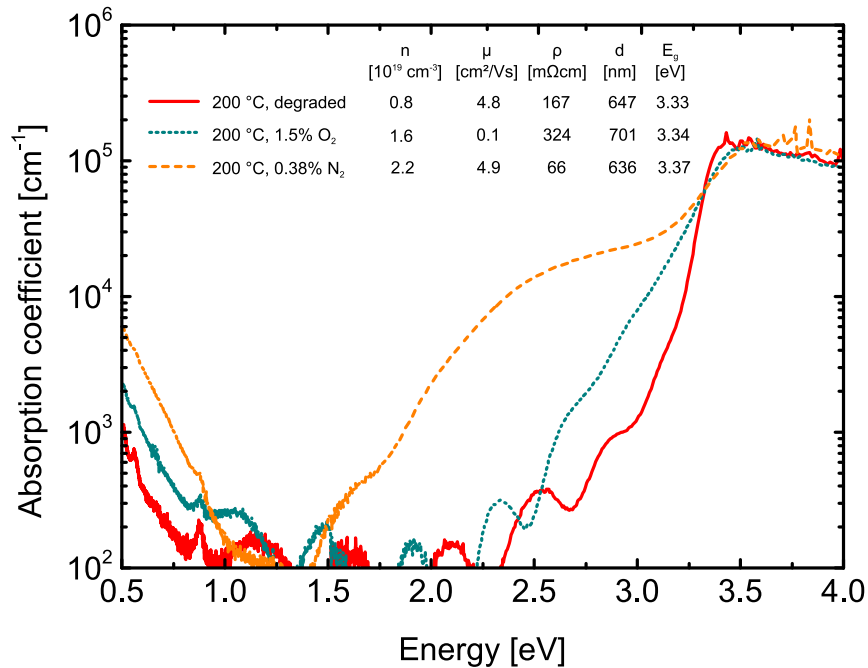


Figure 3.45: Comparison of absorption coefficient of ZnO:Al layers obtained by thermal degradation and ZnO:Al deposited with additional oxygen and nitrogen, respectively, yielding comparable electrical properties; All samples have been deposited at 200 °C and with the same sputter conditions apart from the additional gas supply.

respectively, yielding all comparable electrical properties and layer thickness.

However, regarding the optical properties, major differences can be observed. Figure 3.45 illustrates a comparison of absorption coefficients of ZnO:Al films obtained by application of thermal degradation process and ZnO:Al deposited with additional oxygen and nitrogen, respectively, yielding all comparable electrical properties and layer thickness.

The optical absorption properties of ZnO deposited with additional oxygen are very similar to the absorption behaviour of the degraded ZnO:Al films without any addition of impurity gas during deposition. They vary merely in the slope of the fundamental absorption edge, the Urbach tail. The degraded film is characterised by a very steep absorption edge, which is caused by the temperature of the treatment. Oxygen incorporation, as discussed above, has just inferior influence on the shape.

When the amount of nitrogen necessary to reach the electrical properties of degraded ZnO:Al films is incorporated, an additional absorption feature appears.

Hence, nitrogen incorporation can be excluded as main cause of degradation of electrical properties during annealing without cap in nitrogen ambient.

3 Change of physical properties of ZnO:Al thin films after thermal treatments

3.3.4 Summary

Nitrogen supply to the sputtering gas during growth of ZnO:Al films causes additional growth directions apart from usual c-axis and influences the vibrational lattice properties significantly, hinting a change in point defect concentration.

By means of EDX measurements, it could be verified that nitrogen is actually incorporated into the lattice causing most likely acceptor states that decrease both, carrier concentration and mobility, substantially. Furthermore, nitrogen causes a broad absorption band in vicinity of the fundamental absorption edge. Its position implies that the incorporated nitrogen forms a deep acceptor band rather than a shallow.

Due to the occurrence of such a pronounced absorption band, it can be concluded that nitrogen related defects are not responsible for the strong electrical degradation of ZnO:Al layers when annealed without protective capping layer in nitrogen atmosphere since those layers are highly transparent.

3.4 Influence of hydrogen on electrical properties and sub-band gap absorption

Originating from the solid phase crystallisation process of a-Si on ZnO:Al for thin film solar cells [65], the standard capping material for the annealing procedure under a protective layer has been hydrogenated amorphous silicon, so far. The incorporated hydrogen is assumed to cause the significant increase in mobility after cap annealing. Ponomarev *et al.* [89] ascribes it to a diffusion of H from the a-Si:H cap towards the ZnO:Al layer, passivating grain boundary defects.

In order to study the influence of hydrogen on the ZnO:Al used in this work, ZnO:Al layers have been grown in hydrogen containing atmosphere and their electrical and optical properties have been analysed. Furthermore, cap annealing using hydrogen-rich and hydrogen-poor cap material have been carried out to investigate the influence of hydrogen during the used standard cap annealing process.

Hydrogen is known to have a major impact on the electrical properties of ZnO. While hydrogen possesses amphoteric behaviour in other semiconductors, counteracting prevailing conductivity [11, 129], it increases conductivity when ZnO is deposited [130–133] or annealed under H₂ containing atmosphere [134, 135].

Residual hydrogen in deposition chambers is expected to be the cause for native n-type conductivity of ZnO [11]. Multiple studies signify that neither intrinsic donor, oxygen vacancy nor zinc interstitial, due to their deep energy level and high formation energy, respectively, are able to contribute significantly to native n-type conductivity [8, 9, 136, 137].

3.4.1 Addition of hydrogen to the deposition process

In contrast to the other investigated impurity gas series, the ZnO:Al layers of the hydrogen series have been deposited at 100 °C. A higher temperature caused roughened surfaces for all used hydrogen to argon ratios of the sputtering gas. For 100 °C it was possible to reproduce the increase of carrier concentration with increasing hydrogen as reported in literature [131, 138–140].

Next to the determination of the carrier concentration n and mobility μ , the Urbach energy E_U of the respective layers has been extracted according to eq. 2.42. The results for n , μ and E_U are given in figure 3.46 for the as deposited state of the samples and after a short and long annealing treatment at 250 °C for 1.5 hours and 50 hours, respectively, without cap in air and under atmospheric pressure.

An increase of the hydrogen content in the sputtering gas up to 5 % leads to an increase in carrier concentration of the deposited ZnO:Al film, indicating either that hydrogen is incorporated and acts as a shallow donor [11, 136] or affects n indirectly by activation of Al dopants or passivation of acceptors. A further raise of the hydrogen concentration does not result in a further improvement of the carrier concentration which saturates around $5.4 \cdot 10^{20} \text{ cm}^{-3}$.

3 Change of physical properties of ZnO:Al thin films after thermal treatments

The corresponding behaviour of the electron mobility is rather inconclusive and will be discussed separately at the end of this subsection.

As it can be seen in part c) of figure 3.46, hydrogen has an instant impact on the absorption band tailing and a decrease of Urbach energy with hydrogen flow is observed down to a saturation level around 100 meV. It can be assumed that hydrogen is able to passivate absorption tail-causing defects.

For further investigations, annealing experiments have been carried out in order to remove hydrogen from the ZnO lattice.

Annealing of bare ZnO layers at 250 °C for 90 minutes increases the carrier concentration n of the undoped reference sample slightly but decreases for any sample doped with hydrogen. However, even after annealing n remains on a high level above the value for the undoped layer. This result indicates a partial but not full effusion of hydrogen that was incorporated during deposition.

The release of hydrogen from the passivated Urbach-tail-causing defect states results in an enhancement of the Urbach energy as it can be seen in figure 3.46 b).

In order to support this assumption, the initially chosen treatment time of 1.5 hours was extended to 50 hours. The carrier concentration of initially hydrogen doped ZnO:Al films is within small fluctuations comparable to the layer not intentionally doped with hydrogen after such a long treatment. As expected, the Urbach energy of all samples is significantly increased and seems to be nearly independent of the initial hydrogen content of the films.

The determination of the molecular structure of hydrogen in ZnO and, hence, the identifi-

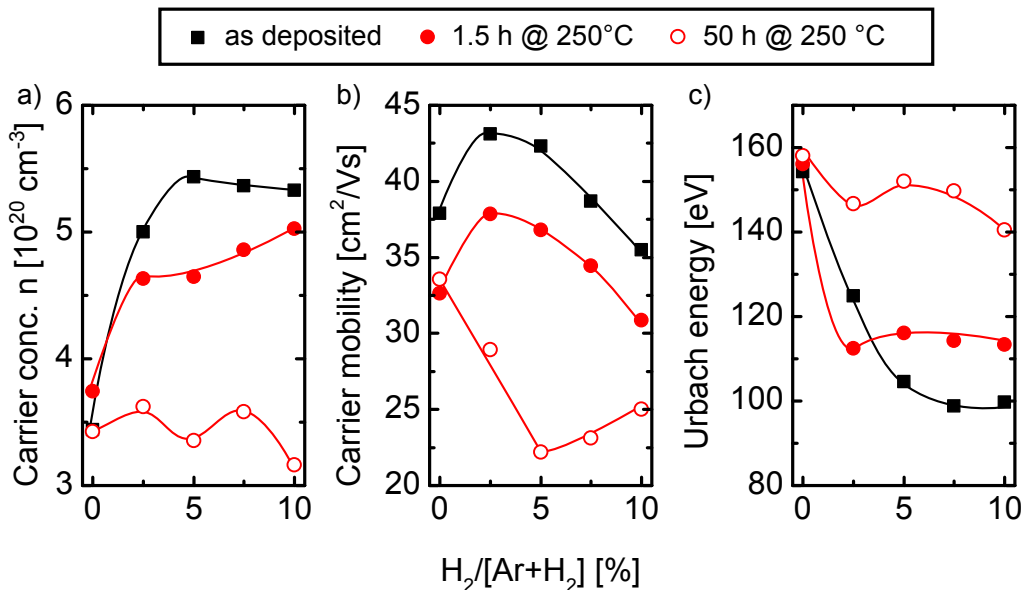


Figure 3.46: a) Carrier concentration, b) carrier mobility and c) Urbach energy as function of hydrogen to argon ratio in the sputter atmosphere for ZnO:Al films in their as deposited and thermally treated state; The included lines are guides to the eye.

cation of the hydrogen passivated defect that is partially causing Urbach tails is not trivial. The binding behaviour of H in ZnO is very versatile [141]. So far, it was found that H in solids can form chemical bonds with up to three other atoms or may be bound in clusters [136]. The main positions H can occupy in ZnO are at interstitial sites (H_i), bound to Zn in oxygen vacancies (H_O) [136] or bound to oxygen in Zn vacancies ($V_{Zn}H_2$) [142], creating complexes with other impurities such as extrinsic dopants or at dangling bonds, preferably at grain boundaries. H_i and H_O act as shallow donors [11, 136], while H at V_{Zn} passivates the doubly charged acceptors by the formation of O-H bonds. All these kinds of defects have different formation energies and differ in required energy for dissociation.

Theory and experiment have shown that hydrogen removal in single crystal ZnO at temperatures below 500 °C is mainly caused by out-diffusion of H_i [136, 143, 144]. However, considering polycrystalline material, it can be assumed that hydrogen is also released from dangling bonds at grain boundaries since they act as very efficient diffusion channels.

By means of the carried out experiments it is difficult to draw a conclusion about the kind of defect that causes absorption below the band edge and which can be passivated by hydrogen incorporation.

Due to the indecisive behaviour of the carrier mobility of ZnO:Al samples deposited under variable amount of hydrogen in the sputtering atmosphere, it is difficult to distinguish the different hydrogen incorporation possibilities and their effect on the electronic transport.

If the observed increase in carrier concentration is only caused by incorporation of hydrogen as a donor, the carrier mobility should actually decrease due to enhanced ionised impurity scattering. Furthermore, it has to be considered that the hydrogen experiments, carried out in this work, have been performed with a highly Al-doped ZnO. It is assumed that hydrogen in the deposition atmosphere enhances the doping efficiency by destabilising Al_2O_3 formation at the surface during growth [131]. However, explaining the increase in carrier concentration by a higher activation level of the incorporated Al is still contradicting the increase in mobility.

The enhancement of the carrier mobility would be feasible if the dominant activity of H is the passivation of acceptors, like zinc vacancies or dangling bonds. The not pronounced increase of μ for higher hydrogen dilution of the sputtering gas may be due to disturbance in crystalline growth [131]. The latter is caused by a decrease of scattering cross section in the sputtering gas and, hence, an increased ion bombardment on the growing layer.

However, the partly disproportionate decrease of mobility upon annealing in case of the not intentionally hydrogen doped sample indicates that even for a low treatment temperature, the effect of hydrogen removal is superimposed by another effect. The latter may be the attenuated form of the degradation process.

3 Change of physical properties of ZnO:Al thin films after thermal treatments

Table 3.1: Overview of the used capping layer materials and their respective thickness and deposition technique; The particularities of the individual deposition methods are described in section 2.2.1.2. Sample series marked with an asterisk contain a sample with larger deviation in thickness. The concerning samples are marked in figure 3.47.

cap material	thickness [nm]	deposition technique
a-Si	50±10	PECVD
a-Si	50±10*	e-beam evaporation @ 300 °C
a-Si	100±10*	e-beam evaporation @ 300 °C

3.4.2 Employing hydrogen-rich and hydrogen-poor cap materials

In order to clarify the impact of hydrogen in the cap material, the standard cap annealing treatment has been carried out using amorphous silicon differing in hydrogen content of the precursors used for deposition. While the standard PECVD process was employed to obtain hydrogen-rich a-Si:H layer, essentially hydrogen-free layers were deposited using electron beam evaporation.

Table 3.1 provides an overview of the used materials and their thickness. The results in

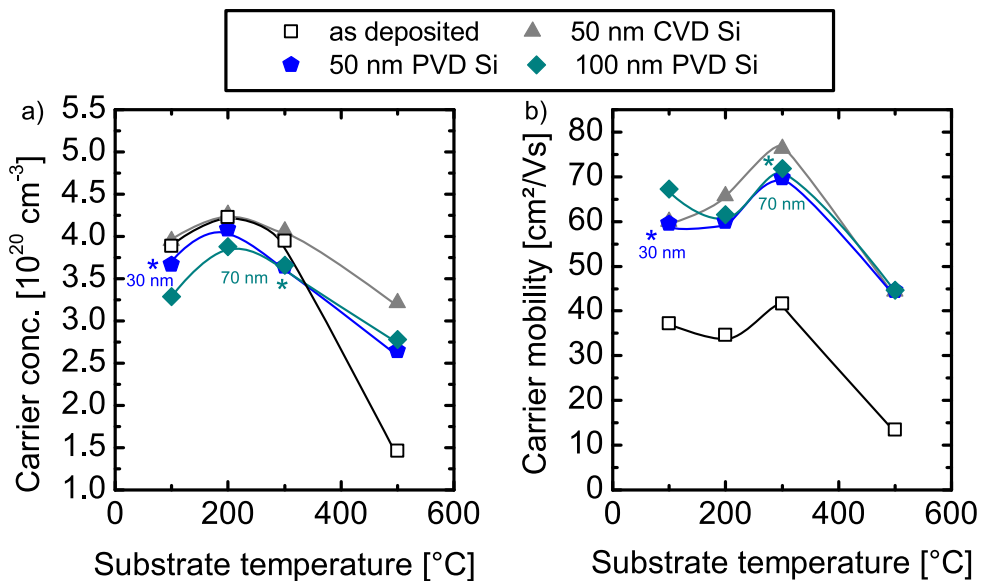


Figure 3.47: a) Electron concentration and b) carrier mobility of ZnO:Al as function of substrate temperature during deposition in their as deposited state and after cap annealing with hydrogen-rich (CVD) and hydrogen-poor (e-beam, PVD) silicon as cap material; The thickness of the capping layer given in the legend is the desired value for deposition. The real thicknesses deviate at around 10 nm, except for the samples assigned with an asterisk. For them, the cap thicknesses are given at the respective data points.

section 3.1 show strong dependence of the annealing process related changes in electrical transport properties on the deposition temperature of the ZnO:Al thin film. Therefore, cap annealing with different capping materials have been applied to ZnO:Al layers deposited in the range of 100 °C and 500 °C. All samples have been treated as described in section 2.2.1.3 in an oven at 650 °C for 24 hours under nitrogen flow and atmospheric pressure.

The results of the Hall measurements are shown in figure 3.47. The application of a 50 nm a-Si capping layer represents a repetition of the experiment described in section 3.1 and is consistent with the previous results.

Regarding the employment of electron beam evaporated (e-beam) a-Si, it is observable that the layer thickness has no major influence on the capping effect. Just for the very thin layer, a slight difference might be recognisable. Comparing hydrogen-rich and hydrogen-free material, the carrier mobility after cap annealing is enhanced almost to the same extent. No influence of the deposition temperature and, hence, structure (see sec. 3.1) of the material can be observed. A similar result was obtained by Wimmer *et al.* [145] who investigated the annealing behaviour of hydrogen containing and hydrogen-free silicon capping layers in dependence of the treatment time up to 24 hours and annealing temperature between 500 °C and 650 °C. He, as well, could show that there are no differences in electrical properties after cap annealing depending on the hydrogen content of the cap material. Hence, it can be concluded that impact of H during annealing is only marginal.

As it can be seen in fig. 3.48, the hydrogen content in the cap material does not have any influence on the Urbach energy.

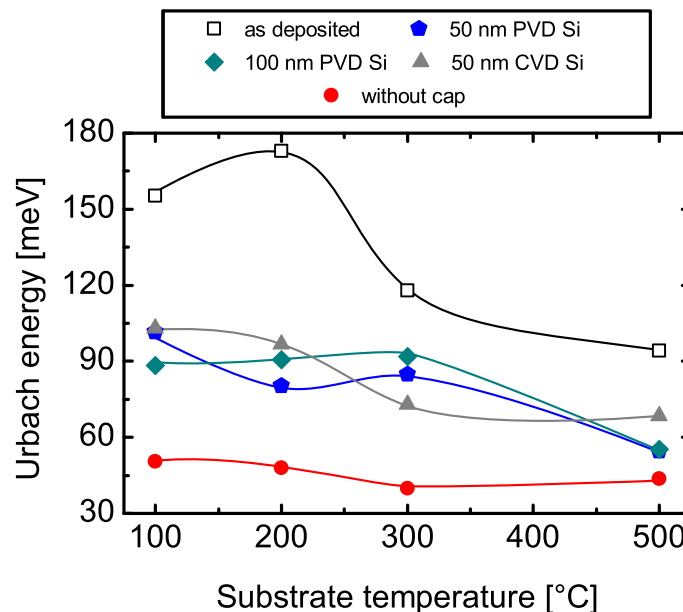


Figure 3.48: Urbach energy E_U as function of substrate temperature after cap annealing using various cap materials

3 Change of physical properties of ZnO:Al thin films after thermal treatments

3.4.3 Summary

For sputtered ZnO:Al it is not possible to attribute the significant improvement of electrical properties after cap annealing solely to hydrogen diffusion from the cap material, as was done for low pressure chemical vapour deposited ZnO by Ponomarev *et al.* [89]. It was shown that the carrier concentration becomes larger and the Urbach tails narrower for increasing hydrogen content in the sputtering gas. Driving out the hydrogen broadens the absorption tails again.

Furthermore, no significant difference in annealing behaviour could be observed regarding the electrical properties and sub-band gap absorption using hydrogen-rich and essentially hydrogen-free a-Si as cap material.

Hence, hydrogen can be excluded as main driver for material changes related to cap annealing.

3.5 Multi-step annealing

Previous investigations showed that the implementation of ZnO in solid phase crystallised poly-Si solar cell absorber results in a lower efficiency than reference cells without ZnO [146]. Furthermore, during the integration process of cap annealed ZnO:Al in a-Si/ μc tandem solar cells it was observed that a short dip of the ZnO layer in HCl is required to obtain a good solar cell efficiency [118]. Both findings suggest that during the procedure of cap annealing changes take place at the Si/ZnO interface, as well. Wimmer *et al.* [78, 119] investigated the buried interface between silicon and ZnO:Al and found evidence for the creation of a very thin SiO_x layer. An oxidation of silicon would accordingly cause a chemical reduction of ZnO:Al and could probably have a major impact on the resulting electrical properties of the ZnO layer.

If a reduction of ZnO:Al takes place during cap annealing due to formation of SiO_x at the interface, than this SiO_x would be removed during the de-capping process. Hence, the comparison of the application of multiple cap annealings without and with intermediate cap removal and renewal would provide information about the impact of such a reduced ZnO:Al/ SiO_x interface layer.

For the experiment, two sets of identically deposited ZnO:Al films have been prepared¹². One set of samples has been heated up, hold for 24 hours at 650 °C and cooled down successively for five times while for the other set de-capping and a-Si:H deposition was carried out after each cooling.

Furthermore, multi-step annealing has been performed consisting of alternating application of cap annealing and degradation in order to investigate the reversibility of the degradation process. Out of different variations in sequence of degradation and cap annealing the results of four sets of samples were remarkable and will be presented and discussed in the following. All investigated ZnO:Al films of these series have been prepared with the standard sputter conditions described in section 2.2.1.1 at 300 °C and with a thickness of 680 ± 15 nm.

After the third annealing process, independent of the kind of treatment, all ZnO:Al layers exhibited microscopic cracks. Since Hall- and four-point-probe measurements, consequently, can not be applied the analysis of the thin films has been restricted to their optical properties.

3.5.1 Repeated annealing under an amorphous silicon capping layer with and without intermediate cap renewal

Figure 3.49 shows the absorption coefficient α of the two sets of samples repeatedly treated with cap annealing but differing in intermediate cap renewal. The black curve belongs to the as deposited ZnO:Al layer while the blue ones show α after multiple cap annealing.

¹²All layers have a thickness of 670 ± 20 nm. Deposition conditions have been chosen according to the layers of the temperature series with a substrate temperature of 300 °C, see sec. 2.2.1.1.

3 Change of physical properties of ZnO:Al thin films after thermal treatments

The shade of blue increases for higher numbers of applied cap annealings while the exact numbers are given at the corresponding curves.

In case of multiple cap annealings without intermediate cap renewal (fig. 3.49 a)), no major change in absorption behaviour can be observed after application of more than one cap annealing step. However, a subsequent minor shift in band gap position towards lower energies and, as far as correctly determinable, a small decrease in sub-band gap absorption between 1 eV and 3 eV is visible for an increasing number of cap annealings. Especially the slight decrease in band gap, implying a weakly decreased carrier concentration, with any further cap annealing indicates a minor decline in its protection efficiency.

When this protective capping layer is renewed between two cap annealing steps the absorption behaviour of the treated ZnO:Al films change significantly. This can be seen in figure 3.49 b). Here, the black curve belongs to the as deposited state again while the blue ones correspond to the treated samples.

It is interesting to note that the application of two cap annealings with intermediate cap renewal leads to a tremendous increase of absorption over the entire spectral range between band gap in the blue and free carrier absorption in the near infrared. A third cap annealing enhances this absorption even more while not significantly changing the position of the band gap. Only the application of a fourth and fifth cap annealing decreases the carrier concentration considerably, observable by a strongly decreased free carrier absorption and

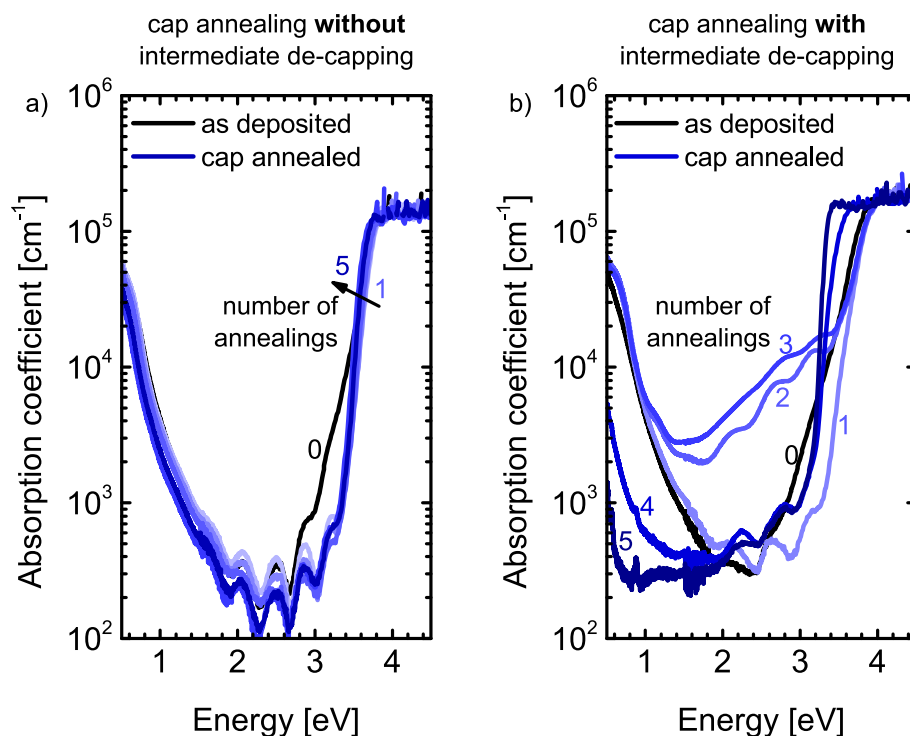


Figure 3.49: Absorption coefficient of ZnO:Al thin films repeatedly thermally treated a) without and b) with intermediate de-capping; The number of applied annealing steps is given at the respective graphs in the corresponding colours.

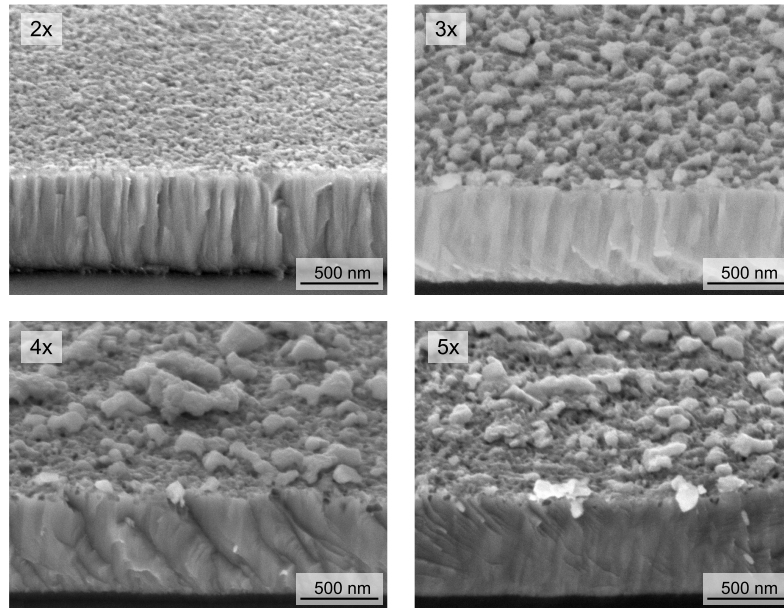


Figure 3.50: SEM cross section and surface micrographs of ZnO:Al layers subsequently treated with multiple cap annealings but intermediate cap removal; The number of applied annealing steps is given at the respective image.

shift in band gap. The samples cap annealed at least three times possess an increased surface roughness as it can be seen in figure 3.50. It indicates that a surface altering process takes place during annealing which very likely influences the etching behaviour of the layers regarding the cap removal.

Since ZnO layers deposited under Zn-rich conditions are known for their brownish colour [147], the origin of the broadly enhanced absorption within the band gap might be the creation of Zn-rich areas by reduction of the oxygen concentration within the ZnO layers.

As already mentioned, Bär *et al.* [119] found that oxygen migrates towards the Si/ZnO:Al interface when ZnO:Al is thermally treated under an a-Si layer, forming silicon oxide there. This thin oxide layer would, here, be removed with every de-capping process. With each further cap annealing, the oxygen in the ZnO:Al film gets, therefore, consumed, leaving behind Zn rich areas. These areas would presumably be located especially in areas close to the surface.

It was possible to remove the appearing brownish colour of the film by a short dip of the samples into a 0.1 % solution of hydrochloric acid (HCl). With this dip, approximately 20 nm of ZnO material has been removed, supporting the assumption that cap annealing treatments alter especially interface close regions of the ZnO:Al film.

The strong deterioration of the carrier concentration of the ZnO:Al films after the fourth and fifth treatment may be explained by the surface roughness after the third cap annealing. It is quite likely that the applied 50 nm a-Si capping layer does not completely cover the entire

3 Change of physical properties of ZnO:Al thin films after thermal treatments

surface and, therefore, the ZnO:Al is partially exposed to the annealing atmosphere. Hence, the properties of these films are comparable to those after the application of annealing without cap.

3.5.2 Alternating application of degradation and cap annealing

Figure 3.51 shows the absorption coefficient α of ZnO:Al films alternately treated for at least three times with the degradation and cap annealing process. For the set of samples shown in part a) of the figure, the treatment series started with degradation, in the case depicted in part b) with cap annealing. Generally, both sequences lead to a very similar trend of absorption. From the energetic position of the band gap and the behaviour of the free carrier absorption it can be observed that application of degradation and cap annealing, independent of the samples past, always lead to a decrease and increase, respectively, of the carrier concentration.

Figure 3.52 shows band gap energies extracted via equation 2.42 of all samples in detail. Those films finally treated with a degradation step possess the same band gap energy of 3.3 eV independent of the preceding treatments. However, the band gap energy of samples finally treated with cap annealing depends on the number of annealings before.

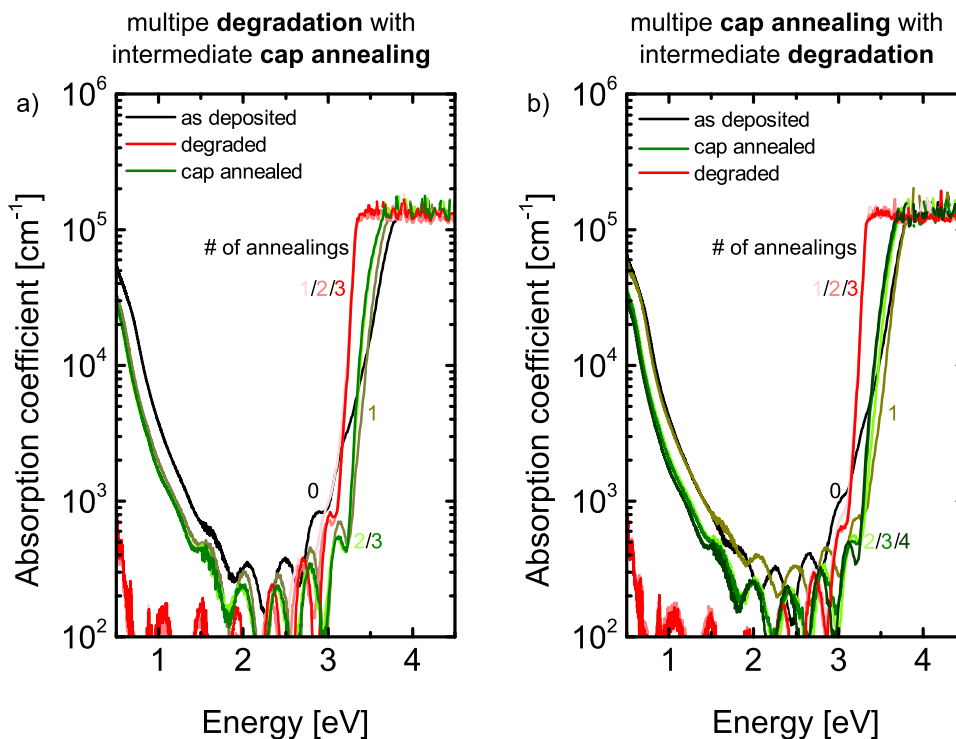


Figure 3.51: Absorption coefficient of ZnO:Al thin films a) repeatedly degraded with intermediate cap annealing and b) repeatedly cap annealed with intermediate degradation; The number of applied annealing steps is given at the respective graphs in the corresponding colours.

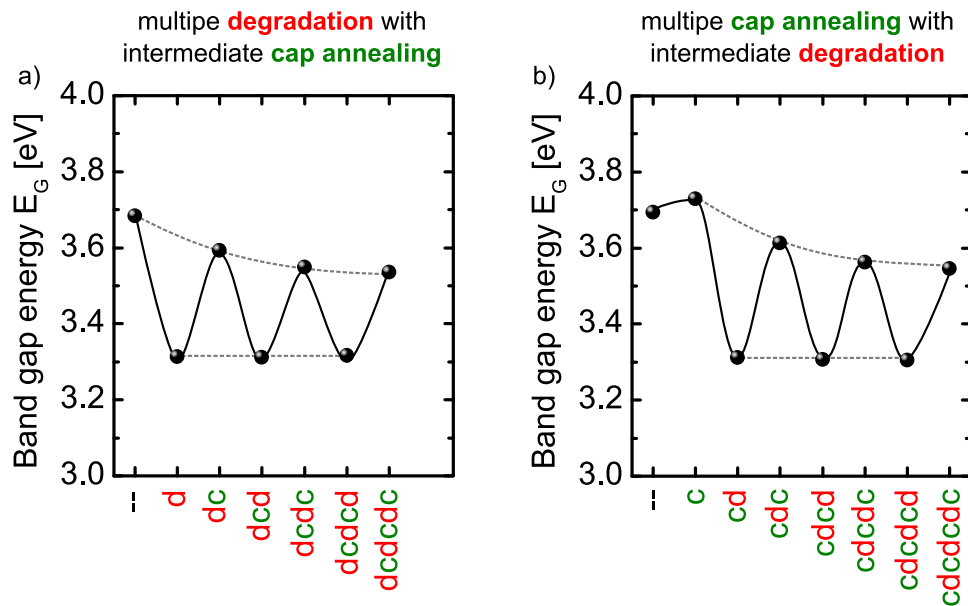


Figure 3.52: Band gap energy obtained from ZnO:Al films that got alternately and subsequently thermally treated starting with a) degradation and b) with cap annealing

For both initial conditions, after each degradation step the band gap energy and, therefore, the carrier concentration can never be restored completely with a cap annealing. It indicates that the degradation process of ZnO by annealing without cap consists of two mechanisms, one recoverable by cap annealing and an irreversible one.

For these two sets of samples, the width of the absorption tails (Urbach energy E_U , according to eq. 2.42) has been calculated and plotted in figure 3.53. Part a) shows the results for the treatment series starting with degradation, b) starting with cap annealing. It has to be noted that the fit of the Urbach tail has to fulfill certain requirements and there is a lower limitation to the determinable Urbach energy. This issue is discussed in detail in appendix B. The data points given here in red do not satisfy those conditions and have to be regarded with special care. Furthermore, the fits attained for the multi-step annealed samples finally treated with cap annealing have been close to that limitation given in appendix B. Hence, only the general statement can be made that, as seen in the previous sections of this work, both, degradation and cap annealing reduce the sub-band gap absorption in vicinity of the band gap energy significantly with respect to the as deposited state, resulting in lower Urbach energies.

The oscillations at a very low level of E_U depending on the final treatment are probably due to a minor dependence of the Urbach energy on the width of the error function used in the fit (see section 3.1, eq. 2.42 and appendix B).

Comparing the figures 3.52 and 3.53 the assumption of a correlation between the optical band gap energy or carrier concentration, respectively, and the Urbach energy is obvious.

3 Change of physical properties of ZnO:Al thin films after thermal treatments

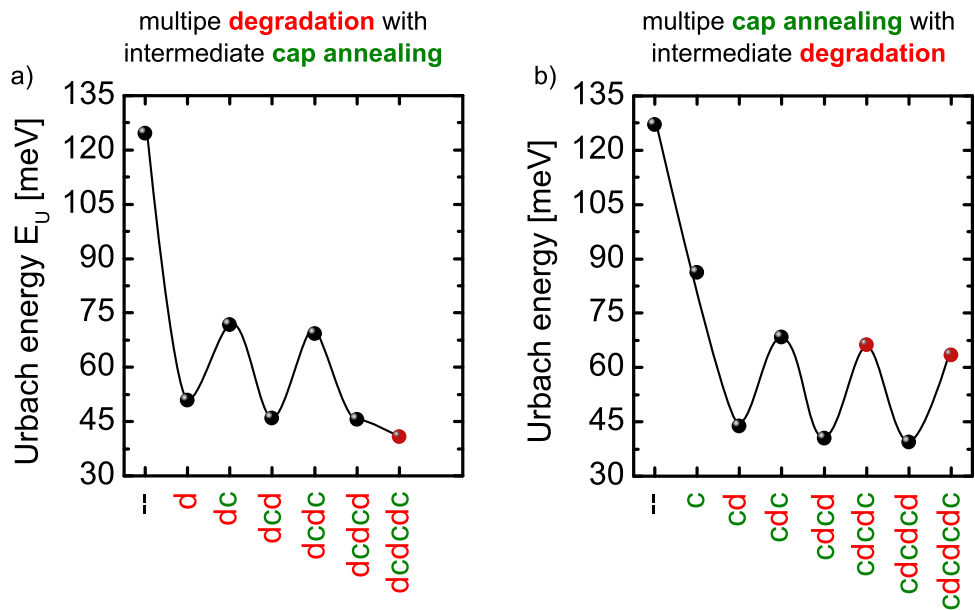


Figure 3.53: Urbach energy obtained from ZnO:Al films that got alternately and subsequently thermally treated starting with a) degradation and b) with cap annealing

However, no direct relationship of the carrier concentration, neither with the Urbach energy nor the width of the error function in the fit could be observed when analysing the complete set of samples investigated in this thesis.

3.5.3 Summary

Multiple cap annealings with and without intermediate a-Si cap renewal result in very different optical properties of ZnO:Al. Without cap renewal, multiple application of cap annealing more than once do not have a significant impact but decreases the band gap energy slightly. Intermediate removal and deposition of a new capping layer after each cap annealing step, however, causes pronounced sub-band gap absorption and an alteration of the ZnO:Al surface.

This result indicates that the capping layer affects the ZnO in two different ways. Firstly, it protects the ZnO from interacting with the atmosphere, preventing a severe degradation of the electrical properties. Secondly, the a-Si cap itself is able to interact with the ZnO film and acts most likely as an oxygen sink, creating SiO_2 at the interface and causing an enrichment of Zn in interface-close regions.

The alternating application of degradation and cap annealing leads to an oscillation of the band gap energy E_G , where E_G is always reduced to 3.3 eV and recovered by cap annealing, but never to the previous value. Hence, it confirms the assumption that the degradation

3.5 Multi-step annealing

mechanism consist of an irreversible and a by cap annealing reversible process. The at same time observable oscillation of Urbach energy cannot be fully explained based on the present experiments. It hints, however, that for low Urbach energies a minor influence of the Fermi energy is existent.

3.6 Summary of experimental results regarding electronic transport and sub-band gap absorption

Electrical transport

Both considered annealing procedures, with and without capping layer, influence the defect equilibrium of the treated ZnO:Al by affecting donor and acceptor concentrations in different ways. Cap annealing of bare films significantly improves the electrical transport, mainly by annihilating present intrinsic acceptors. Annealing without cap on the other side, deteriorates the material's electrical properties.

It can be expected that an interaction with the annealing atmosphere, in this case with nitrogen and residual oxygen, or the protection from it, provides the key for an explanation of mechanisms leading to such contrasting behaviour.

When provided during film growth, it was shown that both elements easily reduce both, carrier concentration and mobility. However, nitrogen could be excluded as cause for the observed strong degradation of electrical properties attributed to annealing without cap. The main reason for this exclusion is the strong colouring of the films accompanied with the incorporation of nitrogen in ZnO, which is not observed for ZnO:Al annealed without cap. Furthermore, it could be shown that once nitrogen is incorporated it is not completely removable anymore under the treatment conditions investigated here.

Considering annealing under a protective a-Si:H capping layer, it was supposed that passivation of defects or creation of donor states by hydrogen is able to explain the enormous improvement of electrical properties. This could be disproved because even high amounts of hydrogen incorporated during growth do not explain the tremendous change in electrical characteristics of cap annealed and 2 step annealed ZnO:Al layers.

Therefore, it is quite likely that the observed effects can be mainly attributed to the presence or absence of oxygen in the annealing ambience. Specific oxygen related mechanisms will be addressed in the ensuing discussion.

Sub-band gap absorption

It was found that the annealing temperature has a major impact on the optical properties in the vicinity of the fundamental absorption edge of ZnO:Al. To obtain absorption tails with Urbach energies far below 100 meV at least 400 °C treatment or substrate temperature during deposition are required. The reduction of the tail absorption is not directly related to the electrical properties of the corresponding layer, since very narrow tails are observable for, both, electrically very poor and very good material. The origin of these absorption tails is discussed separately in the following section.

4 Discussion

4.1 Impurity related mechanisms during thermal annealing and the influence of the prevailing oxygen partial pressure

Thermal post-deposition procedures influence the treated material not just by supply of thermal energy but by a possible interaction with the treatment atmosphere, as well. Whether the atmosphere affects the properties of the ZnO layer positively or negatively primarily depends on its chemical composition and the field of application of the treated layers.

The mainly investigated treatment atmospheres for ZnO thin films are vacuum, air, nitrogen or hydrogen. A treatment of bare ZnO layers of inferior electrical properties primarily leads to qualitative improvements in case of a treatment in vacuum [73, 148, 149] and hydrogen [72] or to deterioration for oxygen and nitrogen containing ambients [66, 75, 77, 150].

Annealing in the same temperature regime under a protective capping layer, on the other side, yields significantly improved electrical properties [74, 89], even for treatment atmospheres with O₂ and N₂.

Disregarding the specific deposition and annealing conditions, the capping layer has two effects. It acts as **protection layer** and diminishes the influence from the atmosphere considerably. Furthermore, the cap itself may **interact with the ZnO layer**, affecting chemical and physical processes within the treated material.

The results of annealing experiments in the past indicated a strong influence of O₂ and N₂ on the electrical degradation process during annealing without cap. Both elements are able to easily form acceptor states in ZnO resulting in compensation of active donors and enhanced ionised impurity scattering that reduces the electron mobility.

As explained earlier, but for completeness sake repeated, N₂ can be excluded as possible main factor. It could be shown that incorporation of N₂ during film growth, sufficient to induce such a strong electrical degradation observed after annealing without cap in N₂ atmosphere, yield highly coloured ZnO:Al layers. ZnO films deposited with pure Ar and annealed in N₂, however, are characterised by a high transparency.

Hence, it can be assumed that the impact of thermal post-deposition procedures is primarily dependent on the oxygen partial pressure during the treatment. Atmospheres like air or with residual oxygen contaminated nitrogen can be expressed as ambients with high oxygen

4 Discussion

partial pressure. Vacuum treatments and annealing under a silicon capping layer on the other side, are characterised by a very low oxygen partial pressure.

Earlier studies by Ruske *et al.* [66] and Wimmer *et al.* [79] showed that the degree of degradation after annealing without cap depends on the treatment duration and applied temperature. The electrical deterioration is pronounced for either longer treatment times at constant plateau temperatures or for higher treatment temperatures at constant durations. Both results speak for a diffusion-driven process.

In case of cap annealing, a similar trend has been observed. Here, a direct correlation between increase of carrier concentration and mobility with raise of treatment temperature up to 650 °C at constant annealing time has been found.

The influence of the temperature is primarily related to the activation of diffusion processes. Since it could be shown that no recrystallisation of ZnO occurs during, both, annealing with and without cap, the chosen temperature regime between 550 °C and 650 °C provides, at the most, activation energy for healing of minor structural defects.

Annealing under high oxygen partial pressure

Assuming now that O₂ diffusion is the main driver for electrical changes during annealing processes, similarities should be found between ZnO:Al already deposited under O₂ containing atmosphere and ZnO:Al deposited without additional O₂ but annealed under high O₂ partial pressure, i.e. with residual oxygen in the annealing ambience.

Figure 4.1 shows the carrier mobility as function of carrier concentration of those ZnO:Al layers with varied oxygen supply during growth.

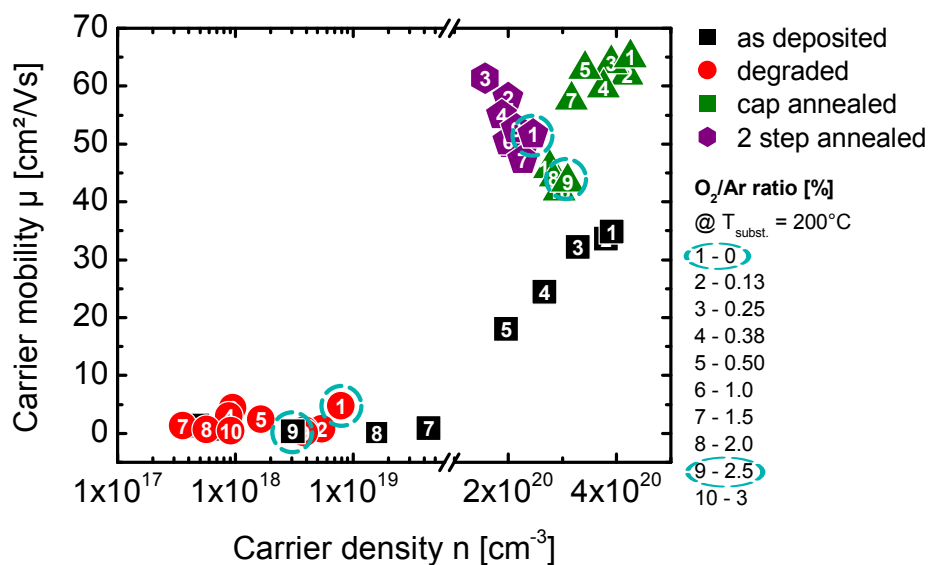


Figure 4.1: Carrier mobility as function of carrier concentration for the samples of the oxygen series

4.1 Impurity related mechanisms during thermal annealing

The ZnO:Al layers deposited between 2 % and 2.5 % oxygen in the sputter gas possess comparable electrical properties as degraded films without additional O₂ (see data points 1 and 9). Furthermore, samples already deposited under very oxygen-rich conditions seem to experience no further degradation upon annealing without cap. Additionally, it is interesting to note that cap annealing of ZnO:Al with at least 2 % oxygen in the sputtering gas results in very similar electrical properties as 2 step annealed ZnO:Al deposited at the same temperature but without additional oxygen. All this is further evidence for an incorporation of residual oxygen from the atmosphere during the 24 hours annealing without cap as a major cause of the observable degradation of electrical properties attributed to this treatment. Possible oxygen related specific mechanisms behind the loss of carriers and mobility during annealing without cap are

- the deactivation of Al³⁺ dopants or
- the compensation of donors by creation of acceptor-like intrinsic defects.

Deactivation of Al as donor may occur by forming AlO_x phases or neutral defect complexes involving Al³⁺ and intrinsic acceptors like zinc vacancies (V_{Zn}²⁻) or oxygen interstitials (O_i²⁻). Present intrinsic acceptors can act, additionally, as electron traps and, therefore, compensate active donors.

Due to the observed strongly reduced mobility, however, the formation of AlO_x and neutral complexes seems rather unlikely. Furthermore, the binding strength of the Al-O bonds is about three times larger than that of Zn-O bonds [75]. Since an almost complete recovery of the carrier concentration is obtained by applying cap annealing on degraded ZnO:Al, an activation of Al from relatively stable AlO_x phases appears also improbable.

However, the observation of a non-reversible deactivation of carriers in the context of multi-step annealing could be related to the formation of AlO_x or Al related neutral defect complexes.

The enormous decline in mobility induced by annealing without cap is rather explainable with the creation of acceptors and their pronounced impact on electron scattering. The formation of both intrinsic acceptors, V_{Zn}²⁻ and O_i²⁻, is highly benefited by increased oxygen partial pressure [151].

Additionally, the influence of grain boundaries has to be taken into consideration at the low level of carrier concentration observed for degraded ZnO:Al. It can be expected that the decreased mobility is a consequence of increased grain boundary scattering, as well.

Annealing under low oxygen partial pressure

Annealing of ZnO:Al with a protective cover layer effectively creates a treatment environment with very low oxygen partial pressure.

Possible reasons for the tremendous increase in mobility, although not to the same impact, are

- elimination of compensating acceptors and
- passivation of acceptors by hydrogen.

4 Discussion

According to first-principle calculations of formation energies of defects by Lany and Zunger [151] the compensation can be expected to be dominated by V_{Zn}^{2-} . Hence, annealing under a protective cap, i.e. with very low oxygen partial pressure, appears to be able to annihilate these acceptors.

Additionally, annealing under a silicon cap results in migration of oxygen to the Si/ZnO interface, as earlier works showed [78, 119]. Silicon, so to speak, acts as a sink for oxygen. Zn that becomes available would fill V_{Zn}^{2-} and enhance both carrier concentration and mobility. The forming SiO_2 at the interface, however, may act as a barrier preventing further changes in the ZnO:Al in case of multiple cap annealing steps with the same cap.

Further evidence for this assumption is given by the experiment of cap renewal between multiple cap annealings, which most likely causes oxygen depleted regions near the ZnO/Si interface and considerable Zn enrichment, as well.

The origin of the calculated accompanied slight decrease in donor concentration is highly speculative. The most plausible reason would be the local formation of AlO_x or neutral defect complexes as in case of annealing without cap.

Influence of hydrogen

When carried out at sufficiently low temperatures ($\ll 500$ °C), annealing in hydrogen is able to decrease the resistivity of ZnO thin films by either passivating existing acceptor-like defects or acting as shallow donor [72, 77, 144].

In this work, however, the only important hydrogen source is the hydrogenated amorphous silicon layer during cap annealing. The annealing process is carried out at a temperature of 650 °C. Since hydrogen is nearly completely removed for treatment temperatures above 500 °C [143, 144], it does not play more than a subordinate role in the cap annealing process. This assumption can be confirmed by Hüpkes *et al.* [152] performing SIMS¹³ measurements of ZnO:Al layers before and after annealing with deuterated amorphous silicon (a-Si:D) capping layers. They could show that after a 24 hour annealing process at 650 °C almost all deuterium diffused from the capping layer but no detectable amount could be found in the treated ZnO:Al film.

Conclusion

Even though the analysis of the change in electrical properties during annealing is based on a rather simple model, it provides a conclusive picture of the processes occurring in ZnO:Al during annealing with and without protective capping layer in nitrogen ambient.

The resulting properties of ZnO:Al after annealing are primarily caused by competing mechanisms of oxygen incorporation and oxygen 'effusion' from the layer, influencing the donor and acceptor concentration in the material.

The equilibrium point between them depends on treatment conditions. Since it is expected that the processes are diffusion-driven, parameters like annealing temperature, duration and

¹³Secondary Ion Mass Spectroscopy

4.1 Impurity related mechanisms during thermal annealing

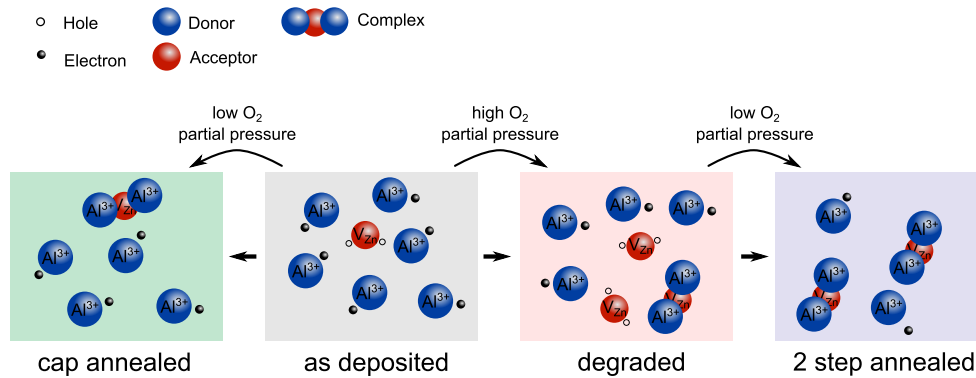


Figure 4.2: Simplified illustration of the annealing processes in terms of changes in donor and acceptor concentration in dependence of the applied oxygen partial pressure condition.

layer thickness are important for the strength of the annealing process. The oxygen partial pressure, however, represents the main influencing factor since it determines the principle characteristic of the treatment, i.e. either improvement or deterioration of the electrical properties of the treated film.

Figure 4.2 presents a illustration of the annealing processes in terms of changes in donor and acceptor concentration in dependence of the applied oxygen partial pressure condition.

As deposited films are characterised by a comparably high doping efficiency but the donors are partially compensated. This reduces the carrier concentration as compared to the Al concentration of the film and diminishes the mobility compared to the maximum obtainable mobility predicted by theory.

Cap annealing leads to a reduction of acceptor states but also to partial inactivation of donors, most likely by formation of donor-acceptor complexes. Due to the opposing charge of donors and acceptors, these complexes can have a high binding energy [153] and could explain the irreversible contribution of the annealing process.

Annealing without cap, on the other hand, creates additional acceptors which strongly diminish the carrier concentration. Most acceptors seem to be unbound, as the carrier concentration in these layers is very low and a sole attribution of low mobility to grain boundary scattering seems unlikely, although not impossible. Cap annealing of the degraded layers on the contrary (2 step annealing) lowers the acceptor concentration again and releases a large amount of carriers. As compared to only cap annealed samples, more donors are deactivated, which could again be explained by creation of more neutral or singly charged acceptor-donor complexes. As these complexes are predicted to be rather stable, this again seems to hint, that a lot of unpaired acceptors should be present in the degraded films, as the large recovery of carriers with this second annealing step would seem unlikely if all donors were deactivated by degradation.

In summary the presented picture is able to describe the observed annealing related changes in ZnO:Al within a comparatively simple scheme. In this model, the electrical transport is mainly governed by the defect equilibrium in the films, which determines the compensation ratio and, therefore, the contribution of ionised impurity scattering to the electrical trans-

4 Discussion

port. Grain boundary scattering is explicitly not ruled out, but should only play a major role for degraded films or films deposited at a high oxygen partial pressure.

4.2 The origin of the exponential absorption tails in ZnO:Al

In many semiconductors and insulators the fundamental absorption edge below the band gap energy depends exponentially on the energy of incident photons. This behaviour is known as Urbach tail since in 1953, F. Urbach suggested an empirical rule for the optical absorption coefficient α in disordered solids [51].

In this work the presented experimental series showed that the transparency of ZnO:Al suffers as well from the appearance of such absorption tails. Their development is mainly dependent on the applied temperature regime, either during deposition or post-deposition annealing, or the presence of larger quantities of hydrogen. For better understanding and development of methods to prevent such a loss of transparency knowledge about the origin of such tails is important.

During the past 60 years many attempts were undertaken to find a physical explanation of that rule for a wide range of materials [46, 54, 154–161]. Up to now, no universally valid theory was found and it remains unclear whether there is only one or several independent mechanisms giving rise to the development of exponential absorption tails.

Two important formalisms have been developed: Kane's [162] and Halperin-and-Lax's (H-L) [163] which were further developed in the following years ([164] and references therein). However, Kane's model, which represents undisturbed band and band tails with a single DOS, overestimates the tails, while the H-L model uses a separate DOS for undisturbed bands and their tails and is in acceptable agreement with the experiment [164].

From the many existing theories about the origin of absorption tails the emerging main physical reason is the creation of additional states close to the band edges due to impurities and presence of potential fluctuations, i.e. internal electric fields, in the crystal. The source of the dominant field is determined by the nature of the lattice. Considering a covalent material, charge and concentration of impurities play a major role while for ionic and polar material electric fields are also induced by lattice dynamics.

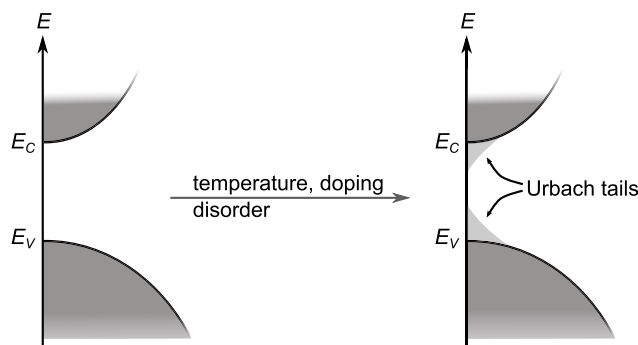


Figure 4.3: Urbach tailing scheme, according to [154]

4 Discussion

For polycrystalline material, it is very likely that structural disorder, both, at grain boundaries and in grains contribute to absorption band tailing to a great extent.

Following the considerations of Iribarren *et al.* [56, 164], all important contributions to the formation of exponential band tails with Urbach energy E_U can be represented by

$$E_U(X, n, p, T) = \underbrace{E_{U_X}(X)}_{\substack{\text{structural} \\ \text{disorder}}} + \underbrace{E_{U_D}(n)}_{\substack{\text{ionized} \\ \text{donors}}} + \underbrace{E_{U_A}(p)}_{\substack{\text{ionized} \\ \text{acceptors}}} + \underbrace{E_{U_{Ph,D}}(n)}_{\substack{\text{phonon-} \\ \text{electr.} \\ \text{interaction}}} + \underbrace{E_{U_{Ph,A}}(p)}_{\substack{\text{phonon-} \\ \text{hole} \\ \text{interaction}}}, \quad (4.1)$$

where the part of the structural disorder can be divided into contributions of bulk defects, grain boundaries (GB) and strain

$$E_{U_X}(X) = \underbrace{E_{U,\text{def}}}_{\substack{\text{bulk} \\ \text{defects}}} + \underbrace{E_{U,\text{GB}}}_{\substack{\text{GB} \\ \text{defects}}} + \underbrace{E_{U_Y}}_{\substack{\text{strain}}}. \quad (4.2)$$

X represents, here, a parameter for the structural disorder in atomic position [53], n and p the electron and hole concentration, respectively, and Y a parameter which is associated with the strain in the material and its elastic properties.

Contribution of structural disorder – grain boundaries, bulk defects and grains

Grain boundaries

Lattice defects and imperfection are always present, even in monocrystalline lattices. These distortions of a perfect crystal range from relatively localised defects, like wrong bonds and coordination, over chemical and stoichiometric defects to extended defects like voids, dislocations and grain boundaries.

These defects produce potential fluctuations and tend to be more pronounced in polycrystalline than in monocrystalline material. Hence, a greater effect on the Urbach energy is expected. The two main regions of a polycrystalline sample, grains and grain boundaries, contribute differently and the influence of grain boundaries is expected to decrease with increasing grain size of the material. Furthermore, as stated in eq. 4.2, strain in the lattice may have an influence on the development of band tails, as well.

To estimate the influence of grain boundaries, Iribarren *et al.* [164] employed a simple model consisting of spherically shaped grains surrounded by two-dimensional amorphous layers as grain boundaries. They assume the grain boundaries to have a certain carrier trap density, which are ionised and, hence, possess an electric field. As described in section 2.1.3, the trapped carriers create a potential barrier at the grain boundaries and a depletion region within the grains.

They showed that the penetration depth of the electric field F_{GB} into the surrounding grains

4.2 The origin of the exponential absorption tails in ZnO:Al

is temperature dependent and becomes larger with increasing temperature. These electric fields cause potential fluctuations by an internal Franz-Keldysh effect¹⁴ and, hence, local variations of the optical band gap.

The Urbach energy E_U is assumed to be directly related to this electric field. This assumption is confirmed by a theory established by Dow and Redfield [157]. As the average electric field $\langle F_{GB} \rangle$, induced by the grain boundaries, depends on temperature, trap concentration and grain size [164, 165], the Urbach energy is determined by these parameters, as well.

Intra-grain defects

Even if the lattice of the grain regions can be considered as essentially ordered, many localised and extended defects are present, especially if doped material is considered.

The dominant representatives of the category point defects, in case of ZnO:Al, are substitutional impurities like Al on Zn lattice positions and stoichiometric defects like vacancies or atoms lodging on interstitial sites. Depending on the deposition conditions clustering of intrinsic atoms, the development of different material phases, e.g. AlO_x or incorporation of dopants on interstitial sites, have to be regarded, as well. Especially the dominant defects may lead to localised fields according to the mentioned Franz-Keldysh effect to local deviations of the optical band gap. Furthermore, due to difference in size of the impurities compared to the constituent atoms of the lattice, a substitution or clustering at interstitial sites may result in local mechanical strain and a variation in interatomic distance. Compression of the latter leads to an increase of the electronic band gap, while a dilution yields a decrease.

Among extended intra-grain defects, dislocations are assumed to be the predominant species. Usually they occur at the edge of an extra plane of atoms causing in compressive and tensile strains and in lowering and raising, respectively, of the potential in the neighbourhood of the dislocation [60]. These potential differences, in turn, are smearing the band edges.

Strain

Strain is not only present in the surrounding of localised defects but may prevail in larger areas of the sample e.g. due to mismatch in thermal expansion between substrate and the sample's material.

¹⁴The Franz-Keldysh effect describes the change in optical absorption of a semiconductor when an electric field is applied. The electric field tilts the band edges and the states at the edges are effectively exponentially broadened into the forbidden band gap area. A valence electron, excited with energy slightly less than the band gap, is able to tunnel to the conduction band through a triangular shaped barrier whose thickness is inversely proportional to the applied field. Hence, an increase in electrical field strength enhances the tunneling probability [60, 165].

Contribution of density-of-states (DOS) band tails due to ionised impurities

The initially most reasonable assumption for absorption within the band gap are density-of-states band tails due to the presence of a sufficient amount of ionised impurities, like after heavy doping.

The kind of dopant in semiconductors is usually chosen according to their energy level close to one of the band edges in order to reduce the activation energy of conducting carriers. Due to many-body effects, those dopants do not cause a discrete energy level but split into an energy band merging, at high doping concentrations, with the valence or conduction band. The impurity band can participate in absorption processes (see figure 4.3).

Next to the dopants themselves, e.g. compensating defects create tail states at the corresponding band edge and develop a defect band if present in a sufficiently high concentration. However, the determination of DOS tails due to impurities is not trivial and their shape is not intuitively exponential.

A detailed overview of different theories about band tailing due to heavy doping is given by Van Mieghem [166]. He points out that an alteration of the band structure by doping is always attributed to many-body effects like band gap narrowing and also to a spatial random distribution of impurities locally distorting conduction and valence band, respectively. While the electron-electron interaction causes a relatively small tail, the tail caused by electron-impurity interaction reaches far into the band gap.

However, impurities do not only cause local electric fields due to their charge, their size causes localised strains (dilation or compression), as well. The resulting deformation potential increases the band gap locally in case of compressive and decreases it for tensile stress. The overall perturbation results in a smearing of both band edges and has the same effect as dislocations.

In general, all ZnO:Al films examined in this work, except of some degraded samples, possess a carrier concentration above 10^{18} cm^{-3} and can, therefore, be considered as degenerate. Since the Fermi energy is located within the conduction band, tail states at the conduction band edge are occupied and do not contribute to band-to-band absorption processes.

However, against the common view that in a degenerate n-type (p-type) material only the tail of the valence (conduction) band is probed [56, 60, 167, 168], it has to be assumed that both tails participate in photon absorption, either by *intraband* transitions or by tunneling processes. Hence, the influence of the individual tail cannot be clearly separated.

Contribution of phonon related fields

In the context of phonon related electrical fields it is important to consider that the lifetime of a phonon is much larger than that of a photon. Therefore, on the timescale of optical absorption events, displacements due to a finite temperature distribution can be considered as frozen, causing static internal electric fields. Regarding the lattice dynamics of ZnO at elevated temperature, only longitudinal optical (LO) phonons create significantly strong fields [157]. The interaction between electrons and electrical potential induced by the phonon field is called Fröhlich interaction [73]. The strength of the phonon field is

4.2 The origin of the exponential absorption tails in ZnO:Al

directly correlated to the relative displacement of the participating atoms and, therefore, strongly temperature dependent. G. D. Mahan [46] showed theoretically that Urbach's rule can be derived from Fröhlich interaction.

Furthermore, the experimentally shown strong temperature dependence of Urbach energy $E_0 = k_B T / \sigma$ [57, 169] supports a strong influence of phonons fields on absorption tails.

Temperature broadened Mahan-excitons

Regarding absorption processes in ZnO, actually excitonic rather than electronic states have to be taken into consideration. These are pairs of electrons and holes, stabilised by Coulomb attraction between them, and dominating the absorption behaviour of undoped semiconductors below the fundamental absorption edge [170]. Usually, it is assumed that for a degenerate semiconductor, these excitons eventually dissociated if the carrier concentration exceeds a critical value (excitonic Mott transition, see section 2.1.5) [47, 48, 171, 172]. However, the critical excitonic Mott density is heavily debated in literature since the existence of excitons above that critical density is predicted [46–48], the so-called *Mahan*-excitons. These Mahan excitons are able to interact with internal electric fields in a similar way as it is described for electrons above.

For example, Dow *et al.* [157] ascribed the exponential absorption edge in ionic and covalent materials to an interaction of excitons with non-uniform electric microfields, which are able to ionise the excitons. However, primarily the microfields affect the internal motion of the excitons and broadens their energy states. Furthermore, they showed that their proposed mechanism yields an exponential spectral dependence of the absorption coefficient on the photon energy.

Conclusion

To summarise, absorption tails in ZnO:Al can be caused by a direct change of the DOS within the band gap, e.g. due to intrinsic or extrinsic addition of donors and acceptors and by potential fluctuations caused by inhomogeneously distributed internal electrical microfields. The latter may have multiple origins like the fields from ionised impurities, phonon-related fields due to the polar character of the bonds and structural defects.

Based on the experiments carried out in this work, a quantitative differentiation of all contributions is hardly possible and is beyond the scope of this thesis. However, based on the obtained results the influence of various factors can, at least, be estimated.

Structural disorder

From the results of section 3.1, it can be assumed that the sub-band gap absorption is caused by extended defects to a large extent.

The observable absorption tails in ZnO:Al can be strongly diminished either by using high substrate temperatures above 400 °C during the deposition or by application of high temperature post-deposition annealings (fig. 3.14 a)). The degree of improvement after thermal

4 Discussion

annealing for temperatures applied in this work (550 and 650 °C) is highest for room temperature deposited samples and is declining for increasing deposition temperatures. No significant improvement can be obtained by annealing a sample grown at 500 °C substrate temperature.

Further clarification is provided by considering the dependence of the Urbach energy on the annealing temperature. Figure 4.4 shows the Urbach energy of ZnO:Al layers deposited at a moderate temperature of 200 °C as function of the temperature used for a subsequent annealing without cap for two hours¹⁵. Here, it can be observed that a significant reduction of absorption tails is obtained when the samples are treated at temperatures above 400 °C even for a rather short treatment time.

At these temperatures, the provided thermal energy is probably sufficient to anneal parts of those structural defects caused by a growth at low temperatures.

This assumption is further supported by the finding that the Urbach energy correlates strongly with the width of the Raman E_2^{high} mode, a measure for the crystal quality, as it can be seen in figure 4.5 a). Only the ZnO:Al layers in their as deposited states, with increasing oxygen addition during growth, present an exception in this case.

Apparently, the increase of oxygen supply during growth reduces the density of structural defects for which Raman spectroscopy is sensitive but that are not causing absorption close to the band edge.

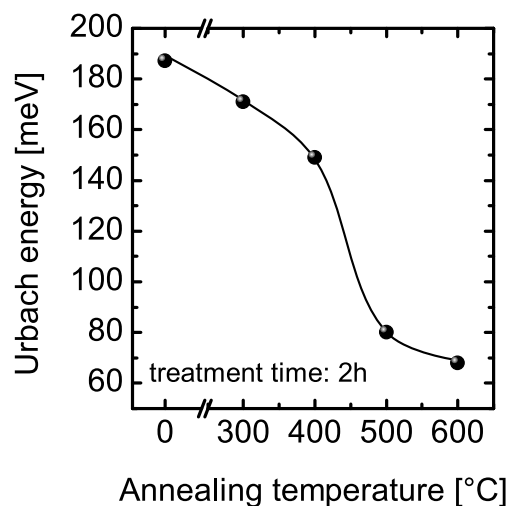


Figure 4.4: Urbach energy of ZnO:Al as function of the applied temperature during a two hour thermal annealing without cap; The layers had a thickness of 613 nm and were deposited at a substrate temperature of 200 °C.

¹⁵All other annealing conditions have been fixed.

4.2 The origin of the exponential absorption tails in ZnO:Al

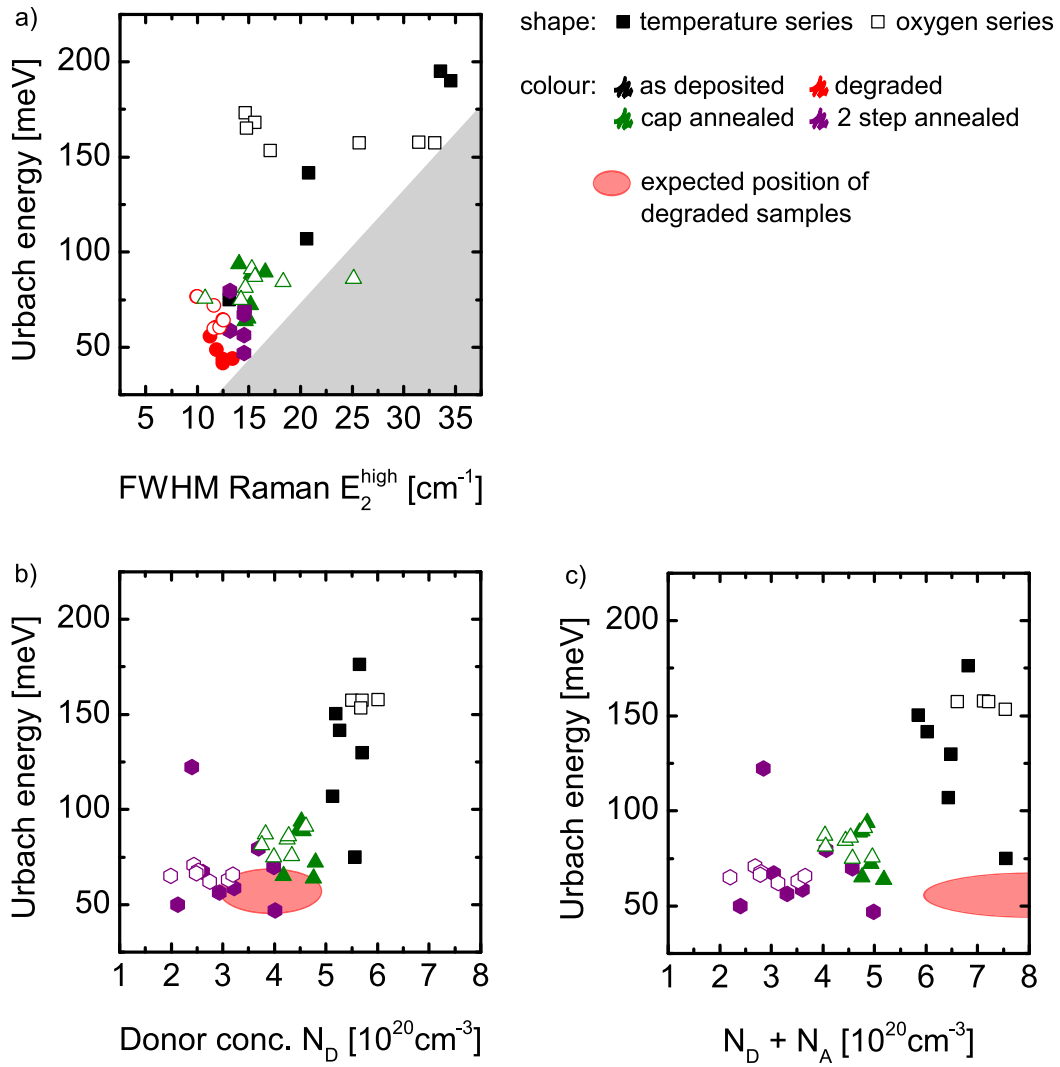


Figure 4.5: Urbach energy of ZnO:Al films of the temperature and oxygen series as function of electrical and structural parameters: a) FWHM of E_2^{high} Raman mode, b) donor concentration N_D and c) sum of donor and acceptor concentration $N_D + N_A$. The red shaded area in part b) and c) represent the expected results of the degraded samples of both series.

4 Discussion

DOS tails due to impurities

The presence of structural defects is not necessarily the only reason for the observation of absorption tails in ZnO:Al. As introduced above, the presence of impurities like extrinsic donors and compensating acceptors may cause energetic defect bands below the conduction and above valence band edge.

Figure 4.5 b) and c) show the Urbach energy E_U of the temperature and oxygen series as function of the donor concentration N_D and of the sum of donor and acceptor concentration N_D+N_A , respectively. A weak trend of increasing tail width with increasing donor and acceptor concentration is observable, especially for low Urbach energies below 100 meV. The disproportionate increase of E_U above $5 \cdot 10^{20} \text{ cm}^{-3}$ donor concentration and above $6 \cdot 10^{20} \text{ cm}^{-3}$ combined donor and acceptor concentration, respectively, concerns only as deposited samples and most probably reflects the influence of their structural defects.

Assuming the applicability of the picture evolved in this work about the development of acceptor and donor concentration for degraded ZnO:Al and still neglecting grain boundaries, than the N_D 's and N_A 's would be located in the red shaded areas, illustrated in the figures 4.5 b) and c). Those samples are expected to be characterised by tremendous compensation and partial deactivation of donors. If DOS tails at the valence band would cause absorption within the band gap, those samples would possess rather high Urbach energies. Since the opposite is observed, only donors may have an influence on the absorption tails.

It can be concluded that in sputtered Al doped ZnO, no trivial reason can be given regarding the development of Urbach like absorption tails. The presented studies support the assumption that the presence of extended structural defects can be viewed as the dominant factor. However, further subordinate influences e.g. related to the donor concentration in the material cannot be excluded. This also shows the cyclic de- and increase of E_U during alternating application of degradation and cap annealing (sec. 3.5).

Regarding the application of ZnO:Al as transparent conductive oxide it is important to note that either the choice of elevated temperature, both, already during film growth or during a post-deposition annealing, or the addition of hydrogen provide a possibility to reduce sub-band gap absorption and, therefore, to significantly enhance the transparency of the film in the vicinity of the band edge.

4.3 Technological relevance

Cap annealed ZnO as transparent contact for optoelectronic devices

The challenge regarding the application of TCOs as electrodes is the trade-off between conductivity and transparency. Therefore, a proper balance between both is necessary. Where the transparency over a wide spectral range is of importance, high conductivity should mainly be reached by a high mobility to avoid optical losses in the near infrared region of the spectrum due to free carrier absorption. Furthermore, the material should possess a large band gap energy and any parasitic absorption in the vicinity of the band edge should be prevented.

With cap annealing of ZnO:Al it is possible to fabricate thin films that feature both, excellent electrical and optical properties. Due to the thickness dependence of the resistivity, best optoelectronic properties are achieved for layers between 500 and 700 nm. In this work prepared 700 nm thick cap annealed ZnO:Al layers, deposited at 200 – 300 °C, reach carrier concentrations in the order of $4 \cdot 10^{20} \text{ cm}^{-3}$ with mobilities around $65 \text{ cm}^2/\text{Vs}$, resulting in a sheet resistance ρ_{sh} of 3Ω . Due to a moderate doping level and the reduction of absorption tails at the band gap, these layers possess a broad optical window with less than 5 % absorbance in the range of 390 – 950 nm.

As mentioned in the introduction of this work, a main aim of the development of ZnO is to find a cheaper replacement for the in industry standardly used indium-based semiconductors.

Comparison with tin-doped indium oxide (ITO)

Regarding display applications widely used TCOs are crystalline or amorphous ITO and amorphous zinc-doped indium oxide (IZO). For industrial use, the most common deposition techniques for these materials are dc or rf magnetron sputtering. Of these TCOs, crystalline ITO, deposited at 250 – 350 °C offers the lowest resistivities in the range of $1 - 4 \cdot 10^{-4} \Omega\text{cm}$ [173–176]. These low conductivities are mainly achieved by carrier concentrations in the range of 10^{21} cm^{-3} which significantly impairs the transparency of the layers in the infrared. That makes these films only interesting for applications in which the IR absorption losses are not relevant, as is the case for display technologies. However, many applications, for instance the deposition of electrodes on the color filter within an LCD display, require preparation temperatures below 200 °C, additionally to low resistivities and thicknesses of approximately 15 to 100 nm [175]. Similar restrictions apply to transparent electrodes deposited onto the active part of a thin film solar cell. Hence, room temperature deposited amorphous ITO with slightly inferior electrical properties but with more controllable wet-etching behaviour for lithographic line definition presents a suitable alternative to c-ITO.

A current research topic and technologically very attractive material is hydrogen-doped indium oxide (IOH) [177, 178]. These thin films are sputtered at room temperature and subsequently annealed at 200 °C. The resulting IOH layers show a remarkably high mobility of $98 - 130 \text{ cm}^2/\text{Vs}$ at carrier densities of $n \approx 2 \cdot 10^{20} \text{ cm}^{-3}$ at a layer thickness of 240 nm. However, even if it is a both electrically and optically excellent material, it nevertheless has the major disadvantage that it is indium-based.

4 Discussion

As shown in this work and in earlier studies of Ruske et. al. [66] and Wimmer et al. [79] resistivities in the range of $2 \cdot 10^{-4} \Omega\text{cm}$ can be achieved with cap annealing of ZnO:Al. These values are not yet as good as for the ITO standard but offers the advantage being much cheaper compared to In-based compounds.

The major drawback, however, represents the strong thickness dependence of the resistivity of ZnO due to inferior film growth during the nucleation phase. The resistivity is considerably increased, even after cap annealing, for those very thin layers required for the display industry [179].

To overcome this problem, an improvement of nucleation is necessary. One approach currently under investigation is the nitrogen mediated crystallisation (NMC), introduced by Itagaki *et al.* [180]. Here, very thin ZnO:Al is crystallised from the amorphous phase via nitrogen atom mediation, yielding 20-nm-thick films with a resistivity of $5 \cdot 10^{-4} \Omega\text{cm}$ and optical transmittance higher than 80 % in a wavelength range of 400 – 2500 nm [180].

Furthermore, these NMC seed-layers affect the sub-sequent growth of sputtered ZnO:Al improving its crystallinity. By means of a combination of this approach with cap annealing of the entire stack, it was possible to prepare ZnO:Al thin films with less than 300 nm in thickness possessing a carrier mobility of about $60 \text{ cm}^2/\text{Vs}$ and a sheet resistance below 15Ω .

In the field of TCO applications requiring sheet resistances of a few Ohms, cap annealed ZnO:Al thin films would be of high interest, since they are superior in NIR transmission, due to a lower carrier concentration. However, ZnO is still exceeded by IOH thin films, considering the optoelectrical properties and the ability to prepare high-quality IOH at temperatures below $200 \text{ }^\circ\text{C}$.

Successful application of cap annealed ZnO:Al in thin film solar cells

For photovoltaic electrode applications, the TCO must be highly transparent across the solar spectrum. Considering ZnO:Al, a way to tailor the electrical properties is the sequent use of annealing with and without protective capping layer, as employed in this work.

Subsequently annealed ZnO:Al layers without and with cap (2 step annealed) have already been successfully applied in a-Si/ $\mu\text{c-Si}$ tandem solar cells showing the relevance and feasibility of the annealing technique. In comparison to cells based on unannealed ZnO:Al films an absolute improvement of 0.7 % of the improved initial conversion efficiency was achieved [116]. This improvement could be attributed to the decrease in free carrier absorption with the simultaneous, significant increase in electron mobility affecting primarily the $\mu\text{c-Si}$ bottom cell.

Furthermore, enhanced transparency close to the fundamental absorption edge causes an improved blue response of the a-Si top cell. This effect is caused by the high temperature related reduction of Urbach-like absorption tails as they have been examined in this work.

Another approach, regarding the application of the cap annealing process, is to decrease the layer thickness without effectively changing the sheet resistance of the material [181]. Reducing the thickness does not just saves material but increases its transmission, as well.

Commonly, the ZnO front contact in thin film solar cells is wet-chemically textured in order to enhance light scattering and, hence, its propagation path length within the solar cell. Here, the surface morphology is crucial for its scattering efficiency. Since the etching behaviour is changing and the resulting topography is worsening with decreasing layer thickness, very thin cap annealed, textured ZnO:Al thin films have not been suitable for application in the standard a-Si/ μ c-Si tandem solar cell [118]. However, this issue could be addressed with decoupling of electrical and light scattering properties by deposition of a very thin ZnO:Al film of 250 nm onto an already textured glass substrate [181]. With this approach, a 70 % ZnO material reduction has been achieved at a conversion efficiency comparable to the 'standard' a-Si/ μ c-Si tandem cell.

Evaluation of the oven treatment

Even if annealing in an oven presents a very simple process not requiring any expensive equipment, the necessary long treatment times are very unattractive for industrial applications. Laser processing would be a promising alternative for the oven. Here, a wide range of variable parameters are available. The treatment could be carried out using continuous wave (cw), pulsed, spot or line laser devices with possible excitation wavelengths between UV and IR. Furthermore, light intensity and scanning speed are adaptable as well as the treatment atmosphere.

First studies showed that a wavelength in the IR region of the spectrum is more suitable for treating ZnO since it gets sufficiently well absorbed by free carriers and provides a more homogeneous energy distribution within the layer compared to UV radiation [182, 183]. However, a drawback is the necessary adaption of excitation parameters to the carrier concentration of the material since the latter determines the light absorption in the respective spectral region.

In both works of Horn *et al.* [182] and Schumann [183], cw-laser radiation with a wavelength of 1070 nm and different scanning velocities have been employed to study the annealing effect on ZnO:Al, both, bare and capped with silicon oil. The silicon oil was used to provide a similar protection effect as the 'standard' a-Si capping layer.

Due to a very short interaction time of the laser with the ZnO film in the order of milliseconds, the impact on the treated film is, by far, not as pronounced as observed for oven treatments. The general trends of deterioration of the layer's electrical properties during laser annealing in air and their considerable improvement after annealing under a cap, however, are maintained. Even for these strongly reduced treatment times, laser annealing under a protective capping layer was able to increase, both, carrier concentration and mobility by about 20 % [183].

Hence, it could be shown that an electrical improvement of thermally treated aluminium-doped ZnO thin films using laser radiation is in principle possible. For industrial application, however, the method should be adapted to laser systems with higher performance for large-area processing.

5 Summary and outlook

In this study aluminium-doped zinc oxide (ZnO:Al) thin films, prepared under different deposition conditions and subsequently annealed in nitrogen ambience, have been structurally, electrically and optically characterised. The variation of deposition parameters has been selected specifically to promote a deeper understanding of the underlying mechanisms of ZnO annealing with and without protective a-Si:H capping layer. In particular, this involved the change of the substrate temperature and the additional supply of either oxygen, nitrogen and hydrogen during film growth.

Electrical properties

Annealing under a protective silicon capping layer significantly improves the electrical and optical properties of ZnO:Al that is primarily caused by a substantial increase in electron mobility. However, the degree of improvement is strongly dependent on the deposition conditions. In order to achieve a maximum mobility, already electrically superior layers in their as deposited state have to be treated.

Thermally treated bare films, however, are characterised by deteriorated electrical properties. A subsequent combination of both treatments allows a selective variation of the electrical and optical properties within certain limits, aiming at layers with reduced carrier concentration but enhanced mobility.

Regarding the application of zinc oxide thin films as transparent electrodes, an improvement of the electrical properties is technologically relevant, since it principally allows the use of thinner films with the same sheet resistance whose optical properties are, besides a positive effect of enhanced charge carrier mobility, improved by a decreased layer thickness.

The aim of this work has been a systematic investigation of the origin of the fundamental differences between thermal post-deposition treatments of ZnO:Al with and without amorphous silicon layer in nitrogen ambient.

It could be shown that nitrogen has no substantial impact on the degradation of electrical properties attributed to annealing without cap since ZnO:Al, purposely grown under nitrogen atmosphere and thermally untreated, differs significantly in colour from ZnO:Al annealed in nitrogen ambience.

By means of a simplified model considering ionised impurities and phonons as dominant scattering sites, donor and acceptor concentrations have been determined and discussed regarding the activation, deactivation and compensation of donors by interaction of the treated ZnO:Al film with either cap material or annealing ambient.

5 Summary and outlook

It could be concluded that the resulting properties of ZnO:Al after annealing are primarily influenced by the prevailing oxygen partial pressure during the process. Annealing under high oxygen partial pressure includes treatments of bare ZnO:Al in atmospheres containing at least a small amount of residual oxygen. It strongly promotes the creation of oxygen-related acceptors like zinc vacancies or oxygen interstitials, leading to a compensation of donors and tremendously decreased electron mobility by enhanced ionised impurity scattering.

Annealing beneath a silicon cap can be considered as a treatment under low oxygen partial pressure. Here, it could be observed that previously present acceptors are annihilated causing a considerable increase in mobility. Oxygen migrates to the ZnO/Si interface, creating silicon oxide, while most likely the, then, available zinc fills zinc vacancies. Cap annealing, however, is also accompanied by a minor decrease in donor concentration, presumably by the creation of neutral defect complexes or aluminium oxide.

Since hydrogenated amorphous silicon is used as standard capping material, it was supposed that the incorporated hydrogen diffuses into the underlying ZnO:Al film during annealing, being responsible for the observed improvement of electrical properties. Although it could be shown that hydrogen incorporation during growth is able to enhance the electric transport, it is nearly completely removed for post-deposition treatment temperatures above 500 °C. Furthermore, no significant difference in annealing behaviour could be observed using hydrogen-rich PECVD deposited amorphous silicon and essentially hydrogen-free electron beam evaporated silicon as protective capping layer.

Hence, it could be concluded that hydrogen incorporation from the cap material is not primarily responsible for the enormous enhancement of electrical properties after cap annealing as suspected before.

Sub-band gap absorption

For low temperature deposited ZnO:Al films, broad absorption tails can be observed which adversely affect the layer's transparency and, hence, the efficiency of ZnO-electrode based optoelectronic devices like thin film solar cells.

These tails are clearly temperature related since they can be significantly decreased by high deposition temperatures or post-deposition annealing. Comparison with Raman experiments indicate a correlation with structural improvement of the layer. However, a larger supply of oxygen during growth result in comparable Raman crystallinity but yield layers with still very pronounced Urbach tails. Hydrogen, on the other side, is able to passivate at least a large proportion of tail causing defects.

Hence, defects that are curable by high temperature processes or passivated by hydrogen can be regarded as the main cause of decreased transmission in the vicinity of the absorption edge. Furthermore, according to the results regarding donor and acceptor concentration obtained in this work, a subordinate influence of donors by creation of density-of-state tails is suspected.

Resonant enhancement of Raman response

It was observed that resonant enhancement of longitudinal-optical phonon modes in ZnO is directly related to occurrence and severity of absorption in vicinity of the respective Raman excitation energy within the band gap. This absorption can be either caused by broad Urbach tails or, in case of narrow tails, by electronic states related to the appearance of an additional, very controversially discussed, Raman mode at 275 cm^{-1} .

Outlook

Especially the uncertainty regarding the role of neutral defect complexes presents an important topic for further investigations. After all, they are likely to be responsible for a lowered doping efficiency associated with the annealing processes. A quantification of the loss in donors would be possible with a modified version of the multi-step annealing experiment with alternating application of degradation and cap annealing. It has to be adapted in so far that cracking of the layers has to be prevented, enabling the measurement of electrical properties.

Furthermore, concerning the comprehension of the limitation of electrical transport in degraded samples, the current status is unsatisfactory. Further insights could be provided by the investigation of samples degraded weakly at low temperatures, especially regarding the influence of grain boundaries. However, this would require an improved model about the mechanisms of grain boundary scattering including an extension for degenerate semiconductors and the consideration of tunnelling.

Considering the applied model for determination of donor and acceptor concentrations, only particular defects were considered which are assumed to be dominant in ZnO. For verification it would be appropriate to study e.g. their occurrence depending on the applied annealing temperature and cross-check with calculations of their activation energies. Transfer of the process to an even more temperature stable substrate would allow the assessment of a wider temperature range required for an estimation of involved activation energies. However, this would require a substrate which is suitable for very high temperatures and still thermally matched with ZnO. Since the prevailing oxygen partial pressure is very likely the main driver of changes in ZnO during thermal post-deposition treatments, annealing experiments in atmospheres with very low, but well defined and controlled oxygen partial pressures would help regarding a further evaluation of this theory.

Finally, to support the proposition regarding the resonant Raman enhancement in presence of pronounced Urbach tails, a variation of the Raman excitation wavelength would be adjuvant. This should especially include a shift of excitation towards even lower energies.

Appendix

A Determination of the optical absorption coefficient

The determination of the absorption coefficient α of thin films is of importance since it provides information about the electronic band structure, band tails and localised defect states. Furthermore, compared to the total absorbance, it depends only on material properties and not on the thickness of the individual investigated layers.

In the spectral region between UV and NIR, α is usually determined from optical transmittance (T) and reflectance (R) measurements. However, due to optical interference effects the experimental determination of α is not trivial.

Figure A.1 gives an overview over the typically employed methods for calculating α . Part a)

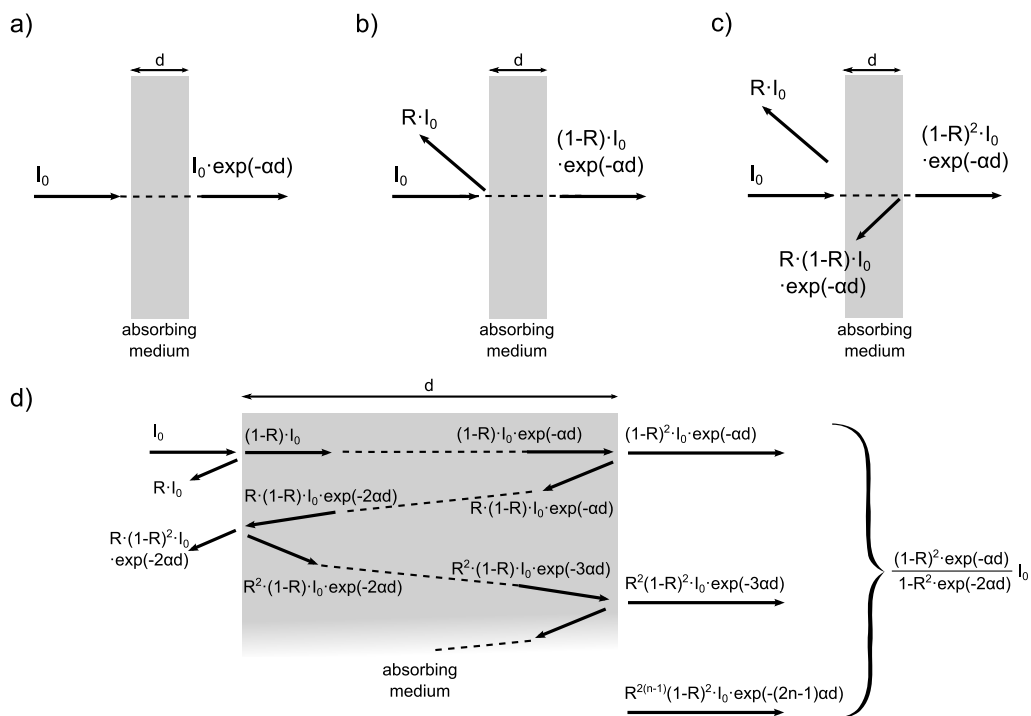


Figure A.1: Illustration of light propagation in an absorbing material according to a) the general form of Lambert-Beer's law, b) accounting for reflection at the incident interface and c) additionally at the second interface and d) taking multiple internal reflections into account; Part d) is taken from Pankove [60].

A Determination of the optical absorption coefficient

illustrates basically equation 2.39. Supposing that $I_0 \cdot \exp(-\alpha d)$ can be interpreted as the transmitted part of the incident radiation, some studies (e.g. [57, 59]) in literature extract α using

$$\alpha_1 = -\frac{1}{d} \ln(T), \quad (\text{A.1})$$

where d is the layer thickness.

This method neglects the light reflected at the surface of the sample which results in sufficiently large errors depending on the spectral region and the refractive index of the material. Even the calculation of α using just the reflectance of ZnO powder [58] or using the absorptance [184] of a ZnO film on glass can be found in literature.

Taking the reflection at the incident surface into account (figure A.1 b)), α can be obtained by

$$\alpha_2 = -\frac{1}{d} \ln\left(\frac{T}{1-R}\right). \quad (\text{A.2})$$

This method is most frequently used, especially regarding the study of absorption behaviour of TCOs on glass (e.g. [61, 62]).

However, even improved by considering reflection at the front surface, this model still neglects reflection at the backside and internal reflection at a possible substrate-layer interface. Therefore, another method extends eq. A.2 to the reflection on the back (fig. A.1 c)):

$$\alpha_3 = -\frac{1}{d} \ln\left(\frac{T}{(1-R)^2}\right). \quad (\text{A.3})$$

This actually represents an approximation of the approach illustrated in figure A.1 d) where not just one but multiple internal reflections are taken into account. Both have in common that they are just applicable in the case of free-standing films even without a transparent, non-absorbing substrate. A substrate would mainly cause a change of the reflection coefficient at the backside since it acts anti-reflectively. This may lead to the case that $(1-R)^2$ is larger than T which, in turn, causes a physically not reasonable negative absorption coefficient.

A correct determination of the absorption coefficient of a thin absorbing layer on glass is just possible using the *transfer matrix method*, which is used for the design of anti-reflective coatings and dielectric mirrors. It calculates the real and imaginary part of the refractive index n and κ , respectively, from experimentally determined R and T taking the individual Fresnel coefficients at the possible multiple interfaces into account and considers, next to partly transmitted and partly reflected light, phase changes of the light due to

different refractive indices of the respective layers. This method, however, requires extensive computational effort and leads to multiple solutions with the same error. It usually demands even more numerical computation to find the correct physical solution than to calculate α itself [112].

In this work, the second approach (eq. A.2) has been chosen to determine the absorption

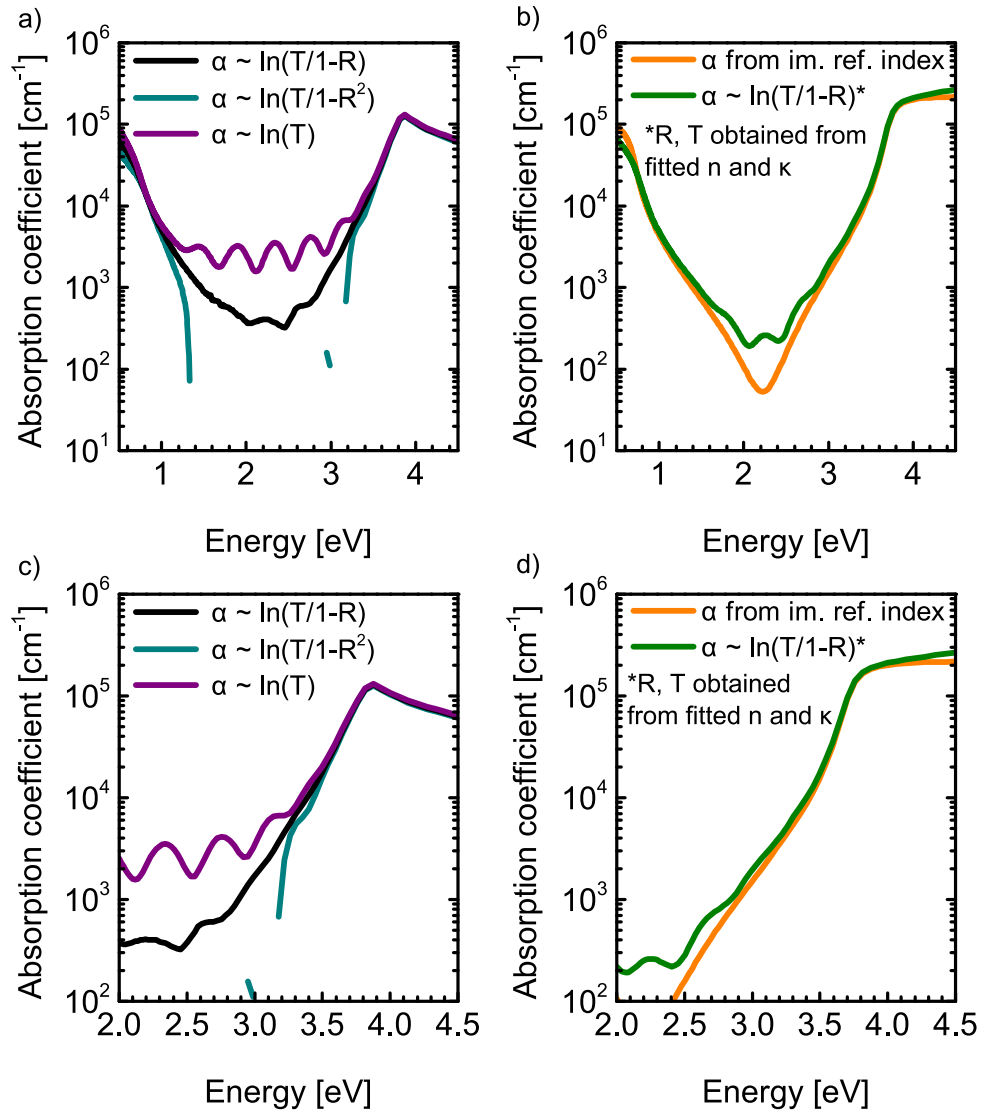


Figure A.2: Comparison of the results of different methods for obtaining the absorption coefficient α ; Part a) shows the calculated α using just transmission T (eq. A.1), reflection R and transmission T (eq. A.2) and R^2 and T (eq. A.3). Part b) compares the outcome of eq. A.2 with the determination of α using the imaginary part of the refractive index κ , which was obtained by fitting the reflection and transmission spectra with a Sernelius-Leng-oscillator. Further information are provided in the text below. c) and d) provide a magnification of a) and b), respectively, in the band gap region.

A Determination of the optical absorption coefficient

coefficient of the investigated ZnO:Al thin films on glass neglecting multiple internal reflections. For ZnO with a refractive index of around $n = 2$ the error due to that neglect of multiple internal reflections is fairly small since the difference in refractive index to air ($n = 1$) and the glass substrate ($n \approx 1.5$) is quite low. This method would be more or less unsuitable for the determination of α of a thin film on glass with higher refractive index like for example amorphous silicon ($n \approx 3 - 4$).

Figure A.2 shows the results of calculating α of a representative ZnO:Al layer using equations A.1 – A.3. Furthermore, both parts of the complex refractive index n and κ have been determined by fitting experimental R and T with a *Sernelius-Leng*-oscillator, which provides a good model for describing the spectra. For a detailed description of the formalism reference is made to the work of *Pflug et al.* [115].

With the imaginary part of the refractive index κ , α was obtained by using eq. 2.40 via the transfer matrix formalism. Based on n and κ , reflection and transmittance is determined again. Calculating now α using eq. A.2 from these simulated, idealised R and T spectra, which are free from measurement errors, an evaluation of the method itself is possible.

The methods employing $\ln(T)$ and $\ln(T/(1 - R)^2)$ yield wrong results for the part of the spectrum with a high transmittance and low reflectance, respectively (fig. A.2 a)). Completely neglecting the part of the light reflected at the incident surface overestimates α while wrong negative α are obtained using the $\ln(T/(1 - R)^2)$ method.

Comparing α calculated by Lambert-Beer's law (eq. A.2) from simulated R and T with α from κ show considerable deviations in spectral region where ZnO film is highly transparent. This is due to multiple reflections in the ZnO layer which are not considered in the model that obtains κ .

Generally, it has to be noted that a decrease of absorption rather than a saturation for energies slightly above the band gap can be observed for the most of the experimentally determined absorption coefficients in this work. This is due to an error in transmission measurement and happens for those samples that have been measured with the incident light illuminating the substrate first.

Figure A.3 a) shows the transmittance of a representative ZnO:Al layer between 200 and 500 nm measured with illumination from the substrate and from the layer side. It appears that the transmittance of the layer is increasing again for $\lambda < 320$ nm when the glass side of the sample stack is illuminated. For wavelengths below this threshold, the incident light causes fluorescent transitions in the glass, meaning that the light gets absorbed but reemitted with a longer wavelength. Figure A.3 b) shows an exemplary fluorescence spectrum of the bare glass substrate when excited with $\lambda = 266$ nm. It can be observed that the glass emits light mainly in a spectral region in which the ZnO:Al layer on the substrate is transmitting. Therefore, it appears that below an excitation wavelength of 320 nm the ZnO:Al layer is gaining transparency again.

Turning the sample around so that the ZnO:Al layer is illuminated first, results in a complete absorption of the UV area of the spectrum by the ZnO film. Hence, the glass is not excited anymore and does not influence the measurement.

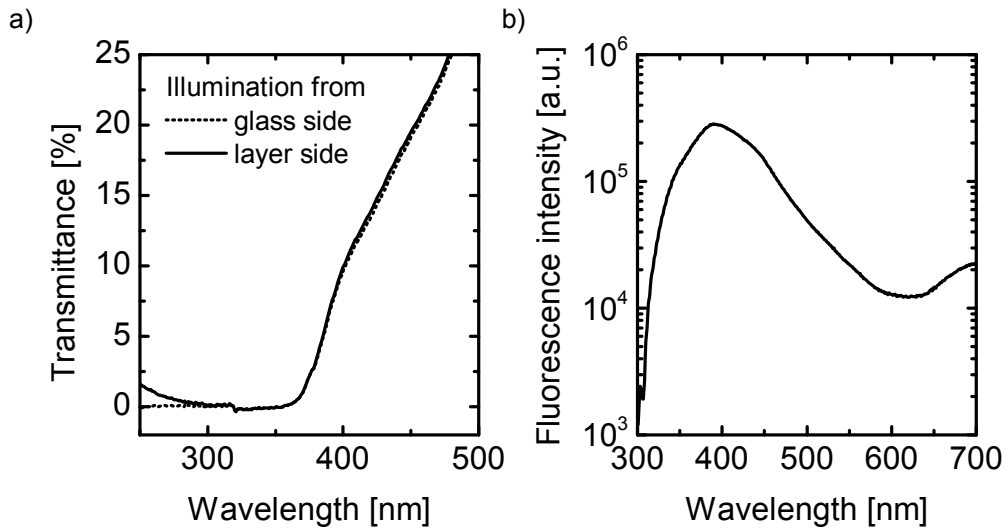


Figure A.3: a) Representative transmittance spectrum of a ZnO:Al thin film in the wrong substrate position with respect to the incident light during measurement; b) Fluorescence spectrum of the bare glass substrate, excited with a wavelength of 266 nm^1

In conclusion, for investigation of the band gap region of ZnO:Al eq. A.2 provides a sufficiently good method for calculating α . The error obtained by this method is mainly depending on the difference in refractive indices of the investigated thin film and the substrate. In case of ZnO on glass, this difference is sufficiently small and causes just minimal reflection around 2 % at the ZnO/glass interface.

Issue of interference fringes in absorption coefficient spectra

All conventional methods for the determination of α of thin films have in common that they yield interference fringes in the resulting spectrum. These may, in some cases, substantially affect the determination of the band gap energy and other optical effects at the band edge [185]. Therefore, different approaches have been developed to suppress these interference fringes in the spectrum.

Ritter *et al.* [186] and Hishikawa *et al.* [185] proposed methods showing that the ratios A/T and $T/(1 - R)$ yield basically interference free spectra and that the absorption coefficient α can be calculated by them.

However, these methods require that the maxima and minima of the interference fringes in transmission and reflection measurements occur always at the same wavelength. That is theoretically the case, however, in practice slightly inhomogeneous layers or a small deviation in position for R and T measurements lead to a slight shift of the relative position of interference fringes in R and T spectra. Applying Ritter's or Hishikawa's method, this shift leads to an attenuation but not to a complete suppression of interference in absorption coefficient spectra.

¹⁶The fluorescence spectrum was kindly provided by S. Tannert of Picoquant GmbH.

B Limits for the determination of Urbach energy

(I) Differentiation between small Urbach tails and low energy side of the error function

In order to evaluate the error of the Urbach tail, fictional absorption coefficients at a fixed band gap energy have been generated that equal to pure error functions with variable widths Γ between 50 and 200 meV since this is the range of widths obtained for the samples investigated in this work. These data sets have been fitted using the model of eq. 2.42, which has been used for all samples except for those of the nitrogen series.

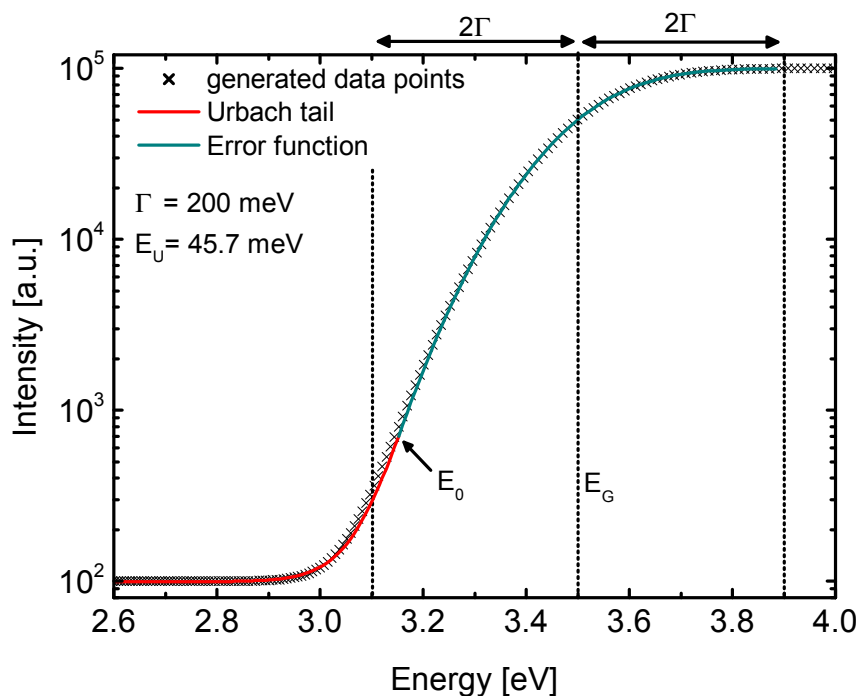


Figure B.1: Exemplary fictional data set simulating the absorption coefficient at the band edge energy corresponding to an error function with a width of $\Gamma = 200$ meV; Furthermore, a fit using an Urbach tail for the low energy part of the absorption edge according to eq. 2.42 is given.

B Limits for the determination of Urbach energy

Figure B.1 shows, as demonstration, the fit of an error function with $\Gamma = 200$ meV. It can be seen that an exponential Urbach tail can be fitted reasonable well even to a pure error function for energies below the fit transition point E_0 . In this case, the fit yields an Urbach energy E_U around 45 meV which is in the order of magnitude of tail widths extracted for degraded ZnO:Al. Therefore, it must be assumed that for samples without additional absorption tail the fit would create an artificial and unphysical one, anyway.

However, fitting bare error functions with variable width using eq. 2.42 showed that the transition point E_0 , where the fit error function devolves into the exponential Urbach tail, is always situated far from the band gap energy but never below $E_g - 2\Gamma$. Figure B.2 a) shows that if E_0 is variable within the fitting routine it tends to take values just slightly above $E_g - 2\Gamma$. In combination with fig. B.2 b) it also demonstrates that for $E_0 < E_g - 2\Gamma$ the mean square error (MSE) of the fit increases dramatically since the model is not applicable anymore.

In conclusion, if no regular exponential tail is present and if the near edge sub-band gap absorption is caused just by the natural line width describable by an error function, then the model of eq. 2.42 can be employed anyway with a low MSE but yields transition energies far below the band gap energy.

For all experimentally obtained data fitted with this model in this work E_0 deviated from the band gap energy in really rare cases by 200 meV at the maximum, supposing that these samples are not significant. Mostly, E_0 was equal to the fitted band gap energy.

Therefore, it is assumed that a fitting of all data sets investigated in this work required the addition of an Urbach tail.

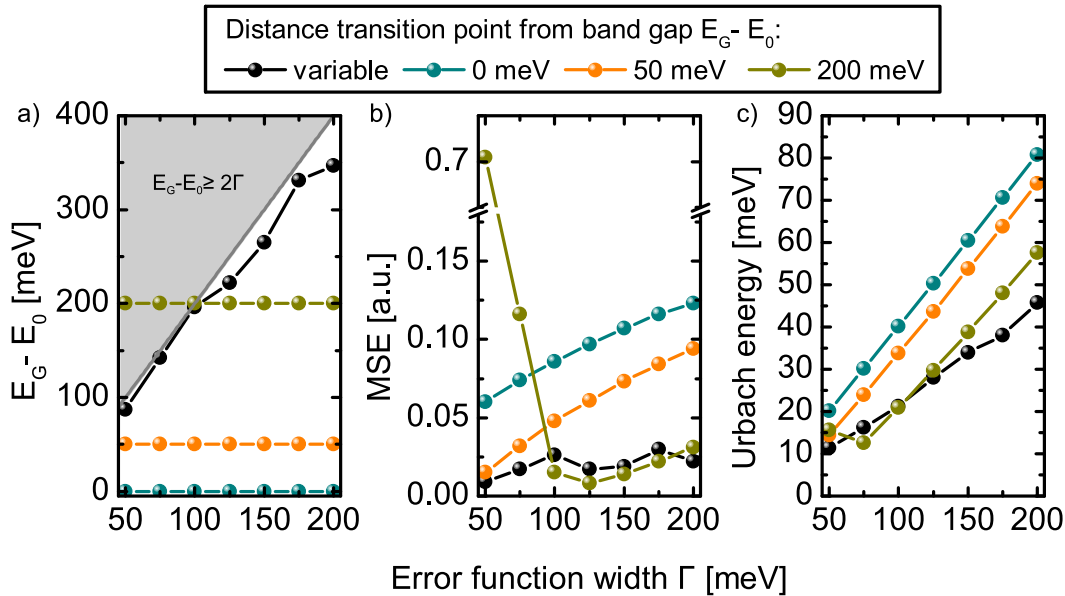


Figure B.2: a) Deviation of the transition point E_0 from the band gap energy E_g , b) mean square error (MSE) of the fit using eq. 2.42 and c) extracted Urbach energy as function of the error function width Γ

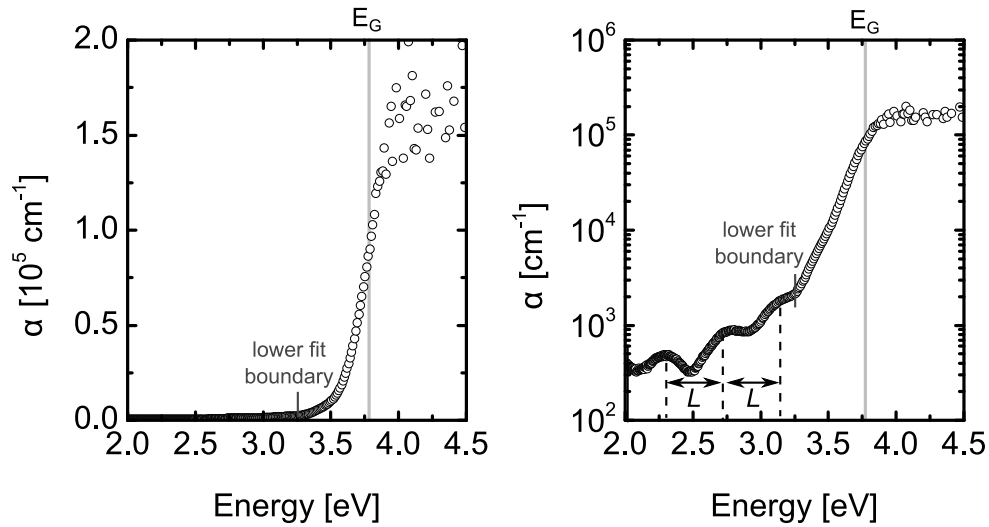


Figure B.3: Representative absorption coefficient spectrum of a ZnO:Al thin film with approximately 700 nm thickness on linear and logarithmic scale; Indicated with dashed lines are the position of interference maxima occurring with a 'periodic length' of L .

(II) Lower limit for Urbach tails

Taking the considerations above into account, the smallest fittable Urbach tail would be from an absorption coefficient spectrum just very slightly deviating from a pure error function but with the requirement of $E_0 \ll E_g - 2\Gamma$. Assuming that the distance between E_G and E_0 is between 0 meV and 50 meV at a maximum to determine a regular Urbach tail, the upper boundary for the MSE of the fit can be taken from figure B.2 b). It should be well below 0.125 for Γ up to 200 meV and below 0.05 for Γ around 50 meV. These conditions were met for the fits of all samples in this work.

Figure B.2 c) shows the extracted Urbach energies E_U for the fictional absorption coefficients corresponding to error functions with widths Γ between 50 and 200 meV. In that figure, the orange curve represents the lowest obtainable Urbach energies in dependence of the error function width, assuming again that a proper Urbach tail is just obtainable when the fitted transition point E_0 deviates by 50 meV from E_g , at the maximum.

The ZnO layer of this work exhibited Γ values between 50 meV for mainly degraded samples and up to 200 meV for samples in their as deposited state or after cap annealing. That means the lower limits for Urbach energies can be expected in the range of 20 meV for degraded films and 80 meV for as deposited and cap annealed ones. For fitted E_U 's below these limits the absorption coefficient data could have been fitted with an error function alone and these samples have to be considered as essentially Urbach tail-free.

(III) Lower boundary for fit – Issue of interference fringes in absorption spectrum

As already indicated in appendix A the appearance of interference fringes have a significant

B Limits for the determination of Urbach energy

influence on the determination of the Urbach tail. Figure B.3 shows a representative absorption coefficient α spectrum of a ZnO:Al thin film with approximately 700 nm thickness on linear and logarithmic scale. Considering for α just the linear plotting, interference maxima and minima are hardly visible and seem not to disturb any fit of the band edge. Since considerable thick layers have been investigated in this work, large scattering of α in the saturation range above the band gap energy occurs due to vanishing transmittance.

In order to decrease the impact of errors above the band gap energy and to focus on the low-energy part of the absorption edge $\ln \alpha$ was fitted using the logarithm of eq. 2.42 to avoid a huge influence of the high-energy end of the absorption edge on the MSE of the fit. On the logarithmic scale, however, interference fringes appear. If the lower energy boundary for the fit is inappropriately chosen, the extracted Urbach energies can differ substantially up to 30 %.

Therefore, for a consistent fit routine the lower boundary for all fits was chosen at the first perceptible minimum seen from the high-energy side (see figure B.3).

List of publications

Publications related to the PhD project

Publications in journals

- S. Schönau, F. Ruske, S. Neubert, and B. Rech, *Analysis of Urbach-like absorption tails in thermally treated ZnO:Al thin films*, Appl. Phys. Lett. 103, 192108 (2013).
- B. Stannowski, F. Ruske, S. Neubert, S. Schönau, S. Ring, S. Calnan, M. Wimmer, O. Gabriel, B. Szyszka, B. Rech, and R. Schlatmann, *Potential of high-mobility sputtered zinc oxide as front contact for high efficiency thin film silicon solar cells*, Thin Solid Films 555, 138-142 (2014).
- R. Muydinov, A. Steigert, S. Schönau, F. Ruske, R. Kraehnert, B. Eckhardt, I. Lauer-mann, and B. Szyszka, *Water-assisted nitrogen mediated crystallisation of ZnO films*, Thin Solid Films 590, 177-183 (2015).

Conference proceedings (peer reviewed)

- F. Ruske, R. Rößler, M. Wimmer, S. Schönau, S. Kämpfer, M. Hendrichs, S. Neubert, L. Korte, and B. Rech, *ZnO:Al with tuned properties for photovoltaic applications: thin layers and high mobility material*, Proc. SPIE 8626, 86260Y (2013).
- S. Schönau, F. Ruske, S. Neubert, and B. Rech, *Annealing related changes in near-edge absorption and structural properties of Al-doped ZnO thin films*, physica status solidi (c) 11, 1468-1471 (2013).
- S. Schönau, F. Ruske, S. Neubert, and B. Rech, *Investigation of Band Tailing in Sputtered ZnO:Al Thin Films Regarding Structural Properties and Impurities*, MRS Proc. 1699 (2014).
- F. Ruske, S. Schönau, S. Ring, S. Neubert, B. Stannowski, V. Sittinger, S. Götzendörfer, and B. Rech, *Material properties of high-mobility TCOs and application to solar cells*, Proc. SPIE 8987, Oxide-based Materials and Devices V, 898723 (2014).

Publications not related to the PhD project

- S. Schönau, J. Rappich, M. Weizman, D. Amkreutz, and B. Rech, *Photoluminescence study of polycrystalline silicon thin films prepared by liquid and solid phase crystallization*, physica status solidi (a) 210, 1652-1656 (2013).

B Limits for the determination of Urbach energy

- D. Amkreutz, J. Haschke, S. Schönau, F. Ruske, and B. Rech, *Light trapping in polycrystalline silicon thin-film solar cells based on liquid phase crystallization on textured substrates*, IEEE 39th Photovoltaic Specialists Conference (2013).
- J. Hegmann, R. Jahn, S. Schönau, N. Sommer, and P. Löbmann, *SiO₂ -TiO₂ Scattering Layers Prepared by Sol-Gel Processing for Light Management in Thin Film Solar Cells*, Journal of Sol-Gel Science and Technology 74, 585-593 (2015).

List of Figures

2.1	ZnO in wurtzite structure	3
2.2	Illustration of optical phonon modes	4
2.3	Fermi energy and effective mass as function of carrier concentration.	13
2.4	Absorption, transmittance and reflection of ZnO:Al thin film	15
2.5	Band diagram of absorption edge	16
2.6	Exemplary absorption coefficient and illustration of fit	19
2.7	Illustration of annealing treatments	24
2.8	Setup configuration spectrophotometer	25
2.9	Illustration Raman scattering	28
2.10	Illustration Bragg condition and Bragg-Brentano focusing geometry for XRD	30
3.1	XRD spectra temperature series, as deposited	34
3.2	Peak position and FWHM (002) XRD reflex of temperature series, as deposited	35
3.3	Surface SEM micrographs of temperature series, as deposited	36
3.4	Raman spectra of temperature series, as deposited	38
3.5	Electrical properties temperature series, as deposited	39
3.6	Urbach energy and Raman E_2^{high} FWHM of temperature series, as deposited	40
3.7	Absorptance and 574 cm^{-1} mode of temperature series	41
3.8	XRD spectra temperature series, annealed	43
3.9	Peak position and FWHM (002) XRD reflex of temperature series, annealed	44
3.10	Surface SEM micrographs of temperature series, annealed	45
3.11	Raman spectra of temperature series, annealed	46
3.12	Electrical properties temperature series, annealed	48
3.13	Absorptance of temperature series in as deposited state and after annealing	49
3.14	Urbach energy and Raman E_2^{high} FWHM of temperature series, annealed	50
3.15	Absorptance of temperature series in vicinity of Raman excitation energy, annealed	51
3.16	Mobility limits according to Look and Pisarkiewicz with individual components.	54
3.17	Donor and acceptor concentrations for the ZnO:Al layers of the temperature series according to the scattering model of D. Look	55
3.18	Electrical properties oxygen series, as deposited	58
3.19	XRD spectra oxygen series, as deposited	59
3.20	Peak position and FWHM (002) XRD reflex of oxygen series, as deposited	60
3.21	Surface SEM micrographs of oxygen series, as deposited	61
3.22	Raman spectra of oxygen series, as deposited	62
3.23	Absorption coefficient of of oxygen series	63

List of Figures

3.24	Urbach energy and Raman E_2^{high} FWHM of oxygen series, as deposited . . .	63
3.25	Raman spectra of oxygen series, annealed	65
3.26	Urbach energy and Raman E_2^{high} FWHM of oxygen series, annealed	66
3.27	Raman spectra around 574 cm^{-1} and absorption coefficient oxygen series in vicinity of Raman excitation energy, annealed	67
3.28	Electrical properties of oxygen series, annealed	69
3.30	Donor and acceptor concentration for the as deposited and annealed ZnO:Al layers of the oxygen series	71
3.31	XRD spectra nitrogen series, as deposited	73
3.32	Peak position and FWHM (002) XRD reflex of nitrogen series, as deposited	74
3.33	Surface SEM micrographs of nitrogen series, as deposited	75
3.34	Raman spectra of nitrogen series, as deposited	76
3.35	Electrical properties nitrogen series, as deposited	77
3.36	Absorption coefficients nitrogen series and fit demonstration, as deposited .	78
3.37	XRD spectra of nitrogen containing ZnO:Al, as deposited and weakly annealed	79
3.38	Resistivity of nitrogen series, weakly annealed	80
3.39	Electrical properties nitrogen series, annealed	80
3.40	Absorption coefficient nitrogen series, annealed	81
3.41	Gauss peak area and center of nitrogen series, annealed	82
3.42	Schematic band diagram of a) non-degenerated and b) degenerated ZnO with nitrogen related possible acceptor bands	83
3.43	EDX material composition nitrogen doped samples before and after annealing	84
3.44	μ as function of n nitrogen and temperature series	86
3.45	Comparison absorption coefficient temperature, oxygen and nitrogen series	87
3.46	Carrier concentration, mobility and Urbach energy as function of hydrogen concentration	90
3.47	n and μ before and after annealing for different cap materials	92
3.48	Urbach energy for different cap materials after annealing	93
3.49	Absorption coefficient multi-step cap annealing with and without intermediate de-capping	96
3.50	SEM cross section and surface micrographs of ZnO:Al layers subsequently treated with multiple cap annealings but intermediate cap removal	97
3.51	Absorption coefficient of subsequently and alternately degraded and cap annealed layers	98
3.52	Band gap energy of ZnO:Al films that got alternately and subsequently degraded and cap annealed	99
3.53	Urbach energy of ZnO:Al films that got alternately and subsequently degraded and cap annealed	100
4.1	μ as function of n for oxygen series	104
4.2	Simplified illustration of the annealing processes in terms of changes in donor and acceptor concentration in dependence of the applied oxygen partial pressure condition.	107
4.3	Urbach tailing scheme	109

4.4	Urbach energy of ZnO:Al as function of post-deposition annealing temperature.	114
4.5	Comparison of Urbach energy with electrical and structural parameters . .	115
A.1	Illustration of light propagation in an absorbing material	127
A.2	Comparison of the results of different methods for obtaining the absorption coefficient	129
A.3	Transmission of ZnO:Al layer in different configurations and fluorescence spectrum of glass substrate	131
B.1	Exemplary fictional data set simulating the absorption coefficient at the band edge energy	133
B.2	Fit transition, MSE and Urbach energy in dependence of error function width	134
B.3	Demonstration of lower fit boundary for Urbach tail determination	135

List of Tables

2.1	Optical phonon modes ZnO	5
2.2	ZnO material parameters used for mobility model of D. Look with effective masses according to Look and Pisarkiewicz	14
2.3	Sample overview	22
2.4	Deposition parameter a-Si:H	23
3.1	Overview of used cap materials	92

Bibliography

- [1] J. Klingshirn, C.F., Waag, A., Hoffmann, A., Geurts. Crystal Structure, Chemical Binding, and Lattice Properties. In *Zinc Oxide - From Fundamental Properties Towards Novel Applications*, chapter 1, page 17. Springer, 2010.
- [2] T. C. Damen, S. P. S. Porto, and B. Tell. Raman Effect in Zinc Oxide. *Physical Review*, 142(2):570–574, 1966.
- [3] C. A. Arguello, D. L. Rousseau, and S. P. S. Porto. First-Order Raman Effect in Wurtzite-Type Crystals. *Physical Review*, 181(3):1351–1363, 1969.
- [4] J. Serrano, A. Romero, F. Manjón, R. Lauck, M. Cardona, and A. Rubio. Pressure dependence of the lattice dynamics of ZnO: An ab initio approach. *Physical Review B*, 69(9):094306, March 2004.
- [5] R. Cuscó, E. Alarcón-Lladó, J. Ibáñez, L. Artús, J. Jiménez, B. Wang, and M. Callahan. Temperature dependence of Raman scattering in ZnO. *Physical Review B*, 75(16):165202, April 2007.
- [6] D.C Look, D.C Reynolds, Z.-Q Fang, J.W Hemskey, J.R Sizelove, and R.L Jones. Point defect characterization of GaN and ZnO. *Materials Science and Engineering: B*, 66(1-3):30–32, December 1999.
- [7] T. Minami. New n-type transparent conductive oxides. *MRS Bulletin*, 25(8):38–44, 2000.
- [8] S. Zhang, S.-H. Wei, and Alex Zunger. Intrinsic n-type versus p-type doping asymmetry and the defect physics of ZnO. *Physical Review B*, 63(7):075205, January 2001.
- [9] A. F. Kohan, G. Ceder, D. Morgan, and C. G. Van de Walle. First-principles study of native point defects in ZnO. *Phys. Rev. B*, 61:15 019 – 15 027, 2000.
- [10] A. Janotti and C. G. Van de Walle. Native point defects in ZnO. *Physical Review B*, 76(16):165202, October 2007.
- [11] C. G. Van De Walle. Hydrogen as a cause of doping in zinc oxide. *Physical review letters*, 85(5):1012–5, July 2000.

Bibliography

- [12] B. K. Meyer, J. Sann, D. M. Hofmann, C. Neumann, and A. Zeuner. Shallow donors and acceptors in ZnO. *Semiconductor Science and Technology*, 20(4):S62–S66, April 2005.
- [13] C. H. Park, S. B. Zhang, and Su-Huai Wei. Origin of p-type doping difficulty in ZnO:Al - The impurity perspective. *Physical Review B*, 66(7):073202, August 2002.
- [14] L. G. Wang and Alex Zunger. Cluster-Doping Approach for Wide-Gap Semiconductors: The Case of p-Type ZnO. *Physical Review Letters*, 90(25):256401, June 2003.
- [15] P. Drude. Zur Elektronentheorie der Metalle. *Annalen der Physik*, 306, 1900.
- [16] H. Ibach and H. Lüth. Motion of Electrons and Transport Phenomena. In *Solid-State Physics: An Introduction to Principles of Materials Science*, chapter 9. Springer Science & Business Media, 2003.
- [17] D. C. Look. (Wiley, New York, 1989), Ch. 1. In *Electrical Characterization of GaAs Materials and Devices*, chapter 1. Wiley, New York, 1989.
- [18] S. Brehme, F. Fenske, W. Fuhs, E. Nebauer, M. Poschenrieder, B. Selle, and I. Sieber. Free-carrier plasma resonance effects and electron transport in reactively sputtered degenerate ZnO:Al films. *Thin Solid Films*, 342:167–173, 1999.
- [19] D. L. Young, T. J. Coutts, V. I. Kaydanov, a. S. Gilmore, and W. P. Mulligan. Direct measurement of density-of-states effective mass and scattering parameter in transparent conducting oxides using second-order transport phenomena. *Journal of Vacuum Science & Technology A: Vacuum, Surfaces, and Films*, 18(6):2978, 2000.
- [20] D. C. Look, K. D. Leedy, L. Vines, B. G. Svensson, A. Zubiaga, F. Tuomisto, D. R. Douth, and L. J. Brillson. Self-compensation in semiconductors: The Zn vacancy in Ga-doped ZnO. *Physical Review B*, 84(11):115202, September 2011.
- [21] T. Pisarkiewicz, K. Zakrzewska, and E. Leja. Scattering of charge carriers in transparent and conducting thin oxide films with a non-parabolic conduction band. *Thin Solid Films*, 174:217–223, 1989.
- [22] T. Pisarkiewicz and A. Kolodziej. Nonparabolicity of the Conduction Band Structure in Degenerate Tin Dioxide. *Physica Status Solidi (B)*, 158:K5–K8, 1990.
- [23] N. Mott. Review Lecture: Metal-Insulator Transitions. *Proc. R. Soc. Lond. A*, 382(1782), 1982.
- [24] S. J. Pearton, D. P. Norton, K. Ip, Y. W. Heo, and T. Steiner. Recent advances in processing of ZnO. *Journal of Vacuum Science & Technology B: Microelectronics and Nanometer Structures*, 22(3):932, 2004.
- [25] C. Bundesmann, R. Schmidt-Grund, and M. Schubert. Optical Properties of ZnO and related compounds. In *Transparent Conductive Zinc Oxide*, pages 79–124. 2008.

- [26] K. Ellmer and G. Vollweiler. Electrical transport parameters of heavily-doped zinc oxide and zinc magnesium oxide single and multilayer films heteroepitaxially grown on oxide single crystals. *Thin Solid Films*, 496(1):104–111, February 2006.
- [27] K. Ellmer. Resistivity of polycrystalline zinc oxide films: current status and physical limit. *Journal of Physics D: Applied Physics*, 34:3097–3108, 2001.
- [28] K. Ellmer, A. Klein, and B. Rech. Electrical Properties. In *Transparent Conductive Zinc Oxide*, chapter 2, pages 35–78. Springer-Verlag, 2008.
- [29] K. Ellmer and R. Mientus. Carrier transport in polycrystalline transparent conductive oxides: A comparative study of zinc oxide and indium oxide. *Thin Solid Films*, 516(14):4620–4627, May 2008.
- [30] E. Conwell and V. F. Weisskopf. Theory of Impurity Scattering in Semiconductors. *Phys. Rev.*, 77:388, 1950.
- [31] H. Brooks. Theory of the Electrical Properties of Germanium and Silicon. *Adv. Electron. Electron Phys.*, 7:85, 1955.
- [32] R. B. Dingle. XCIV. Scattering of electrons and holes by charged donors and acceptors in semiconductors. *Phil. Mag.*, 46(379):831–840, 1955.
- [33] D. L. Rode. *Semicond. Semimet.* 10, 1. 1975.
- [34] D. J. Sondheimer and E. H. Howarth. The theory of electronic conduction in polar semi-conductors. *Proc. Roy. Soc. A*, 219(53), 1953.
- [35] D. C. Look and K. D. Leedy. Making highly conductive ZnO: creating donors and destroying acceptors. *Proc. of SPIE*, 8263:826302, February 2012.
- [36] J. Y. W. Seto. The electrical properties of polycrystalline silicon films. *Journal of Applied Physics*, 46(12):5247, 1975.
- [37] H. Fujiwara and M. Kondo. Effects of carrier concentration on the dielectric function of ZnO:Ga and In₂O₃:Sn studied by spectroscopic ellipsometry: Analysis of free-carrier and band-edge absorption. *Physical Review B*, 71(7):075109, February 2005.
- [38] F. Ruske, a. Pflug, V. Sittinger, B. Szyszka, D. Greiner, and B. Rech. Optical modeling of free electron behavior in highly doped ZnO films. *Thin Solid Films*, 518(4):1289–1293, December 2009.
- [39] D. C. Look, K. D. Leedy, D. H. Tomich, and B. Bayraktaroglu. Mobility analysis of highly conducting thin films: Application to ZnO. *Applied Physics Letters*, 96(6):062102, 2010.
- [40] E. Burstein. Anomalous Optical Absorption Limit in InSb. *Phys. Rev.*, 93(632):2–3, 1954.

Bibliography

- [41] T. S. Moss. *Optical Properties of Semiconductors*. Academic, New York, 1961.
- [42] B. E. Sernelius, K.-F. Berggren, Z.-C. Jin, I. Hamberg, and C. G. Granqvist. Band-gap tailoring of ZnO by means of heavy Al doping. *Physical Review B*, 37(17):244–248, 1988.
- [43] T. Minami, H. Nanto, and S. Takata. Optical properties of aluminum doped zinc oxide thin films prepared by rf magnetron sputtering.pdf. *Japanese Journal of Applied Physics*, 24(8):L605–L607, 1985.
- [44] P. Yu and M. Cardona. *Fundamentals of Semiconductors: Physics and Materials Properties*. Springer, 4th editio edition, 2010.
- [45] C. Klingshirn. Excitons, Biexcitons and Trions. In *Semiconductor Optics*, pages 249–271. 2012.
- [46] G. D. Mahan. Phonon-Broadened Optical Spectra: Urbach’s Rule. *Physical Review*, 145(2):602–608, 1966.
- [47] T. Makino, K. Tamura, C. Chia, Y. Segawa, M. Kawasaki, A. Ohtomo, and H. Koinuma. Optical properties of ZnO:Al epilayers: Observation of room-temperature many-body absorption-edge singularity. *Physical Review B*, 65(12):121201, March 2002.
- [48] A. Schleife, Cl. Rödl, F. Fuchs, K. Hannewald, and F. Bechstedt. Optical Absorption in Degenerately Doped Semiconductors: Mott Transition or Mahan Excitons? *Physical Review Letters*, 107(23):236405, November 2011.
- [49] K. Kopitzki and P. Herzog. *Einführung in die Festkörperphysik*. Vieweg+Teubner Verlag, 2007.
- [50] H. Lüth. *Surfaces and Interfaces of Solid Materials*. Springer-Verlag, Berlin etc., 3rd edition, 1995.
- [51] F. Urbach. The Long-Wavelength Edge of Photographic Sensitivity and of the Electronic Absorption of Solids. *Physical Review*, 92(5):1324–1324, 1953.
- [52] J. I. Pankove. Absorption Edge of Impure Gallium Arsenide. *Physical Review*, 140(6A), 1965.
- [53] G. D. Cody, T. Tiedje, B. Abeles, B. Brooks, and Y. Goldstein. Disorder and the Optical-Absorption Edge of Hydrogenated Amorphous Silicon. *Physical Review Letters*, 47(20):1480–1483, 1981.
- [54] S. Chichibu, T. Mizutani, T. Shioda, H. Nakanishi, T. Deguchi, T. Azuhata, T. Sota, and S. Nakamura. Urbach-Martienssen tails in a wurtzite GaN epilayer. *Applied Physics Letters*, 70(25):3440, 1997.

- [55] S. Wasim, C. Rincón, G. Marín, P. Bocaranda, E. Hernández, Ismaro Bonalde, and Ernesto Medina. Effect of structural disorder on the Urbach energy in Cu ternaries. *Physical Review B*, 64(19):195101, October 2001.
- [56] A. Iribarren, V. Sosa, and J. L. Pen. Band-tail parameter modeling in semiconductor materials. *Physical Review B*, 58(4):1907–1911, 1998.
- [57] R. C. Rai. Analysis of the Urbach tails in absorption spectra of undoped ZnO thin films. *Journal of Applied Physics*, 113(15):153508, 2013.
- [58] F. van Craeynest, W. Maenhout-Van Der Vorst, and W. Dekeyser. Interpretation of the Yellow Colour of Heat Treated ZnO Powder. *Physica Status Solidi (B)*, 8(3):841–846, 1965.
- [59] S.W. Xue, X.T. Zu, W.L. Zhou, H.X. Deng, X. Xiang, L. Zhang, and H. Deng. Effects of post-thermal annealing on the optical constants of ZnO thin film. *Journal of Alloys and Compounds*, 448(1-2):21–26, January 2008.
- [60] J. I. Pankove. *Optical Processes in Semiconductors*. Dover Books on Physics, 1975.
- [61] V. Srikant and D. R. Clarke. On the optical band gap of zinc oxide. *Journal of Applied Physics*, 83(10):5447, 1998.
- [62] Y. Cao, L. Miao, S. Tanemura, M. Tanemura, Y. Kuno, Y. Hayashi, and Y. Mori. Optical Properties of Indium-Doped ZnO Films. *Japanese Journal of Applied Physics*, 45(3A):1623–1628, March 2006.
- [63] J. Sans, J. Sánchez-Royo, A. Segura, G. Tobias, and E. Canadell. Chemical effects on the optical band-gap of heavily doped ZnO:M_{III} (M=Al,Ga,In): An investigation by means of photoelectron spectroscopy, optical measurements under pressure, and band structure calculations. *Physical Review B*, 79(19):195105, May 2009.
- [64] Corning Incorporated. Corning EAGLE XG AMLCD Glass Substrates Material Information, 2006.
- [65] K. Y. Lee, C. Becker, M. Muske, F. Ruske, S. Gall, B. Rech, M. Berginski, and J. Hüpkes. Temperature stability of ZnO:Al film properties for poly-Si thin-film devices. *Applied Physics Letters*, 91(24):241911, 2007.
- [66] F. Ruske, M. Roczen, K. Lee, M. Wimmer, S. Gall, J. Hüpkes, D. Hrunski, and B. Rech. Improved electrical transport in Al-doped zinc oxide by thermal treatment. *Journal of Applied Physics*, 107(1):013708, 2010.
- [67] J. George. *Preparation of Thin Films*. CRC Press, 1992.
- [68] M. Ohyama, H. Kozuka, and T. Yoko. Sol-Gel Preparation of Transparent and Conductive Aluminum-Doped Zinc Oxide Films with Highly Preferential Crystal Orientation. *J. Am. Ceram. Soc.*, 81(6):1622–1632, 1998.

Bibliography

- [69] M. J. Alam and D. C. Cameron. Preparation and properties of transparent conductive aluminum-doped zinc oxide thin films by sol-gel process. *Journal of Vacuum Science & Technology A: Vacuum, Surfaces, and Films*, 19(4):1642, 2001.
- [70] P. U. Nunes, E. Fortunato, and R. Martins. Influence of the post-treatment on the properties of ZnO thin films. *Thin Solid Films*, 383:277–280, 2001.
- [71] C. Lennon, R. Kodama, Y. Chang, S. Sivananthan, and M. Deshpande. Effects of annealing in N₂ on sputtered Al-doped ZnO thin films. *Journal of Vacuum Science & Technology B: Microelectronics and Nanometer Structures*, 27(3):1641, 2009.
- [72] B.-Y. Oh, M.-C. Jeong, D.-S. Kim, W. Lee, and J.-M. Myoung. Post-annealing of Al-doped ZnO films in hydrogen atmosphere. *Journal of Crystal Growth*, 281(2-4):475–480, August 2005.
- [73] X. Yu, J. Ma, F. Ji, Y. Wang, X. Zhang, and H. Ma. Influence of annealing on the properties of ZnO:Ga films prepared by radio frequency magnetron sputtering. *Thin Solid Films*, 483(1-2):296–300, July 2005.
- [74] C. Charpentier, P. Prod'homme, and P. Roca i Cabarrocas. Microstructural, optical and electrical properties of annealed ZnO:Al thin films. *Thin Solid Films*, 531:424–429, March 2013.
- [75] K.-K. Kim, H. Tampo, J.-O. Song, T.-Y. Seong, S.-J. Park, J.-M. Lee, S.-W. Kim, S. Fujita, and Shigeru Niki. Effect of Rapid Thermal Annealing on Al Doped n -ZnO Films Grown by RF-Magnetron Sputtering. *Japanese Journal of Applied Physics*, 44(7A):4776–4779, July 2005.
- [76] S. Takata, T. Minami, and H. Nanto. The stability of aluminum-doped ZnO transparent electrodes fabricated by sputtering. *Thin Solid Films*, 135:183–187, 1986.
- [77] J.H. Noh, H. S. Jung, J.-K. Lee, J. Y. Kim, C. M. Cho, J. An, and K.S. Hong. Reversible change in electrical and optical properties in epitaxially grown Al-doped ZnO thin films. *Journal of Applied Physics*, 104(7):073706, 2008.
- [78] M. Wimmer. *Thermische Nachbehandlung von aluminiumdotiertem Zinkoxid und die Silizium/Zinkoxid-Grenzfläche*. PhD thesis, 2011.
- [79] M. Wimmer, F. Ruske, S. Scherf, and B. Rech. Improving the electrical and optical properties of DC-sputtered ZnO:Al by thermal post deposition treatments. *Thin Solid Films*, 520(12):4203–4207, April 2012.
- [80] F. M. Smits. Measurement of sheet resistivities with four-point probe. *The Bell System Technical Journal*, 37:711–718, 1958.
- [81] L. J. van der Pauw. A method of measuring specific resistivity and Hall effect of discs of arbitrary shape. *Philips Research Reports*, 13(1):1–9, 1958.

- [82] W. H. Weber and R. Merlin. *Raman Scattering in Materials Science*. 2000.
- [83] A. Patanè and N. Balkan. *Semiconductor Reseach*. Springer, 2012.
- [84] E. Le Ru and P. Etchegoin. Raman spectroscopy and related optical techniques. In *Principles of Surface-Enhanced Raman Spectroscopy: and related plasmonic effects*, chapter 2, pages 29–119. Elsevier, 2008.
- [85] L. Spieß, G. Teichert, R. Schwarzer, H. Behnken, and C. Genzel. *Moderne Röntgenbeugung*. Vieweg+Teubner, 2009.
- [86] M. Birkholz. Line Profile Analysis. In *Thin Film Analysis by X-Ray Scattering*. Wiley-VCH Verlag GmbH & Co. KGaA, 2006.
- [87] P. Scherrer. Bestimmung der Größe und der inneren Struktur von Kolloidteilchen mittels Röntgenstrahlen. *Göttinger Nachrichten*, 2:98, 1918.
- [88] H.F. McMurdiea, M. C. Morris, E. H.. Evans, B. Paretzkin, W. Wong-Nga, L. Etlinger, and C. R. Hubbard. Powder Diffraction. 1(2):64–77, 1986.
- [89] M. V. Ponomarev, K. Sharma, M. a. Verheijen, M. C. M. van de Sanden, and M. Creatore. Improved conductivity of aluminum-doped ZnO: The effect of hydrogen diffusion from a hydrogenated amorphous silicon capping layer. *Journal of Applied Physics*, 111(6):063715, 2012.
- [90] A. Van der Drift. Evolutionary selection, a principle governing growth orientation in vapour-deposited layers. *Philips Reseach Reports*, 22(3), 1967.
- [91] K. H. Kim, K. C. Park, and D. Y. Ma. Structural, electrical and optical properties of aluminum doped zinc oxide films prepared by radio frequency magnetron sputtering. *Journal of Applied Physics*, 81(12):7764, 1997.
- [92] B. Szyszka and S. Jäger. Optical and electrical properties of doped zinc oxide films prepared by ac reactive magnetron sputtering. *Journal of Non-Crystalline Solids*, 218:74–80, 1997.
- [93] J. Hüpkes. *Untersuchung des reaktiven Sputterprozesses zur Herstellung von aluminiumdotierten Zinkoxid- Schichten für Silizium-Dünnschicht-*. PhD thesis, Rheinisch-Westfälische Technische Hochschule Aachen, 2005.
- [94] M. Berginski. *Schichten und Schichtsysteme zur Verbesserung der Lichteinkopplung in Silizium-Dünnschichtsolarzellen*. PhD thesis, Rheinisch-Westfälische Technische Hochschule Aachen, 2007.
- [95] R. Wen, L. Wang, X. Wang, G.-H. Yue, Y. Chen, and D.-L. Peng. Influence of substrate temperature on mechanical, optical and electrical properties of ZnO:Al films. *Journal of Alloys and Compounds*, 508(2):370–374, October 2010.

Bibliography

- [96] F. C. M. Van de Pol, F. R. Bööm, and T. J. A. Popma. R.F. planar magnetron sputtered ZnO films I: Structural properties. *Thin Solid Films*, 204:349–364, 1991.
- [97] D. Köhl, M. Luysberg, and M. Wuttig. Structural improvement of zinc oxide films produced by ion beam assisted reactive sputtering. *Journal of Physics D: Applied Physics*, 43(20):205301, May 2010.
- [98] H. Ibach. Thermal Expansion of Silicon and Zinc Oxide (II). *Physica Status Solidi*, 33:257–265, 1969.
- [99] F. Friedrich. *Struktur und Gitterdynamik von Gruppe-V-Elementen in ZnO*. PhD thesis, Technische Universität Berlin, 2009.
- [100] C. Bundesmann, N. Ashkenov, M. Schubert, D. Spemann, T. Butz, E. M. Kaidashev, M. Lorenz, and M. Grundmann. Raman scattering in ZnO thin films doped with Fe, Sb, Al, Ga, and Li. *Applied Physics Letters*, 83(10):1974–1976, 2003.
- [101] F. Friedrich and N. H. Nickel. Resonant Raman scattering in hydrogen and nitrogen doped ZnO. *Applied Physics Letters*, 91(11):111903–1 – 3, 2007.
- [102] F. Reuss. Optical investigations on the annealing behavior of gallium- and nitrogen-implanted ZnO. *Journal of Applied Physics*, 95(7):3385, 2004.
- [103] Z. Q. Chen, M. Maekawa, a. Kawasuso, S. Sakai, and H. Naramoto. Annealing process of ion-implantation-induced defects in ZnO: Chemical effect of the ion species. *Journal of Applied Physics*, 99(9):093507, 2006.
- [104] M. Tzolov, N. Tzenov, D. Dimova-malinovska, M. Kalitzova, and C. Pizzuto. Vibrational properties and structure of undoped and Al-doped ZnO films deposited by RF magnetron sputtering. *Thin Solid Films*, 379:28–36, 2000.
- [105] A. Kaschner, U. Haboek, Martin Strassburg, Matthias Strassburg, G. Kaczmarczyk, A. Hoffmann, C. Thomsen, A. Zeuner, H. R. Alves, D. M. Hofmann, and B. K. Meyer. Nitrogen-related local vibrational modes in ZnO:N. *Applied Physics Letters*, 80(11):1909, 2002.
- [106] F. J. Manjón, B. Marí, J. Serrano, and a. H. Romero. Silent Raman modes in zinc oxide and related nitrides. *Journal of Applied Physics*, 97(5):053516, 2005.
- [107] F. Friedrich, M. A. Gluba, and N. H. Nickel. Identification of nitrogen and zinc related vibrational modes in ZnO. *Applied Physics Letters*, 95(14):141903, 2009.
- [108] M. Gluba, N. Nickel, and N. Karpensky. Interstitial zinc clusters in zinc oxide. *Physical Review B*, 88(24):245201, December 2013.
- [109] M. Berginski, J. Hüpkes, M. Schulte, G. Schöpe, and H. Stiebig. The effect of front ZnO:Al surface texture and optical transparency on efficient light trapping in silicon thin-film solar cells. *Journal of Applied Physics*, 074903(2007), 2012.

- [110] H. Zhu, J. Hüpkes, E. Bunte, and S.M. Huang. Study of ZnO:Al films for silicon thin film solar cells. *Applied Surface Science*, 261:268–275, November 2012.
- [111] Y. Igasaki and H. Saito. Substrate temperature dependence of electrical properties of ZnO:Al epitaxial films on sapphire (1210). *Journal of Applied Physics*, 69(4):2190, 1991.
- [112] I. Hamberg, C. G. Granqvist, K. F. Berggren, B. E. Sernelius, and L. Engström. Band-gap widening in heavily Sn-doped In_2O_3 . *Physical Review B*, 30(6):3240–3249, 1984.
- [113] Z.-C. Jin, I. Hamberg, and C.G. Granqvist. Optical properties of sputter-deposited ZnO:Al thin films. *Journal of Applied Physics*, 64, 1988.
- [114] D. Mergel and Z. Qiao. Dielectric modelling of optical spectra of thin In_2O_3 :Sn films. *J. Phys. D: Appl. Phys.*, 794(35):794–801, 2002.
- [115] A. Pflug, V. Sittinger, F. Ruske, B. Szyszka, and G. Dittmar. Optical characterization of aluminum-doped zinc oxide films by advanced dispersion theories. *Thin Solid Films*, 455-456:201–206, May 2004.
- [116] S. Neubert, M. Wimmer, F. Ruske, S. Calnan, O. Gabriel, B. Stannowski, R. Schlattmann, and B. Rech. Improved conversion efficiency of a-Si:H/ $\mu\text{c-Si:H}$ thin-film solar cells by using annealed Al-doped zinc oxide as front electrode material. *Progress in Photovoltaics: Research and Applications*, 2013.
- [117] D. Dimova-Malinovska, H. Nichev, O. Angelov, V. Grigorov, and M. Kamenova. Electrical and optical properties of ZnO thin films prepared by magnetron rf sputtering - influence of Al, Er and H. *Superlattices and Microstructures*, 42(1-6):123–128, July 2007.
- [118] S. Neubert. internal communication, 2014.
- [119] M. Bär, M. Wimmer, R. G. Wilks, M. Roczen, D. Gerlach, F. Ruske, K. Lips, B. Rech, L. Weinhardt, M. Blum, S. Pookpanratana, S. Krause, Y. Zhang, C. Heske, W. Yang, and J. D. Denlinger. Impact of solid-phase crystallization of amorphous silicon on the chemical structure of the buried Si/ZnO thin film solar cell interface. *Applied Physics Letters*, 97(7):072105, 2010.
- [120] N. Y. Garces, N. C. Giles, L. E. Halliburton, G. Cantwell, D. B. Eason, D. C. Reynolds, and D. C. Look. Production of nitrogen acceptors in ZnO by thermal annealing. *Applied Physics Letters*, 80(8):1334, 2002.
- [121] T. Minami, T. Miyata, and T. Yamamoto. Stability of transparent conducting oxide films for use at high temperatures. *Journal of Vacuum Science & Technology A: Vacuum, Surfaces, and Films*, 17(4):1822, 1999.

Bibliography

- [122] H. Zhu, J. Hüpkes, E. Bunte, and S.M. Huang. Oxygen influence on sputtered high rate ZnO:Al films from dual rotatable ceramic targets. *Applied Surface Science*, 256(14):4601–4605, May 2010.
- [123] T. Tsuji and M. Hirohashi. Influence of oxygen partial pressure on transparency and conductivity of RF sputtered Al-doped ZnO thin films. *Applied Surface Science*, 157:47–51, March 2000.
- [124] D. Hwang, J. Ahn, Kw. Hui, K. Hui, and Y. Son. Effect of oxygen partial pressure contents on the properties of Al-doped ZnO thin films prepared by radio frequency sputtering. *Journal of Ceramic Processing Research*, 12(2):150–154, 2011.
- [125] R. M. Park, M. B. Troffer, C. M. Rouleau, J. M. DePuydt, and M. a. Haase. p-type ZnSe by nitrogen atom beam doping during molecular beam epitaxial growth. *Applied Physics Letters*, 57(20):2127, 1990.
- [126] P. H. Rieger. *Electron Spin Resonance: Analysis and Interpretation*. Royal Society of Chemistry, 2007.
- [127] J. L. Lyons, a. Janotti, and C. G. Van de Walle. Why nitrogen cannot lead to p-type conductivity in ZnO. *Applied Physics Letters*, 95(25):252105, 2009.
- [128] M. C. Tarun, M. Zafar Iqbal, and M. D. McCluskey. Nitrogen is a deep acceptor in ZnO. *AIP Advances*, 1(2):022105, 2011.
- [129] Hydrogen in Semiconductors,. In J. I. Pankove and N. M. Johnson, editors, *Semiconductors and Semimetals, Vol. 34*, chapter 1, pages 1–15. Academic Press, Boston, 1991.
- [130] S. Kohiki, M. Nishitani, T. Wada, and T. Hirao. Enhance conductivity of zinc oxide thin films by ion implantation of hydrogen atoms. *Applied Physics Letters*, 64(21):2876–2878, 1994.
- [131] M. L. Addonizio, A. Antonaia, G. Cantele, and C. Privato. Transport mechanisms of RF sputtered Al-doped ZnO films by H₂ process gas dilution. *Thin Solid Films*, 349:93–99, 1999.
- [132] A.Y. Polyakov, N.B. Smirnov, A.V.; Govorkov, K. Ip, M.E. Overberg, Y.W. Heo, D.P. Norton, S.J. Pearton, B. Luo, F. Ren, and J.M. Zavada. Hydrogen plasma treatment effects on electrical and optical properties of n-ZnO. *Journal of Applied Physics*, 1:400–406, 2003.
- [133] C.H. Seager and S.M. Myers. Quantative comparisons of dissolved hydrogen density and the electrical and optical properties of ZnO. *Journal of Applied Physics*, 94(5):2888–2894, 2003.
- [134] E. Mollwo. Die Wirkung von Wasserstoff auf die Leitfähigkeit und Lumineszenz von Zinkoxydkristallen. *Zeitschrift für Physik*, 138:478–488, 1954.

- [135] S. J. Baik, J. H. Jang, C. H. Lee, W. Y. Cho, and K. S. Lim. Highly textured and conductive undoped ZnO film using hydrogen post-treatment. *Appl. Phys. Lett.*, 70:3516, 1997.
- [136] A. Janotti and C. G. Van de Walle. Hydrogen multicentre bonds. *Nature materials*, 6(1):44–7, January 2007.
- [137] A. Janotti and C. G. Van de Walle. Fundamentals of zinc oxide as a semiconductor. *Reports on Progress in Physics*, 72(12):126501, December 2009.
- [138] F. Ruske, V. Sittinger, W. Werner, B. Szyszka, K. Van Osten, K. Dietrich, and R. Rix. Hydrogen Doping of ZnO:Al Films Deposited by Pulsed DC-Sputtering of Ceramic Targets. *Society of Vacuum Coaters - 48th Annual Technical Conference Proceedings*, pages 302–307, 2005.
- [139] J. N. Duenow, T. A. Gessert, D. M. Wood, A. C. Dillon, and T. J. Coutts. Effects of hydrogen ambient and film thickness on ZnO:Al properties. *Journal of Vacuum Science & Technology A: Vacuum, Surfaces, and Films*, 26(4):692, 2008.
- [140] A. Bikowski and K. Ellmer. Electrical transport in hydrogen-aluminium Co-doped ZnO and $Zn_{1-x}Mg_xO$ films: Relation to film structure and composition. *Journal of Applied Physics*, 113(5):053710, 2013.
- [141] M. D. McCluskey and S. J. Jokela. Defects in ZnO. *Journal of Applied Physics*, 071101(2009), 2012.
- [142] E. Lavrov, F. Börrnert, and J. Weber. Dominant hydrogen-oxygen complex in hydrothermally grown ZnO. *Physical Review B*, 71(3):035205, January 2005.
- [143] K. Ip, M. E. Overberg, Y. W. Heo, D. P. Norton, S. J. Pearton, C. E. Stutz, B. Luo, F. Ren, D. C. Look, and J. M. Zavada. Hydrogen incorporation and diffusivity in plasma-exposed bulk ZnO. *Applied Physics Letters*, 82(3):385, 2003.
- [144] J. Bang and K. J. Chang. Diffusion and thermal stability of hydrogen in ZnO. *Applied Physics Letters*, 92(13):132109, 2008.
- [145] M. Wimmer. *Thermische Nachbehandlung von aluminiumdotiertem Zinkoxid und die Silizium / Zinkoxid-Grenzfläche*. PhD thesis, Technischen Universität Berlin, 2011.
- [146] T. Sontheimer. *Design of electron beam evaporated Si thin films for solid phase crystallized solar cells on glass*. Phd thesis, Technische Universität Berlin, 2011.
- [147] N. Bouhssira, S. Abed, E. Tomasella, J. Cellier, a. Mosbah, M.S. Aida, and M. Jacquet. Influence of annealing temperature on the properties of ZnO thin films deposited by thermal evaporation. *Applied Surface Science*, 252(15):5594–5597, May 2006.

Bibliography

- [148] F.-J. Haug, Zs. Geller, H. Zogg, a. N. Tiwari, and C. Vignali. Influence of deposition conditions on the thermal stability of ZnO:Al films grown by rf magnetron sputtering. *Journal of Vacuum Science & Technology A: Vacuum, Surfaces, and Films*, 19(1):171, 2001.
- [149] G.J. Fang, D.J. Li, and B.-L. Yao. Effect of Vacuum Annealing on the Properties of Transparent Conductive AZO Thin Films Prepared by DC Magnetron Sputtering. *Physica Status Solidi (a)*, 193(1):139–152, September 2002.
- [150] N. R. Aghamalyan, I. A. Gambaryan, E. Kh. Goulanian, R. K. Hovsepyan, R. B. Kostanyan, S. I. Petrosyan, A. F. Zerrouk, and E. S. Vardanyan. Influence of thermal annealing on optical and electrical properties of ZnO films prepared by electron beam evaporation. *Semicond. Sci. Technol.*, 18:525–529, 2003.
- [151] Stephan Lany and Alex Zunger. Dopability, Intrinsic Conductivity, and Nonstoichiometry of Transparent Conducting Oxides. *Physical Review Letters*, 98(4):045501, January 2007.
- [152] J. Hüpkes, U. Zastrow, F. Ruske, M. Warzecha, M. Wimmer, and U. Breuer. Isotopic markers for thermal annealing and degradation studies in Zinc Oxide. *to be submitted*, 2014.
- [153] A. Zakutayev, N.H. Perry, T. O. Mason, D. S. Ginley, and S. Lany. Non-equilibrium origin of high electrical conductivity in gallium zinc oxide thin films. *Applied Physics Letters*, (103):232106, 2013.
- [154] K. Boubaker. A physical explanation to the controversial Urbach tailing universality. *The European Physical Journal Plus*, 126(1):10, January 2011.
- [155] D. Redfield. Effect of Defect Fields on the Optical Absorption Edge. *Physical Review*, 130(3):916–918, 1963.
- [156] H. Sumi and Y. Toyozawa. Urbach-Martienssen rule and exciton trapped momentarily by lattice vibrations. *Journal of the Physical Society Japan*, 31(2):343–358, 1971.
- [157] J. D. Dow and D. Redfield. Toward a Unified Theory of Urbach’s Rule and Exponential Absorption Edges. *Physical Review B*, 5(2):594–610, 1972.
- [158] B. Bosacchit and J.E. Robinson. Urbach’s rule in polar semiconductors. *Solid State Communications*, 10:797–802, 1972.
- [159] T. Skettrup. Urbach’s rule derived from thermal fluctuations in the band-gap energy. *Physical Review B*, 18(6):2622–2631, 1978.
- [160] S. John, C. Soukoulis, Mh. Cohen, and En. Economou. Theory of electron band tails and the Urbach optical-absorption edge. *Physical review letters*, 57(14):1777–1780, October 1986.

- [161] K. Noba and Y. Kayanuma. Urbach tail for ferroelectric materials with an order-disorder-type phase transition. *Physical Review B*, 60(7):4418–4421, 1999.
- [162] E. O. Kane. Band tails in semiconductors. *Solid-state Electronics*, 28(1/2):3–10, 1985.
- [163] B. I. Halperin and M. Lax. Impurity-Band Tails in the High-Density Limit. I. Minimum Counting Methods. *Physical Review*, 1532(1963):722–740, 1966.
- [164] A. Iribarren, V. Sosa, and J. L. Pen. Modeling of the disorder contribution to the band-tail parameter in semiconductor materials. *Physical Review B*, 60(7):4758–4762, 1999.
- [165] L. Samuel, Y. Brada, A. Burger, and M. Roth. Urbach rule in mixed single crystals of $\text{ZnxCd}_{1-x}\text{Se}$. *Physical Review B*, 36(2):1168–1173, 1987.
- [166] P. Van Mieghem. Theory of band tails in heavily doped semiconductors. *Reviews of Modern Physics*, 64(3):755–793, 1992.
- [167] J. I. Pankove. Absorption Edge of Impure Gallium Arsenide. *Physical Review*, 9(1955):2059–2065, 1965.
- [168] J. Singh. Fundamental optical properties of materials II. In *Optical Properties of Condensed Matter and Applications*. John Wiley & Sons, 2006.
- [169] M. Schreiber and Y. Toyozawa. Numerical Experiments on the Absorption Lineshape of the Exciton under lattice Vibrations. III. The Urbach Rule.pdf. *Journal of the Physical Society Japan*, 51(5):1544–1550, 1982.
- [170] R. J. Elliott. Intensity of optical absorption by excitons. *Physical Review*, 108(6):1384–1389, 1957.
- [171] T. Makino, Y. Segawa, S. Yoshida, A. Tsukazaki, A. Ohtomo, and M. Kawasaki. Gallium concentration dependence of room-temperature near-band-edge luminescence in n-type ZnO:Ga . *Applied Physics Letters*, 85(5):759, 2004.
- [172] T. Makino, Y. Segawa, S. Yoshida, A. Tsukazaki, A. Ohtomo, M. Kawasaki, and H. Koinuma. Free-Carrier Effects on Zero- and One-Phonon Absorption Onsets of n-Type ZnO . *Japanese Journal of Applied Physics*, 44(10):7275–7280, October 2005.
- [173] M. Buchanan, J. B. Webb, and D. F. Williams. Preparation of conducting and transparent thin films of tin-doped indium oxide by magnetron sputtering. *Applied Physics Letters*, 37(2):213, 1980.
- [174] E. Fortunato, D. Ginley, H. Hosono, and D. C. Paine. Transparent Conducting Oxides for Photovoltaics. 32(March):242–247, 2007.

Bibliography

- [175] Tadatsugu Minami. Present status of transparent conducting oxide thin-film development for Indium-Tin-Oxide (ITO) substitutes. *Thin Solid Films*, 516(17):5822–5828, July 2008.
- [176] R. Bel Hadj Tahar, T. Ban, Y. Ohya, and Y. Takahashi. Tin doped indium oxide thin films: Electrical properties. *Journal of Applied Physics*, 83(5):2631, 1998.
- [177] T. Koida, H. Fujiwara, and M. Kondo. Hydrogen-doped In₂O₃ as High-mobility Transparent Conductive Oxide. *Japanese Journal of Applied Physics*, 46(No. 28):L685–L687, July 2007.
- [178] L. Barraud, Z.C. Holman, N. Badel, P. Reiss, a. Descoedres, C. Battaglia, S. De Wolf, and C. Ballif. Hydrogen-doped indium oxide/indium tin oxide bilayers for high-efficiency silicon heterojunction solar cells. *Solar Energy Materials and Solar Cells*, 115:151–156, August 2013.
- [179] G. Köppel. *Beeinflussung der elektrischen Eigenschaften von ZnO : Al durch Variation der Depositionstemperatur und thermische Nachbehandlung*. Bachelor thesis, Technische Universität Berlin, 2011.
- [180] N. Itagaki, K. Kuwahara, K. Nakahara, D. Yamashita, G. Uchida, K.i Koga, and M. Shiratani. Highly Conducting and Very Thin ZnO:Al Films with ZnO Buffer Layer Fabricated by Solid Phase Crystallization from Amorphous Phase. *Applied Physics Express*, 4(1), 2010.
- [181] S. Neubert, S. Ring, F. Welker, S. Götzendorfer, F. Ruske, B. Stannowski, R. Schlattmann, and B. Rech. Very thin, highly conductive ZnO:Al front electrode on textured glass as substrate for thin-film silicon solar cells. *Phys. Status Solidi RRL*, 8:44–47, 2013.
- [182] A. Horn, C.-C. Kalmbach, J. G. Moreno, V. Schütz, U. Stute, and L. Overmeyer. Laser-Surface-Treatment for Photovoltaic Applications. *Physics Procedia*, 39:709–716, 2012.
- [183] E. Schumann. *Entwicklung eines Laserprozesses zur gezielten Veränderung elektrooptischer Eigenschaften von Zinkoxid*. Master thesis, RWTH Aachen, 2012.
- [184] M. F. Ogawa, Y. Natsume, T. Hirayama, and H. Sakata. Optical absorption edge of zinc oxide films by CVD. *Journal of Materials Science Letters*, 9:1354–1356, 1990.
- [185] Y. Hishikawa, N. Nakamura, S. Tsuda, S. Nakano, A. Kishi, and Y. Kuwano. Interference-free determination of the optical absorption coefficient and optical gap of amorphous silicon thin films. *Japanese Journal of Applied Physics*, 30(5):1008–1014, 1991.
- [186] D. Ritter and K. Weiser. Suppression of interference fringes in absorption measurements on thin films. *Optics Communications*, 57(5):336–338, 1986.

Acknowledgements

At this point, I would like to express my gratitude to the people who made this work possible and who supported me throughout the last three years.

At first, I thank **Prof. Dr. Bernd Rech** for giving me the opportunity to continue doing research at the *Institute for Silicon Photovoltaics* after my master's project and to write this thesis. Additionally, I would like to express my deepest gratitude to him for providing nearly stress-free working conditions during my pregnancy, especially towards the end of the writing process.

I am very grateful to **Prof. Dr. Mario Dähne** and **Prof. Dr. Matthias Wuttig** for the friendly and uncomplicated acceptance of assessment of this work.

My deepest appreciation goes to **Dr. Florian Ruske** for supervising me and whose enormous support and insight comments were invaluable during the last three years.

I would like to offer my special thanks to **Marion Krusche** who has the admirable ability to master the sometimes overwhelming bureaucratic jungle and to solve every issue within the shortest possible time.

I have greatly benefited from the support and huge knowledge concerning everything related to vacuum technology and thin film deposition of **Martin Reiche**. Thank you very much for your patience and advice.

I am particularly grateful for the excellent work of our student assistant **Martina Trahms**, whose support by providing characterisation measurements especially during the final stage of this dissertation was invaluable.

Generally, I would like to thank all people who have been or are still working at the *Competence Centre Thin-Film- and Nanotechnology for Photovoltaics Berlin* (PVcomB), where I spent more than two third of my time and where most of my laboratory work took place. The working atmosphere could not have been better and I will miss the countless cakes in the kitchen a lot.

Especially, I thank **Karolina Mack** for support with the analytic tools at the PVcomB and crafting gloves-animals with me in times of ill mood.

Furthermore, I have greatly benefited from discussions with **Sebastian Neubert**. For his valuable advice and helpful comments I am particularly grateful.

A special thanks also go to **Dr. Marc Gluba** for support with the Raman setup and useful insights into Raman spectroscopy.

I would like to thank **Carola Klimm** for providing SEM and EDX measurements.

The project partners in LIST I thank for the good cooperation, the project meetings and great discussions.

I thank my friends **Corinna Grosse, Roman Bansen, Jan Schmidtbauer, Yuan Zhang** and **Fuxian Wang** for being the best company during lunch breaks and for our memorable conversations about everything under the sun and beyond.

I am indebted to **Robert Braun** for spending hours of his time with proof-reading this thesis.

My deepest appreciation and in words barely expressible gratitude goes to my parents, my grandparents, brothers and especially to Peter for their neverending love and support and for their encouragement throughout this entire journey.

Finally, I thank my (yet unborn) child, even if he has to wait a couple of years to be able to read it. Although distracting my focus quite often, I would have struggled to find the inspiration and motivation needed to complete this dissertation without him.